DELAMINATION GROWTH

IN COMPOSITE MATERIALS

John W. Gillespie, Jr.
Leif A. Carlsson
R. Byron Pipes
Robert Rothschilds
Bruce Trethewey
and
Anthony Smiley

CENTER FOR COMPOSITE MATERIALS
College of Engineering
University of Delaware
Newark, Delaware 19716

NASA Grant Number NAG-1-475
Program Monitor: John D. Whitcomb

ABSTRACT

In this report research related to growth of an imbedded through-width delamination (ITWD) in a compression loaded composite structural element is presented. In the experimental part of the study, composites with widely different interlaminar fracture resistance were examined, viz., graphite/epoxy (CYCOM 982) and graphite/PEEK (APC-2).

The initial part of the program consisted of characterizing the material in tension, compression and shear mainly to obtain consistent material properties for analysis, but also as a check of the processing method developed for the thermoplastic APC-2 material.

The characterization of the delamination growth in the ITWD specimen, which for the unidirectional case is essentially a mixed Mode I and II geometry, requires verified mixed-mode growth criteria for the two materials involved. For this purpose the main emphasis during this part of the investigation has been on Mode I and II fracture specimens, namely the Double Cantilever Beam (DCB) and End Notched Flexure (ENF) specimens. Data reduction schemes and sizing to achieve crack growth in the linear elastic regime are discussed. Moreover, beam theory expressions for the ENF specimen including the influence of interlaminar shear deformation for the compliance, C, and strain energy release rate, G_{II} has been derived. The results indicate that for certain combinations of material properties and geometry interlaminar shear may indeed need

to be accounted for in the data reduction scheme. Furthermore, the influence of friction between the crack surfaces was addressed by beam theory where the decrease in strain energy release rate due to friction was quantified by a non-dimensional strain energy release rate parameter. This parameter provides means to minimize the influence of friction by suitable specimen design. Results for commonly used ENF geometries indicate that neglecting friction, results in an overestimate of the strain energy release rate of only 2 to 4 percent for the friction coefficients investigated.

Finite element (FE) analysis was performed to investigate whether the ENF geometry is a pure Mode II test and to assess the accuracy of the beam theory expressions for C and G_{II}. The contact problem was investigated by introducing nonlinear truss elements along the crack interface. Frictional effects were also evaluated. G_I and G_{II} were numerically determined using the virtual closure technique which enables mode separation. G_I was found to be identically zero. The compliance method for calculating the total strain energy release rate was also utilized and gave identical results with the crack closure approach. Consequently, both numerical techniques allow G_{II} to be evaluated straightforwardly. Comparison with beam theory expressions including interlaminar shear revealed that although good agreement in global compliance was obtained, beam theory expressions for G_{II} may be conservative by 20 to 40 percent for a typical unidirectional graphite fiber

composite and test specimen geometry.

A parametric study based upon the finite element analysis of the frictionless contact problem is presented. The influence of delamination length and depth, span, laminate thickness and material properties on G_{II} are presented and correlated with beam theory results. In an attempt to generalize finite element results, non-dimensional quantities for compliance and G_{II} are identified from the parametric study to accommodate sligth variations in geometry or material properties that will inevitably arise in an experimental program to characterize G_{IIC}. Based upon these results a more accurate data reduction scheme is proposed.

The numerical results on friction effects bear out that analytical beam theory provides a conservative upper bound on the decrease in G_{II} due to friction. Thus, for reasonable coefficients of friction, frictional effects are negligible for commonly used ENF geometries.

In Chapter 4, interlaminar fracture test results are presented. Important experimental parameters are isolated, such as precracking techniques, rate effects and nonlinear load-deflection response. It is found that subcritical crack growth and inelastic material behavior, responsible for the observed nonlinearities, are highly rate dependent phenomena with high rates generally leading to linear elastic type of behavior. Moreover, unstable crack growth in APC-2 during Mode I loading was found to be highly rate

dependent. At all rates, except at the lowest rates, stick-slip behavior or unstable crack growth was observed in DCB testing of APC-2. Finally, preliminary ITWD test results on 64 ply unidirectional laminates are presented.

Table of Contents

Appendices

1. INTRODUCTION

Delaminations represent a common and characteristic flaw in composite laminates that may be introduced during processing or subsequent service conditions. The local instability of composite laminates in the vicinity of interlaminar defects and the potential for delamination initiation and growth may induce significant strength reductions under compressive loadings [1-8]. Therefore, a fundamental understanding of the mechanisms governing delamination initiation and growth is required to develop appropriate failure criteria to assess defect criticality. In composite structures, impact damage may result in multiple delaminations of various planforms interacting with intraply cracks. Analysis of delamination growth including the interaction of the various flaws would be complex and require a three dimensional stress analysis. Consequently, most studies to date have considered delamination growth of imbedded defects in simple configurations. Perhaps the simplest geometry is the imbedded through-width delamination imbedded in a laminate subjected to compressive loads, see Fig. 1. Delamination growth models for this geometry based upon fracture mechanics have been reported by a host of researchers [1,4,5,9-12]. Strain energy release rate formulations have been based upon both analytic formulations [1,4,5,10] and finite element analysis [9,11,12]. The Mode I component of the strain energy release rate, G_I, for a compressively loaded laminate with an ITWD monotonically increases, attains a global maximum and diminishes to zero with increasing load [1,9,13]. The Mode II component

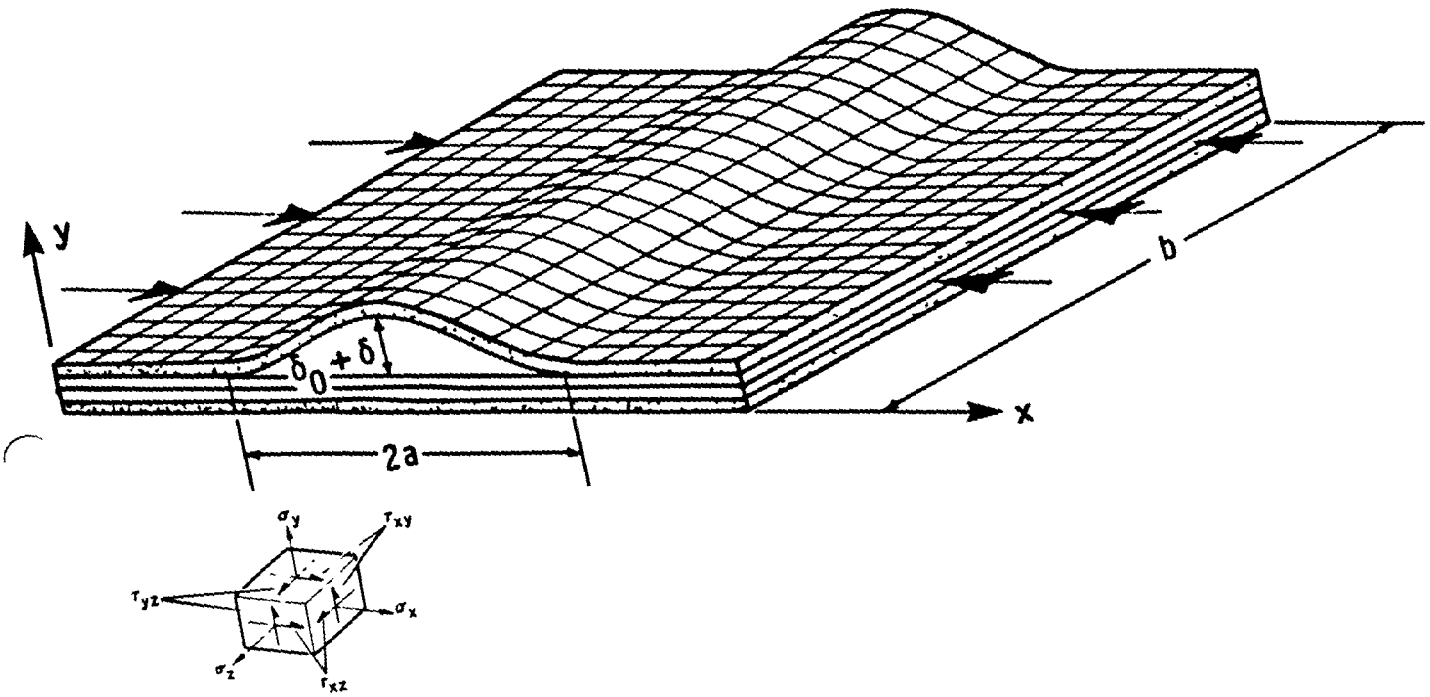

Fig. 1 Local Buckling of ITWD in a compressively loaded laminate [9].

(G_{II}), however, is a monotonically increasing function of the applied compressive load. This phenomenon is attributed to geometric non-linearity and the reduction in axial stiffness exhibited by the buckled sublaminate in particular.

Trends based upon existing models and fracture criteria, however, appear contradictory and are in all probability only applicable for specific combinations of material systems and delamination geometries. Whitcomb [13] clearly highlights the need for an experimentally verified mixed-mode failure criteria by presenting, in Fig. 2, large differences in predicted loads for the onset of delamination growth for a variety of typical growth criteria employed in the analysis of ITWD specimens. In general terms, short deeply imbedded delaminations or delaminations in materials exhibiting low Mode I fracture toughness should be predicted accurately by $G_I = G_{IC}$. For this combination of ITWD geometry and G_{IC}, the Mode II component G_{II} is negligible and all three failure criteria converge for short delaminations, see Fig. 2. Conversely, long near surface delaminations or materials exhibiting large G_{IC} values exhibit reduced axial stiffness resulting in a dominately Mode II state of deformation since G_I tends to zero. Consequently for this bound on ITWD geometry, the appropriate failure criteria would be $G_{II} = G_{IIC}$. In this regime, only the mixed-mode failure criterion attempts to include the dominate Mode II contribution. Therefore, the critical loads for delamination onset diverge significantly as shown in Fig. 2 for the three failure criteria considered. For intermediate combinations of ITWD geometries and

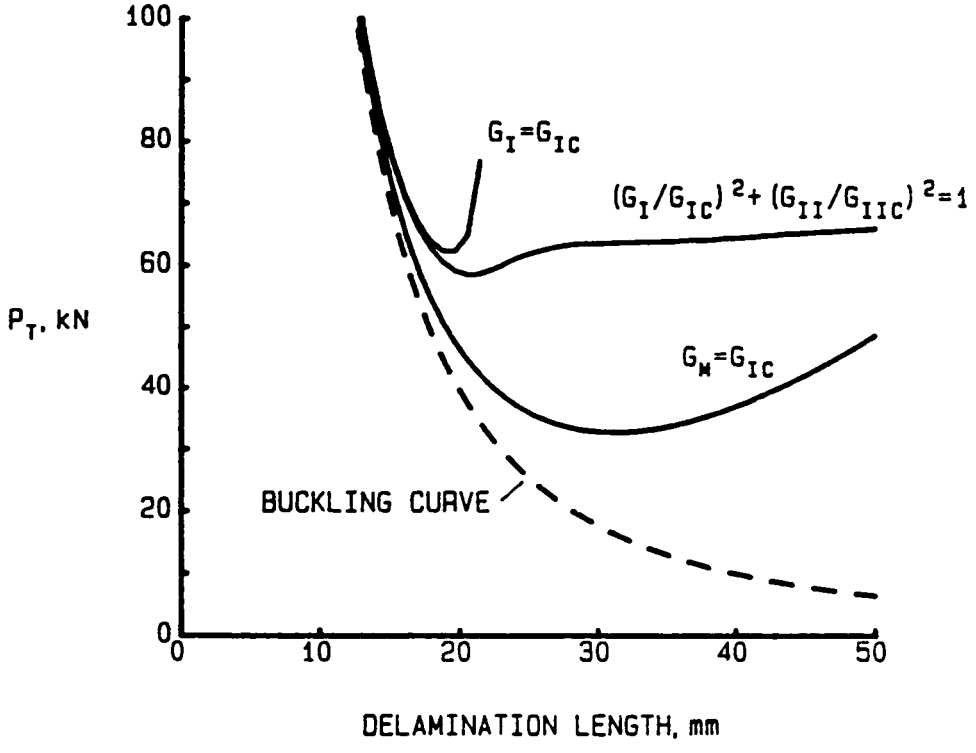

Fig. 2 Critical load for delamination growth using three growth criteria [13].

fracture toughnesses falling within the two limiting bounds mentioned above, the Mode I and Mode II components of strain energy release rate may be equally important for predicting delamination growth. In this situation, only an appropriate mixed-mode failure criterion will incorporate the actual mechanisms of delamination growth and include both bounds discussed above.

In the present study, a comprehensive investigation of instability related delamination growth is underway through the following research objectives:

- Experimental investigation of instability-related delamination growth for two graphite fiber composites exhibiting significantly different fracture toughnesses. Various delamination lengths and depths are considered to provide a wide range of mixed-mode response.
- Correlate experimental data (pre and postbuckling strains and deformations) with analytic and geometrically non-linear finite element results.
- Establish a mixed-mode interlaminar fracture criteria by direct correlation with experimental data for the onset of delamination growth in the ITWD test specimen.

The validity of any mixed-mode failure criterion, however, is strongly dependent upon the accuracy of independent critical strain energy release rate measurements. Fracture tests employed in the present study consist of the Double Cantilever Beam (DCB), Cracked Lap Shear (CLS) and the relatively new End Notched

Flexural (ENF) test specimens. The DCB specimen is a viable pure Mode I test for measuring G_{IC}. Stable crack growth is achievable enabling the compliance method to be employed in the straightforward data reduction scheme summarized in Appendix 1. The CLS fracture specimen is a mixed-mode test as quantified by finite element analysis in conjunction with crack closure techniques [14,15]. The approach employed in a previous study [15] to estimate G_{IIC} for a material system of interest is possible only by assuming a mixed-mode failure criterion. G_{IIC} is then back calculated employing finite element results for mode separation. Obviously, this is not the ideal procedure for deriving an appropriate mixed mode failure criterion. The CLS fracture specimen, however, provides stable crack growth resulting in the straightforward data reduction scheme for reliable measurement of the total critical strain energy release rate, G_C. Consequently, the CLS specimen, in addition to the ITWD specimen, is included in the present study to assess the validity of various failure criteria based upon independent measurements of G_{IC} and G_{IIC}.

Recently, Russell and Street [16], introduced the End Notched Flexural fracture specimen as a viable pure Mode II test. The test specimen is essentially a three point flexure specimen with an ITWD placed at the laminate mid-surface where interlaminar shear stresses are greatest. The delamination is also placed at one end to accommodate the sliding deformation resulting from the bending of the delaminated region. The analysis of the ENF fracture specimen reported to date has been

limited to simple isotropic beam theory for deriving expressions for compliance and strain energy release rate. Since an independent measurement of G_{IIC} is required to evaluate mixed mode failure criteria for the ITWD specimen, additional analysis of the ENF fracture specimen has been performed. In Chapter 3, a more accurate beam theory formulation including interlaminar shear deformation is summarized. In addition, a closed form expression for G_{II} to quantify frictional effects opposing sliding deformation along the crack interface is derived. A non-dimensional parameter relating geometry and the coefficient of sliding friction to the reduction in strain energy release rate is identified which enables frictional effects to be minimized through the judicious choice of test specimen geometry.

Furthermore, linear elastic two-dimensional finite element analysis of the ENF test specimen is performed to assess the accuracy of beam theory expressions for G_{II}. The contact problem is included in the finite element model and frictional effects are evaluated. Strain energy release rates are evaluated numerically using the virtual crack closure technique which enables mode separation. G_I is found to be identically zero. The compliance method for calculating the total strain energy release rate is also utilized and yields identical results with the crack closure approach. Consequently, both numerical techniques allow G_{II} to be evaluated straightforwardly. The ENF fracture specimen is thus shown to be a pure Mode II test within the constraints of small deflection theory. Finite element results show that data reduction schemes based upon linear beam

theory underestimate G_{II} significantly for typical unidirectional graphite fiber composite test specimen geometries. Consequently, data reduction for the ENF fracture specimen will be based on a combination of finite element and beam theory results.

2. EXPERIMENTAL

An outline of the experimental program is presented in Table 1. The program includes processing of thermoset composites [Graphite/Epoxy (CYCOM 982)] and thermoplastic composites [Graphite/PEEK (APC-2)] in order to obtain unidirectional laminates. The basic materials characterization aims to provide the lamina elastic and failure properties and the fracture characterization will determine the interlaminar fracture toughness under pure Mode I or Mode II loading and under mixed-mode loading. Through-width delamination testing will be performed in order to investigate the applicability of the interlaminar fracture data for the instability related delamination growth observed for this specimen.

2.1 Materials Processing

The thermoset material, Graphite/CYCOM 982, was processed in an autoclave according to the prepreg manufacturer's recommended cure cycle. The processing of the thermoplastic material, Graphite/PEEK (APC-2) required the development of new processing techniques due to the high temperatures and pressures needed for this material. In Figs. 3, 4 and 5, details for the compression molding of APC-2 panels at the Center for Composite Materials are summarized. The processing closely follows ICI recommended procedures except that a single press is employed for both the heating and cooling phases shown in Fig. 4. Post consolidation cooling should be rapid and ICI achieves acceptable cooling rates by transferring the APC-2 panels to a second cool press at about 190°C. The Wabash Press employed in the current processing cools

Table 1 Outline of the Experimental Program

- Materials: Graphite/PEEK: APC-2
  Graphite/Epoxy: CYCOM 982
  Unidirectional lay-ups
- Basic Materials Characterization
  Tension, Compression, Flexure, Thermal
- Delamination Fracture Characterization
  DCB - Mode I
  ENF - Mode II
  CLS - Mode I & II (Mixed Mode)
- Through-Width Delamination Testing
  Shadow Moire
  Dial Gages
  Strain Gages

APC 2 PROCESSING

Wabash Press
Max. Temp. = 427°C (800°F)
Max. Load = 150 ton
Cooling: Air/Water

APC 2 Panel: L x W x t
L = 30.5 cm (12 in.)
W = 20.3 cm (8 in.)
t = laminate thickness

Glazing Plate (Stainless)
t_1 = 4.8 mm (0 1875 in.)

Aluminum Foil
(Release Agent Required)
t_2 = 0.1mm (0.004 in.)

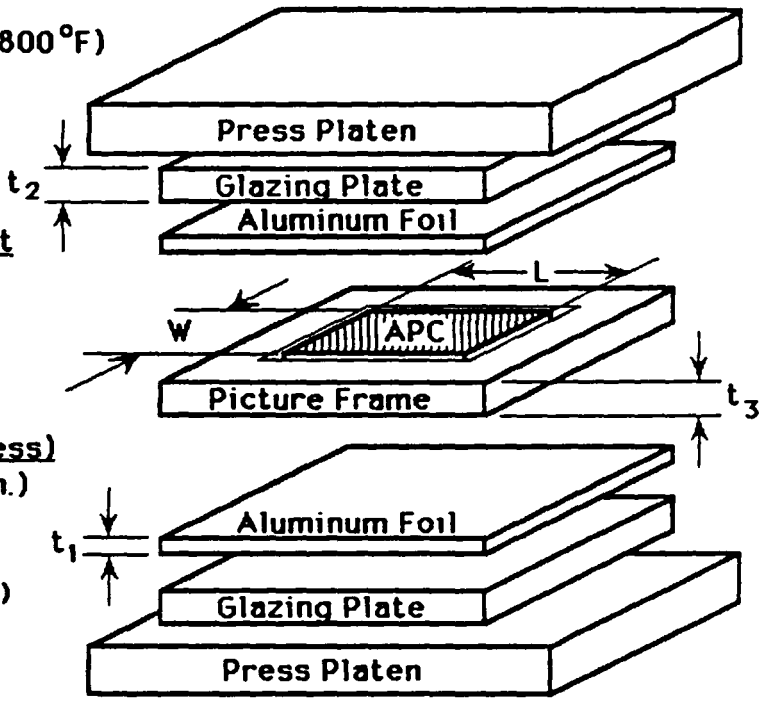

Picture Frame
0.0254 mm (0 10 in) $\leq t - t_3 \leq$ 0.38 mm (0.015 in.)

Fig. 3 APC-2 Picture Frame Molding

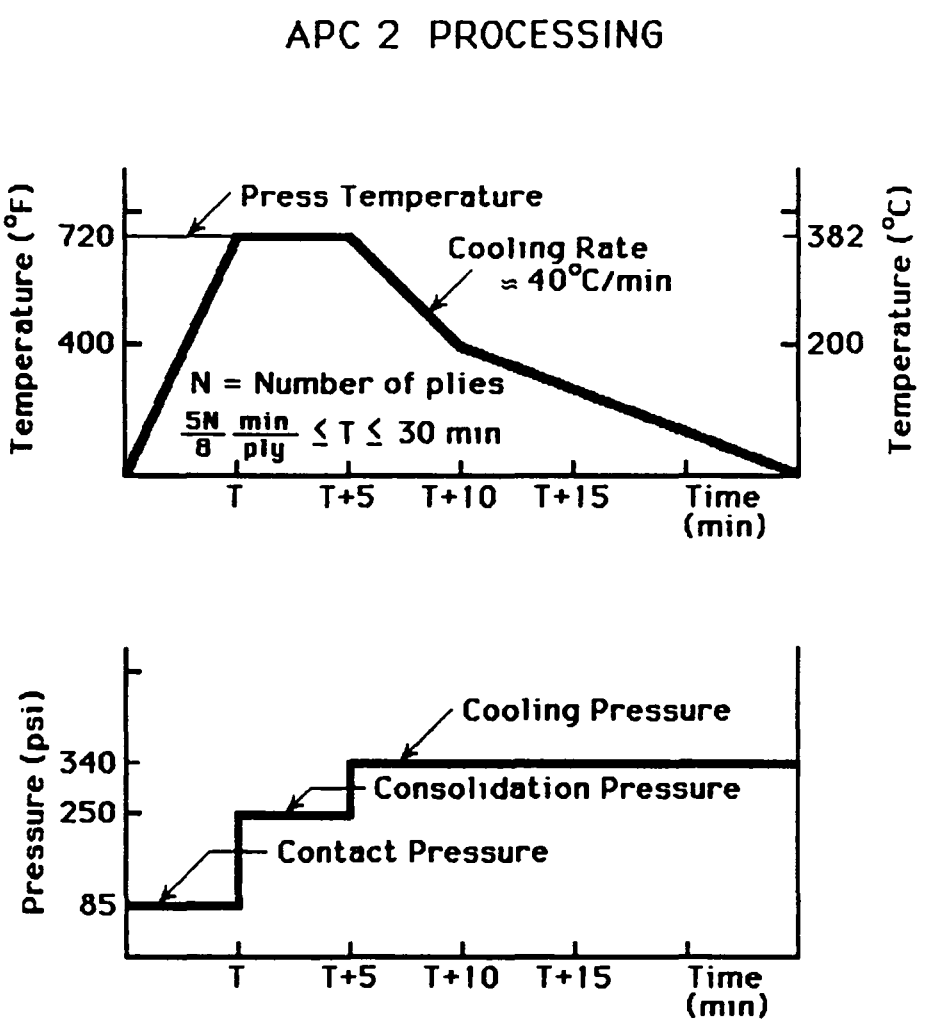

Fig. 4 APC-2 Heating/Cooling Cycle

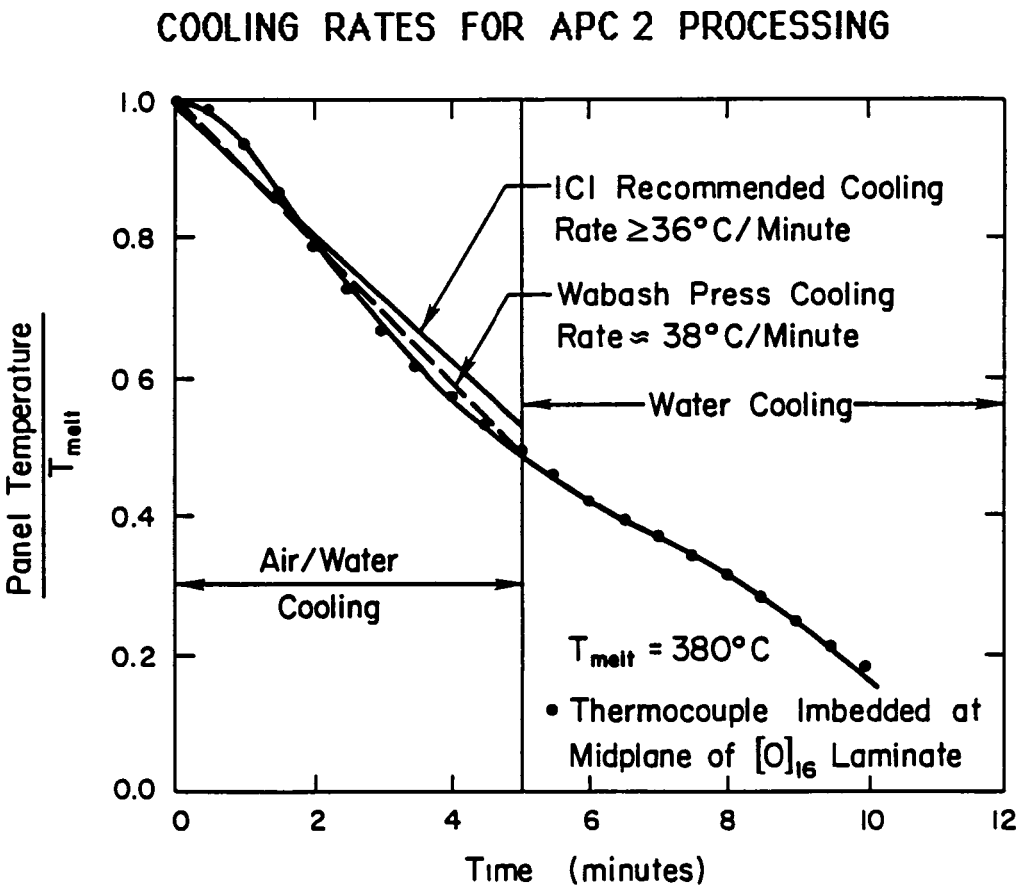

Fig. 5 Experimental Cooling Rates for APC-2 $[0]_{16}$ Panels

the press platens with an air/water mixture which provides an adequate cooling rate of approximately 40°C/min over the critical temperature range of 380°C to 200°C, see Fig. 5.

2.2 Basic Materials Characterization

The test matrix for the basic materials characterization is summarized in Table 2. Experimental results based upon five replicates/test are presented in Tables 3, 4 and 5 for APC-2 and CYCOM 982. Stress-strain curves are given in Appendix 6. In Tables 3-5, material properties taken from the ICI Provisional Data Sheet (APC PD2) are also included for direct comparison with results that correspond to the process conditions mentioned above. In all cases, excellent agreement is obtained and confidence is generated in the processing condition employed in the present study.

2.3 Determination of Interlaminar Fracture Toughness

Fracture characterization for the two graphite fiber composite materials will consist of the Double Cantilever Beam (DCB) [4,14] and the End Notched Flexure (ENF) [16] specimens for measuring G_{Ic} and G_{IIc} respectively. The Cracked Lap Shear (CLS) specimen will also be included to investigate mixed-mode fracture. The data reduction procedures are based on compliance measurements and are presented in Appendix 1. As shown schematically in Fig. 6, the compliance measurements will be made directly with an LVDT to minimize the potential source of error induced by machine and load cell compliance.

Table 2 Basic Materials Characterization

Loading	Lay-ups	Dimensions	Gages	No. of Replicas	Obtain
Tension	$[0]_8$	12.7 x 229 mm	1 Axial-Transv.	5	E_1, ν_{12}, X_1^T, $\varepsilon_1^{T,ult}$
	$[90]_{16}$	25.4 x 229 mm	"	5	E_2, ν_{21}, X_2^T, $\varepsilon_2^{T,ult}$
	$[\pm 45]_{2S}$	25.4 x 229 mm	"	5	G_{12}, S_6, γ_{12}^{ult}
Compr.	$[0]_{16}$	6.4 x 127 mm	2 Axial-Transv.	5	E_1^C, X_1^C, $\varepsilon_1^{C,ult}$
	$[90]_{40}$	12.7 x 127 mm	"	5	E_1^C, X_1^C, $\varepsilon_2^{C,ult}$
Flex.	$[0]_{16}$	6.4 x 102 mm	2 Axial (Top/bottom)	5	E_1^f, X_1^f
Thermal	$[0]_8$	50.8 x 50.8 mm	Axial-Transv.	2	α_1, α_2 (CTE)

Table 3 Tensile and Shear Test Results

Property	Units	APC-2	APC-2/ICI[2]	Graphite/CYCOM 982
E_1	GPa (Msi)	129.0 (18.7±1.0)	134.0 (19.4)	136.0 (19.7±0.1)
E_2	GPa (Msi)	9.4 (1.37±0.02)	8.9 (1.29)	10.0 (1.53±0.1)
ν_{12}		0.310±0.020	----	0.300±0.020
ν_{21}		0.023±0.003	----	0.023±0.003
G_{12}	GPa (Msi)	4.5 (0.65±0.02)	5.1 (0.74)	4.7 (0.68±0.002)
X_1^T	MPa (Ksi)	2140 (310±8)	2130 (309)	2170 (315±6)
X_2^T	MPa (Ksi)	76 (11±1)	80 (11.6)	47 (6.8±0.6)
S_6	MPa	141 (21±1)[3]	150 (22)	78 (11.3±0.2)
$\varepsilon_1^{T,ult}$	%	1.60±0.04	1.45	1.60±0.10
$\varepsilon_2^{T,ult}$	%	0.94±0.05	1.00	0.45±0.04

1 Five Replicates

2 Provisional Data Sheet APC PD2

3 $[\pm 45]_{2S}$ Laminate Strength

Table 4 Compressive Test Results

Property	Units	APC-2	APC-2/ICI	Graphite/CYCOM 982
E_1	GPa (Msi)	117 (17.0±1.0)	--	131 (19.0±1.0)
E_2	GPa (Msi)	9.2 (1.33±0.05)	--	9.3 (1.35±0.07)
X_1^c	MPa (Ksi)	1254 (182±5)	1100 (160)	1295 (188±5)
X_2^c	MPa (Ksi)	214 (31±1)	--	193 (28±1)
$\varepsilon_1^{c,ult}$	%	1.1±0.1	--	1.0±0.1
$\varepsilon_2^{c,ult}$	%	2.3±0.1	--	2.7±0.1

1 Five Replicates

2 Provisional Data Sheet APC PD2

Table 5 Fiber Volume Fraction, Coefficient of Thermal Expansion and Flexure Test Results

Property	Units	APC-2	APC-2/ICI[2]	Graphite/CYCOM 982
V_f	--	0.62	0.62	0.67
α_1	$\mu\varepsilon/^oC$ ($\mu\varepsilon/^oF$)	3.4 (1.9)	--	--
α_2	$\mu\varepsilon/^oC$ ($\mu\varepsilon/^oF$)	34.1 (18.9)	--	--
E_1^f	GPa (Msi)	115.1 (16.7±0.5)	--	126 (18.3±0.7)
X_1^f	MPa (Ksi)	1632 (237±6)	--	1729 (251±8)
$\varepsilon_1^{f,ult}$	%	1.4±0.1	--	1.3±0.1

1 Five Replicates

2 Provisional Data Sheet APC PD2

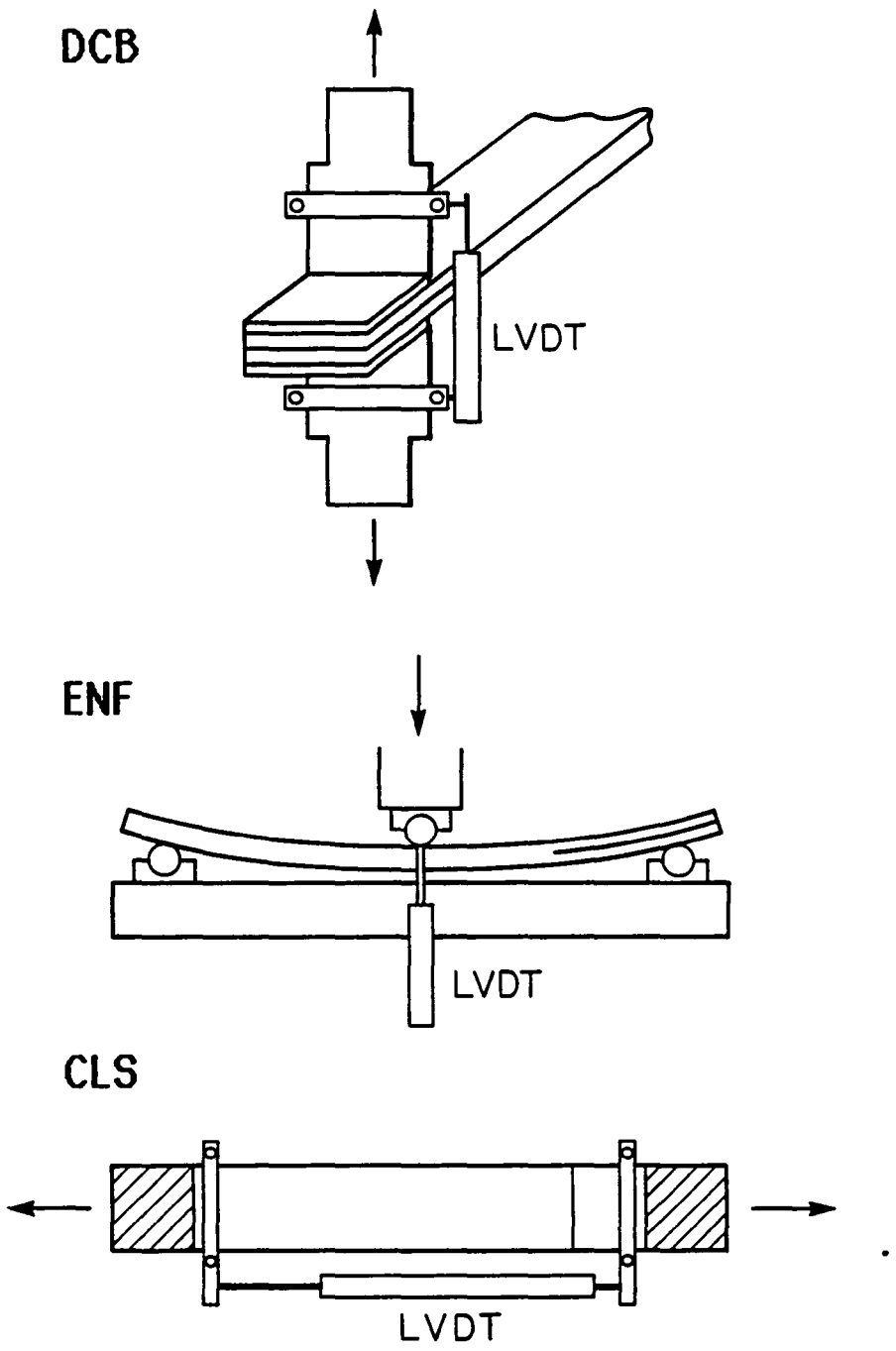

Fig. 6 Interlaminar Fracture Tests.

Unstable crack growth is a common occurrence in ENF fracture testing [15, 16]. Consequently, the data reduction scheme based upon measuring dC/da experimentally cannot be utilized and approximate beam theory expressions or a finite element based crack closure calculation has to be used. The stability analysis of crack growth for the ENF specimen presented in Appendix 2, however, indicates that stable crack growth may be attainable under fixed displacement conditions for $a/L \simeq 0.7$ where a is the crack length and L is the half span. This will be investigated experimentally in the present project. Interestingly, most results in the literature [15, 17] have been for $a/L \approx 0.5$ and unstable crack growth has been reported.

It is anticipated that the APC-2 thermoplastic will exhibit an order of magnitude greater fracture toughness than the typical graphite thermosets [18]. Consequently, design and sizing of the various fracture tests to avoid tensile or flexure failures and to guarantee crack growth is an important consideration in the present study. In Table 6, the design considerations for sizing the DCB, ENF and CLS specimens are summarized. Details are presented in Appendix 3.

In Fig. 7, the number of plies required to keep the DCB specimen in the linear regime is presented as a function of G_{IC}. Results indicate that the standard 24 ply unidirectional laminate should be thick enough to avoid large deflection response even for the APC-2 material. However, processing constraints require 26 ply APC-2 specimens.

Table 6 Design considerations for Sizing the Fracture Specimens

Specimen	Constraints
DCB	Maintain linear behavior
ENF	Avoid flexural failure, maintain linear behavior
CLS	Avoid strap tensile failure

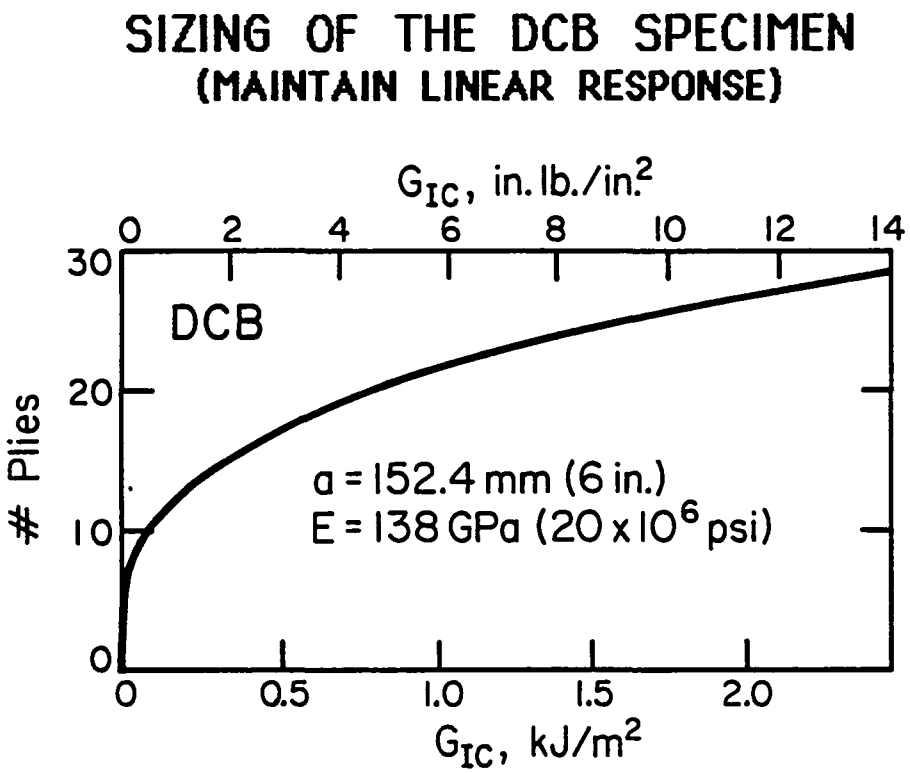

Fig. 7 Sizing the DCB Specimen to maintain linear behavior

In Fig. 8, the number of plies for the CLS specimen required to avoid tensile strap failure is presented. A six ply laminate will be employed for both materials. In Fig. 9, the number of plies for the ENF specimen required to maintain linear response and to avoid flexural failure is presented as a function of G_{IIc}. In the range of G_{IIc} values expected for the CYCOM 982 thermoset material ($2kJ/m^2$), the small deflection behavior dictates the number of plies required for the ENF specimen. In the present study, twenty-four plies will be employed for the thermoset material which is consistent with the geometry used for data published earlier [16,17]. APC-2, on the other hand, may have high G_{IIc} values and flexural failure may occur prior to crack propagation. Consequently, ENF specimens fabricated from APC-2 will be 40 plies as well as the standard 26 ply laminate. A summary of the fracture test based upon the above considerations is presented in Table 7.

2.4 Imbedded Through-Wdith Delamination Specimen Testing

The experimental evaluation of delamination growth for the ITWD specimen will initially be limited to imbedded single delaminations and unidirectional lay-ups. Unidirectional laminates are chosen so that direct correlation can be established with the unidirectional DCB, ENF and CLS test results. Also, the Mode III component of the strain energy release rate will be absent when the implanted defect is located between the plies in a unidirectional laminate. This results in considerable simplication of the problem. Strain gages mounted at the center of the surface of the delamination are being used to monitor the onset of buckling and to allow for comparison

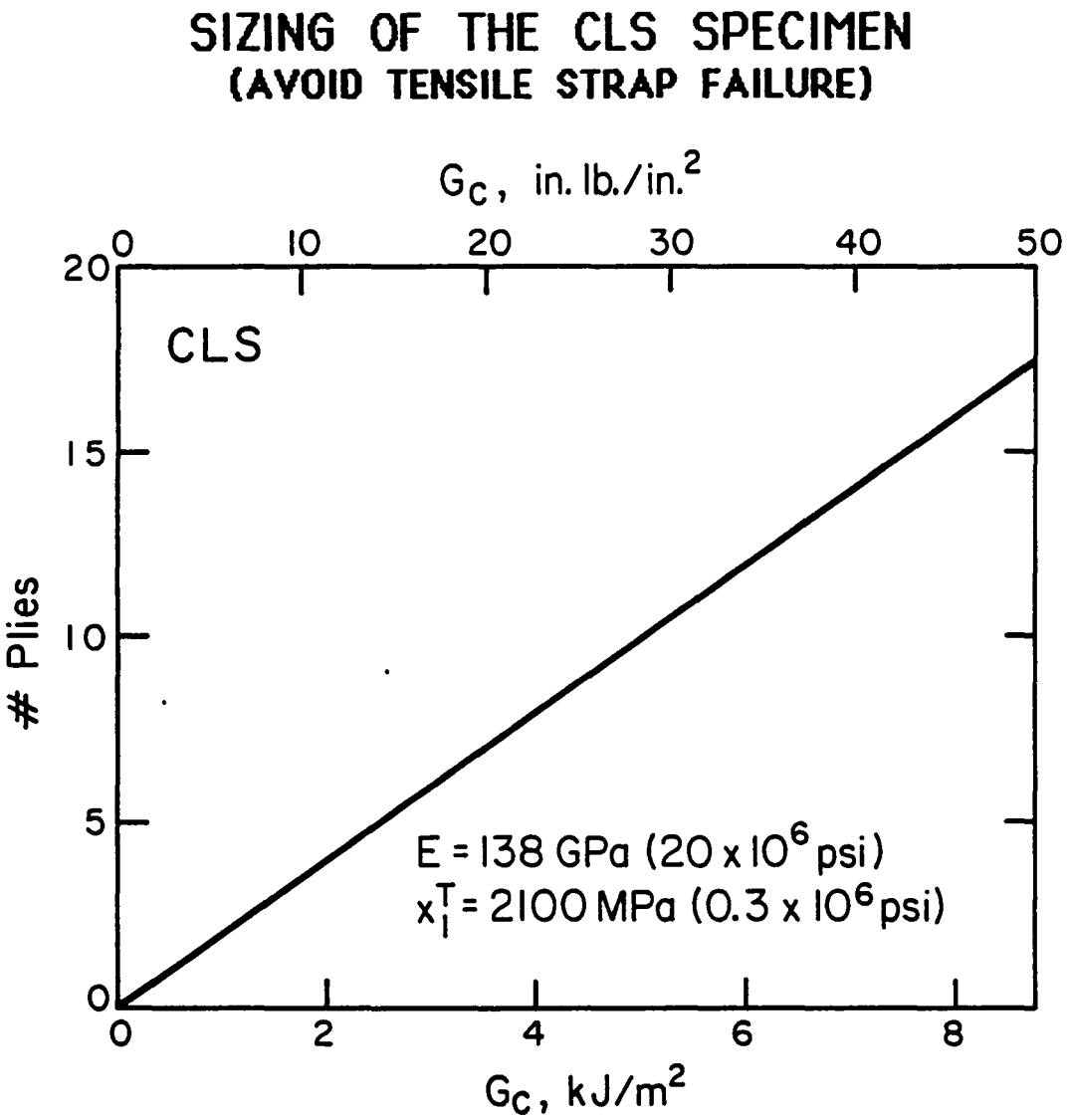

Fig. 8 Sizing the CLS Specimen to avoid strap failure

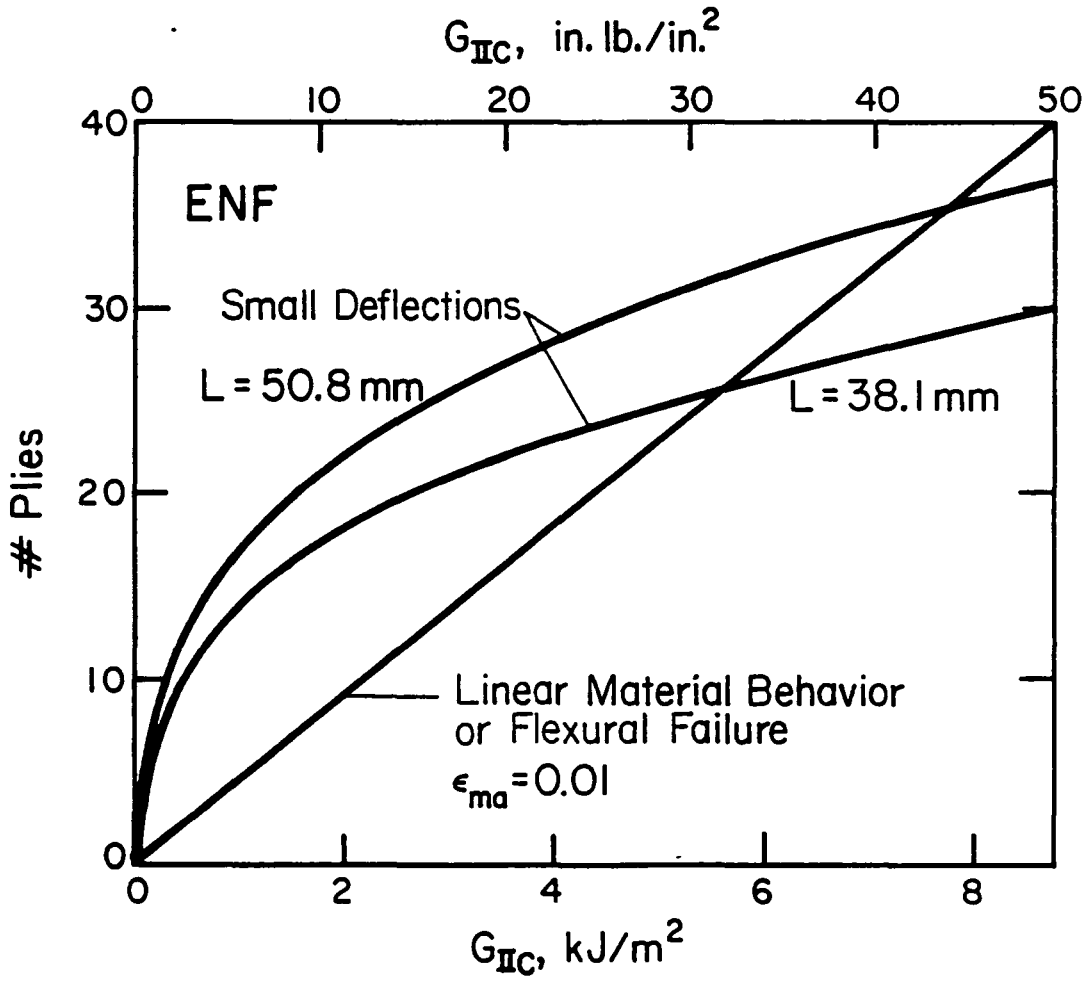

Fig. 9 Sizing the ENF Specimen to maintain linear elastic response E_1 = 138 GPa, a/L = 0.5 and y_a^1 = 0.2

Table 7 Details of Interlaminar Fracture Testing

Specimen	APC-2	CYCOM 982	Dimensions	Compliance Determination	Data Reduction	Obtain
DCB	$[0]_{26}$	$[0]_{24}$	25.4 x 254 mm	crosshead movement	Compliance and Area Methods	G_{Ic}
ENF	$[0]_{26}$,$[0]_{40}$	$[0]_{24}$	25.4 x 279 mm	LVDT,crosshead	FE/Beam Theory	G_{IIc}
CLS	$[0]_{6}$	$[0]_{6}$	25.4 x 254 mm	LVDT,crosshead	Compliance	$G_{I,IIc}$

* All specimens have a 25.4 mm long starter crack consisting of a 0.025 mm thick Kepton film.

betweeen analysis and experiment. Dial gages are used to detect the magnitude of the out-of-plane displacements at the center of the delaminated region. The loads and the out-of-plane displacements will be compared to finite element and strength of materials predictions. It must be confirmed that there is a close correlation between predicted and experimentally determined loads and out-of-plane displacements because these parameters are vitally important to the modelling of instablity related delamination growth.

In order to determine the shape of the post-buckled region, the shadow moire technique, Fig. 10, will be employed. These results will be used to verify the expected one-dimensional nature of the ITWD problem.

The mechanical properties data along with the Mode I and Mode II fracture toughnesses have been established first in order to design the ITWD specimen. The design of the ITWD specimen with near surface delaminations will be guided by the superposition analysis of Whitcomb [13] summarized in Figures 11 and 12. Analysis developed for this program along with the analysis by Ashizawa [4] and Chai [19] is used to study ITWD specimens with deeply imbedded delaminations.

SHADOW MOIRE OPTICAL SET UP FOR THE THROUGH-WIDTH DELAMINATION SPECIMEN

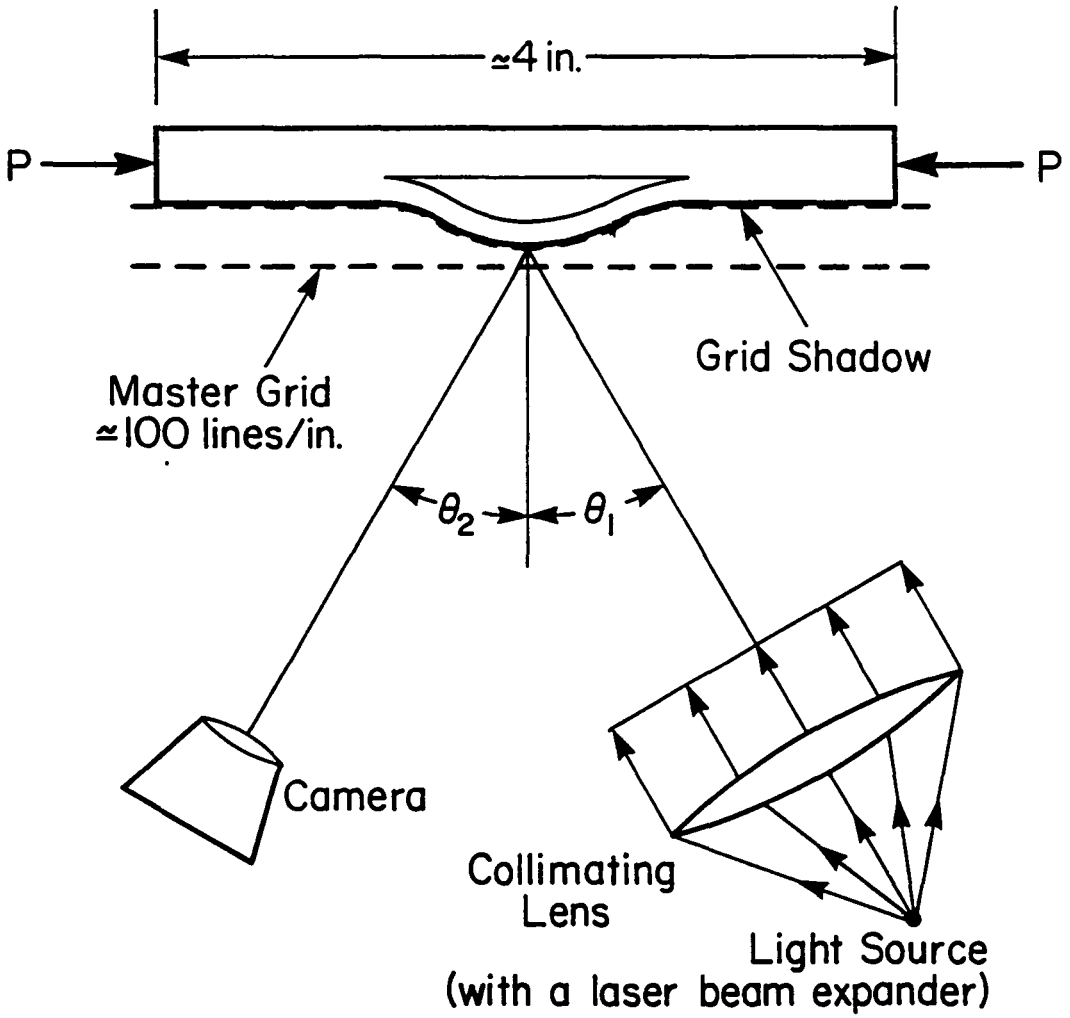

Fig. 10 Shadow Moire optical set up for the through-width delamination specimen.

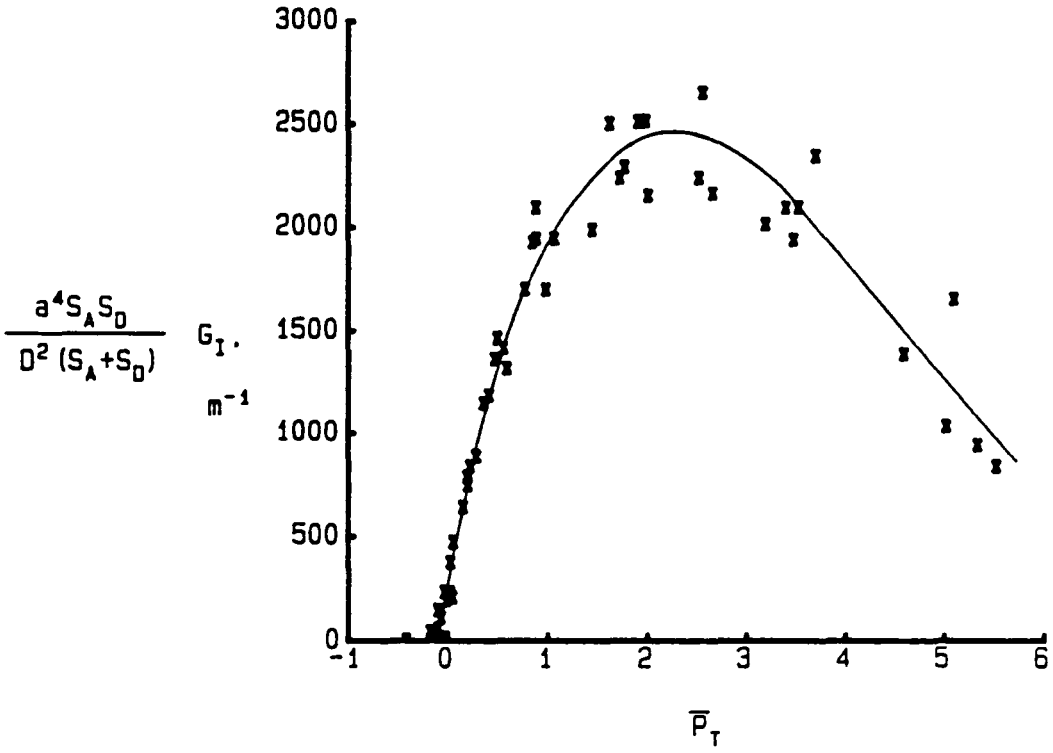

Fig. 11 Normalized Plot of G_I vs. Applied Load [13]

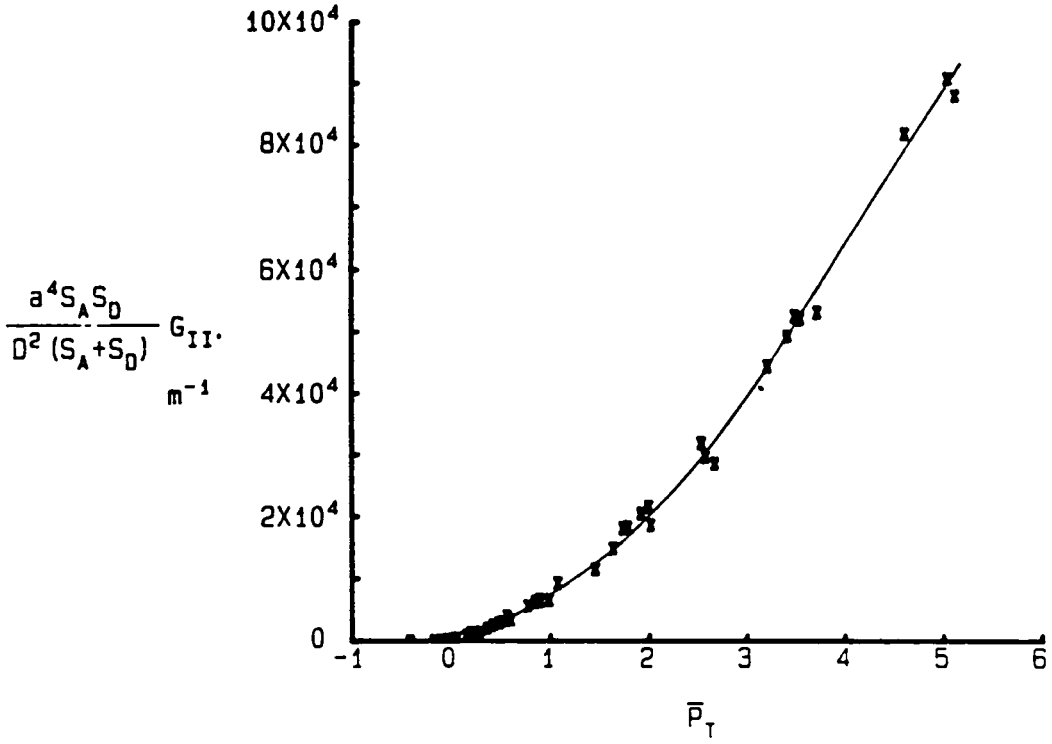

Fig. 12 Normalized Plot of G_{II} vs. Applied Load [13]

3. ANALYSIS

3.1. Finite Element Analysis of the ENF Specimen

Since unstable crack growth is a common occurrence in ENF fracture testing, the data reduction based upon experimentally measuring dC/da (Appendix 1) may not be utilized. To assess the accuracy of the linear beam theory expression currently used to determine G_{II} (see Appendix 1), finite element analysis based on crack closure techniques have been performed.

Linear elastic two dimensional finite element stress analysis of the ENF test specimen was performed by using a four-node plane stress element in the finite element code, ADINA [20]. The finite element model with an exploded view of the crack tip mesh is presented in Figures 13 to 15. The frictionless contact problem was incorporated into the finite element model by connecting duplicate nodes (actually separated by 2.5 x 10^{-3} mm) across the crack interface with non-linear truss elements. The constitutive model employed for the truss elements exhibits zero tensile stiffness and infinite stiffness in compression as shown in Fig. 16.

In all geometries investigated to date, the non-linear truss elements tension release along the entire crack interface except in the vicinity of the support in the three-point bend fixture. Consequently, employing constraint equations for the vertical component of deformation to simulate frictionless contact is not correct, since in this modelling technique, implicit is the assumption that the contact area extends along the entire crack length.

Finite Element Model

- Two-dimensional, plane stress
- ADINA, 3611 nodes, 3318 elements
- Linear elastic
- Frictionless crack interface
- Non-linear truss elements included to identify contact area

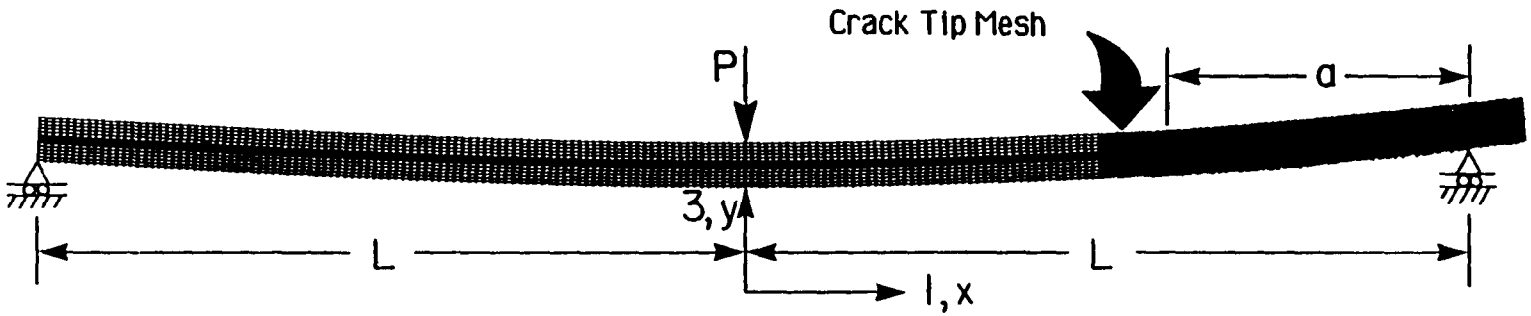

Fig. 13 Finite Element Model of ENF Specimen.

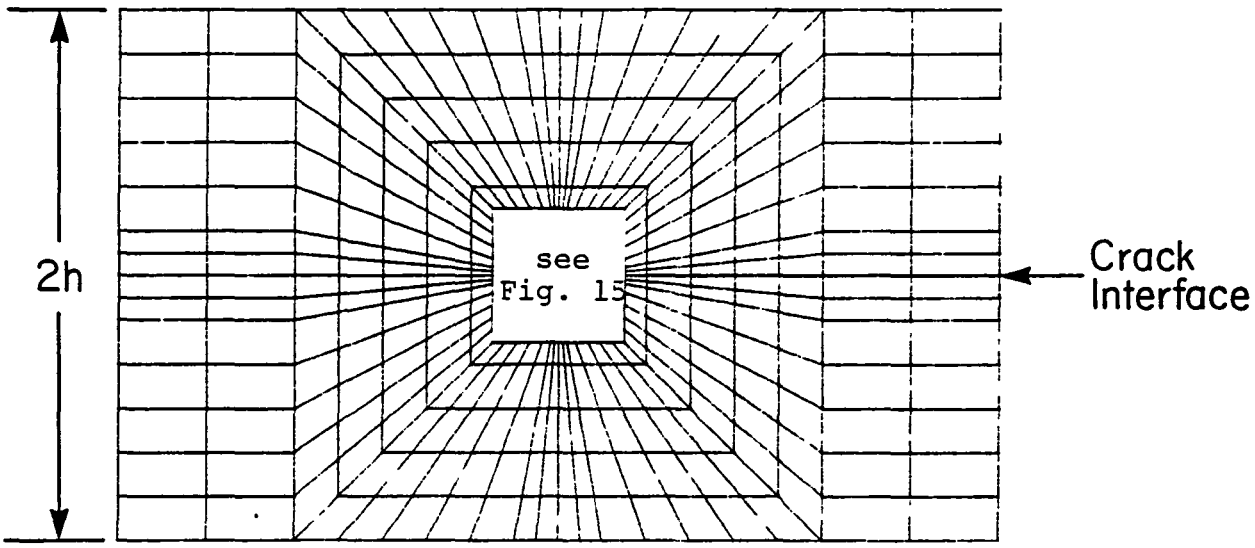

Fig. 14 Finite Element Model in the Vicinity of the Crack Tip

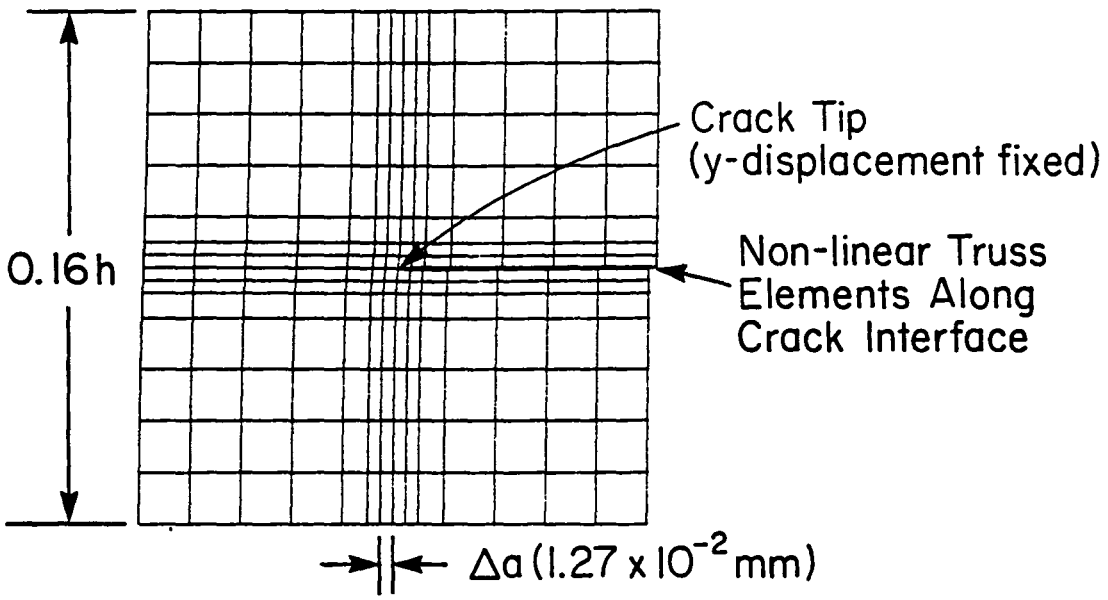

Fig. 15 Deformed shape of Finite Element Model in the vicinity of the crack tip

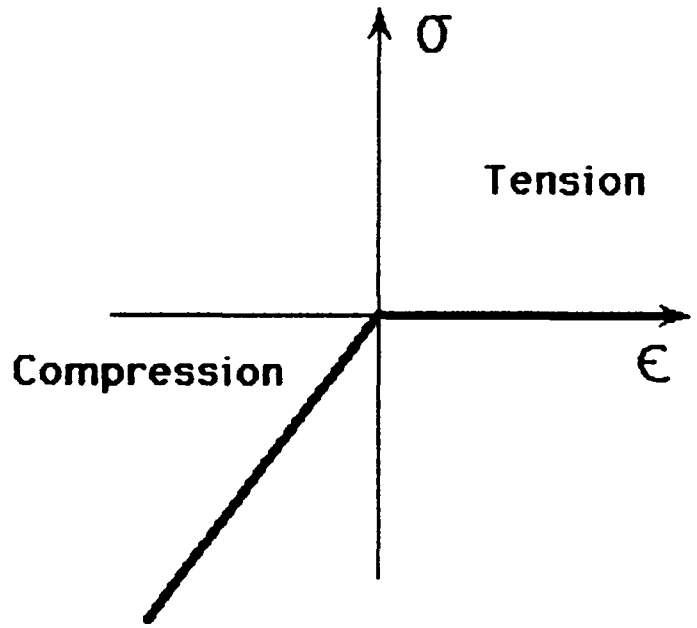

Fig. 16 Constitutive Model for Nonlinear Truss Elements

Material properties employed in the Finite Element modelling are given in Table 8. In Figure 17, the contact force distribution as a function of E_1/G_{13} is presented which shows that the contact area is less than 4h (two laminate thicknesses) in length and centered about the point of load introduction in the fixture. Summation of the contact forces within the contact area verifies that each beam carries an equal load.

3.1.1. Compliance of an orthotropic beam

To assess the accuracy of the finite element model shown in Figures 13 to 15, the compliance for an orthotropic beam with no delamination, loaded in three-point bending is correlated with beam theory expressions derived in Appendix 4. The crack is eliminated from the model by replacing truss element with appropriate two-dimensional elements. The following beam theory expressions are obtained by setting the crack length equal to zero in Equations (10) and (14) of Appendix 4.

$$C_{SH}\ (a=0) = \frac{L^3}{4E_1 wh^3}\left[1 + 1.2\left(\frac{E_1}{G_{13}}\right)\left(\frac{h}{L}\right)^2\right] \qquad (1)$$

$$C_{BT}\ (a=0) = \frac{L^3}{4E_1 wh^3} \qquad (2)$$

Table 9 shows that finite element results agree within 3.5 percent of the simple beam theory expression in Equation (2). The discrepancy, however, is reduced to 0.1 percent by the analytical solution with shear deformation included (Equation 1) as shown in Table 9.

Table 8 Material Properties investigated in the Finite Element Modeling. ($\nu_{12} = \nu_{23} = \nu_{13} = 0.3$)

	Material 1	Material 2	Material 3
E_1 GPa	137.8	126.1	115.1
E_2 GPa	10.0	9.7	9.7
E_3 GPa	10.0	9.7	9.7
		E_1/G_{13}	
	33.3	18.3	12.8
		26.9	25.7
		122.0	51.4
		183.0	

Table 9 Compliance of an Orthotropic Beam under Three Point Bending. Material 1, $E_1/G_{13} = 33$. L = 50.8 mm, h = 1.52 mm, w = 25.4 mm.

$\frac{C_{FE}}{C_{BT}}$	$\frac{C_{FE}}{C_{SH}}$	$\frac{C_{SH}}{C_{BT}}$
1.035	0.999	1.035

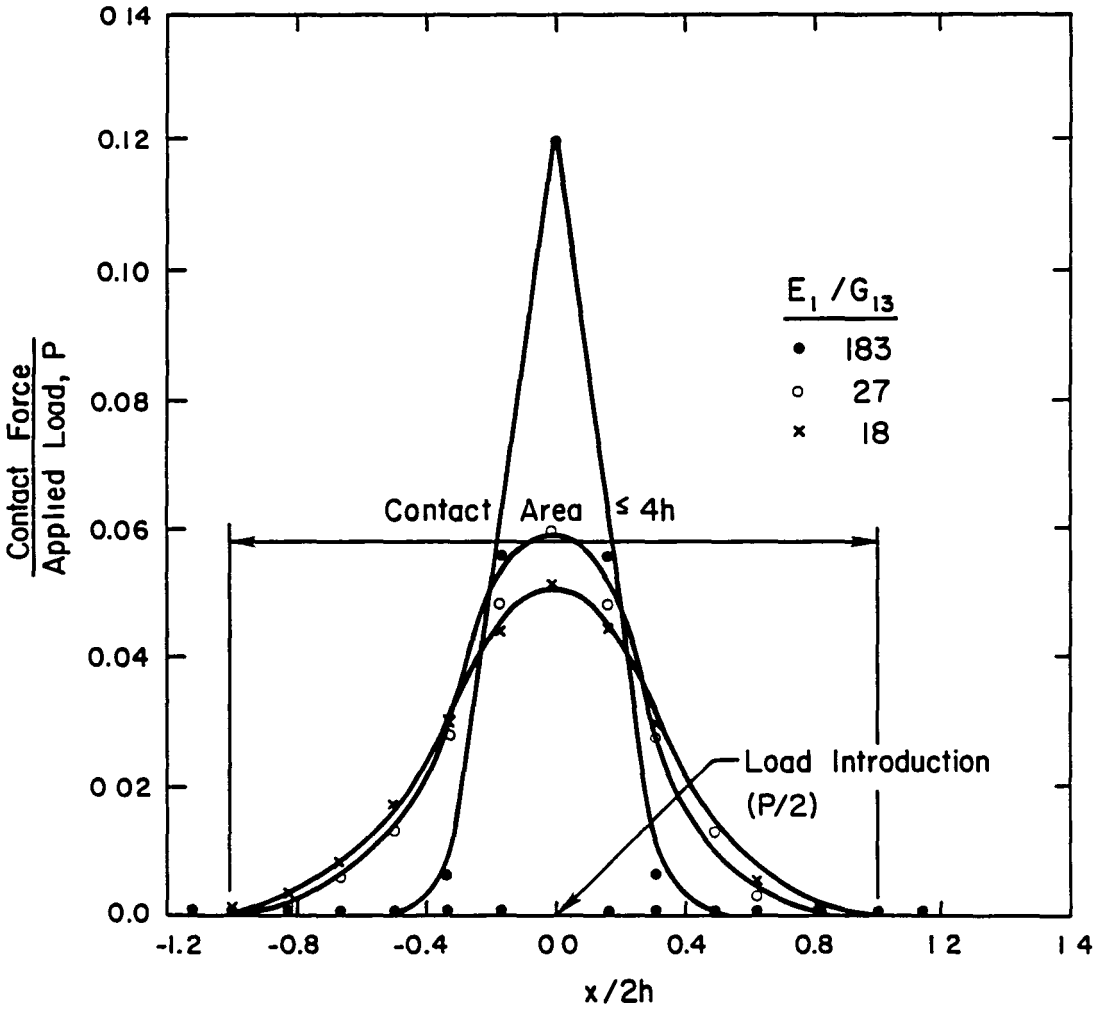

Fig. 17 Contact Normal Force distribution (Material 2)

3.1.2. Compliance of the ENF Specimen

In Appendix 4, the contribution of shear deformation to the ENF compliance has been derived yielding the following expression:

$$C_{SH} = \frac{2L^3 + 3a^3}{8E_1wh^3}\left[1 + \frac{2(1.2L + 0.9a)h^2E_1}{(2L^3 + 3a^3)G_{13}}\right] \qquad (3)$$

The parametric study investigates the influence of shear deformation (E_1/G_{13}) with the material properties presented in Table 8 as well as the influence of span, (L), crack length (a) and laminate thickness (2h) on specimen compliance.

The results, displayed in Tables 10-13, show that in general, finite elements results are more compliant than the simple beam theory expression for C_{BT}. C_{BT} appears to converge to finite element results for small E_1/G_{13} ratios.

Equation (2) for ENF compliance with shear deformation included provides excellent agreement (less than 4 percent difference) with finite element results in all cases investigated in the parametric study. Experimental results reported in [15] have been for 24 ply unidirectional graphite epoxy laminates (h = 1.52 - 1.70 mm) with a = 19.3 mm, L = 38.1 or 50.8 mm and E_1/G_{13} = 26. For this particular configuration, finite element results are within two and seven percent of C_{SH} and C_{BT} respectively. Reasonable agreement between experimental compliance and beam theory has been observed [16], see Fig. 18, which generates confidence in the finite element model as an accurate description of the ENF fracture specimen.

Table 10 Compliance of the ENF Specimen
Comparison of Finite Element Results with Beam Theory Results, Material 3, L = 38.1 mm, a = 12.7 mm.

	$\frac{E_1}{G_{13}}$	$\frac{C_{FE}}{C_{BT}}$	$\frac{C_{FE}}{C_{SH}}$
h = 1.70 mm	12.8	1.037	1.001
	25.7	1.071	0.998
	51.4	1.134	0.990
h = 2.62 mm	12.8	1.084	0.998
	25.7	1.158	0.988
	51.4	1.301	0.968

Table 11 Compliance of the ENF Specimen.
Comparison of Finite Element Results with Beam Theory Results. L = 38.1 mm, a = 19.3 mm.

	$\frac{E_1}{G_{13}}$	$\frac{C_{FE}}{C_{BT}}$	$\frac{C_{FE}}{C_{SH}}$
Material 2	18.3	1.049	1.008
h = 1.52 mm	26.9	1.067	1.007
	122.0	1.246	0.981
	183.0	1.353	0.963
h = 1.70 mm	26.9	1.081	1.007
Material 3	12.8	1.043	1.008
h = 1.70 mm	25.7	1.078	1.006
	51.4	1.140	0.999
Material 3	12.8	1.092	1.008
h = 2.62 mm	25.7	1.165	0.997
	51.4	1.301	0.974

Table 12 Compliance of the ENF Specimen.
Comparison of Finite Element Results with Beam Theory Results. L = 38.1 mm, a = 25.4 mm

	$\frac{E_1}{G_{13}}$	$\frac{C_{FE}}{C_{BT}}$	$\frac{C_{FE}}{C_{SH}}$
Material 2	18.3	1.052	1.015
h = 1.52 mm	26.9	1.070	1.016
	122.0	1.235	0.994
	183.0	1.330	0.974
Material 3	12.8	1.047	1.015
h = 1.70 mm	25.7	1.081	1.016
	51.4	1.140	1.011
Material 3	12.8	1.094	1.018
h = 2.62 mm	25.7	1.162	1.010
	51.4	1.285	0.987

Table 13 Compliance of the ENF Specimen.
Comparison of Finite Element Results with Beam Theory Results. L = 50.8 mm, a = 25.4 mm

	$\frac{E_1}{G_{13}}$	$\frac{C_{FE}}{C_{BT}}$	$\frac{C_{FE}}{C_{SH}}$
Material 2	18.3	1.031	1.008
h = 1.52 mm	26.9	1.042	1.008
	122.0	1.149	0.997
	183.0	1.212	0.987
Material 3	12.8	1.028	1.007
h = 1.70 mm	25.7	1.049	1.009
	51.4	1.087	1.006
Material 3	12.8	1.059	1.011
h = 2.62 mm	25.7	1.103	1.008
	51.4	1.184	0.996

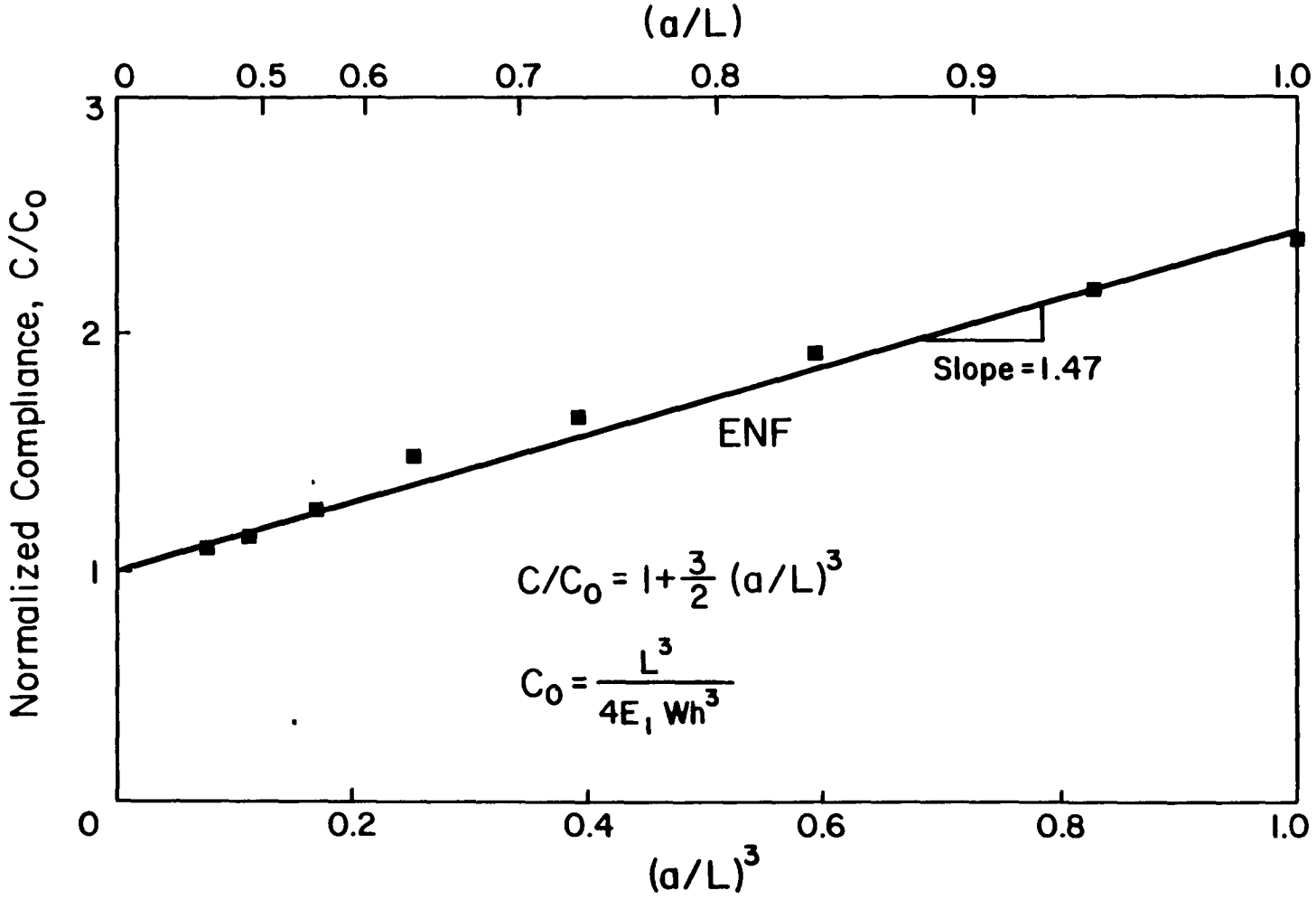

Fig. 18 Compliance as a Function of Crack Length for the ENF Specimen [16]

3.1.3. Strain Energy Release Rate of the ENF Specimen

One of the objectives with the finite element analysis of the ENF specimen was to evaluate the strain energy release rate. Two approaches, the crack closure and compliance techniques, have been investigated numerically. Fig. 19 shows the finite element mesh close to the crack tip. With the crack closure technique [21] the components G_I and G_{II} of the strain energy release rate may be determined,

$$G_I = \lim_{\Delta a \to 0} \frac{1}{2\Delta a} F_c(V_c - V_d) \qquad (4)$$

$$G_{II} = \lim_{\Delta a \to 0} \frac{1}{2\Delta a} T_c(U_c - U_d) \qquad (5)$$

where F_c and T_c are the normal and tangential forces required to hold nodes c and d together. Analogously, the quantities $(V_c - V_d)$ and $(U_c - U_d)$ are the normal and tangential deformations corresponding to Mode I and Mode II crack propagation. Two finite element computations are required for each strain energy release rate calculation.

In all cases investigated to date, the quantity $(V_c - V_d)$ in Equation (4) is identically zero for the finite element mesh presented in Figure 15. Consequently, the ENF fracture specimen is a pure Mode II test within the constraints of small deflection theory.

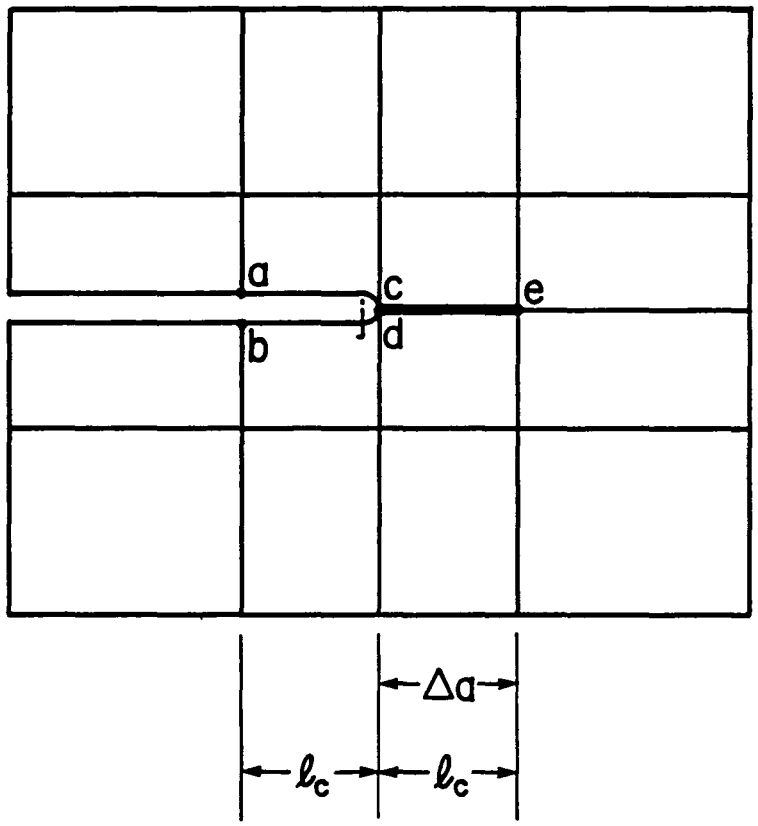

Fig. 19 Finite Element Mesh Near Crack Tip.

In finite element representation, the compliance method yields the following expression for the total strain energy release rate,

$$G = \lim_{\Delta a \to 0} \frac{P_i^2}{2w} \frac{(C_i(a+\Delta a) - C_i(a))}{\Delta a} \qquad (6)$$

where $C_i = V_i/P_i$. V_i is the vertical component of deformation resulting from the applied load, P_i, at node i. This technique also requires two finite element computations.

The compliance technique (Equation 6) yields identical results with the crack closure technique (Equations 4 and 5) confirming that $G_I = 0$ and that the ENF specimen is a viable Mode II Specimen.

In Fig. 20, the stress state in the vicinity of the crack tip is presented. Stresses for each element are extrapolated from the Gauss points to nodal points lying along the crack interface. An individual node has, in general, stress output from four adjacent elements. Minimal stress discontinuities between element output indicated that the model has sufficient mesh refinement. The results presented in Fig. 20 correspond to the average nodal stress components.

The flexure and interlaminar normal stresses are identically zero ($K_I = 0$) and the interlaminar shear stress exhibits the expected singularity. Consequently, the ENF fracture specimen is a pure Mode II test in agreement with the strain energy release rate calculations.

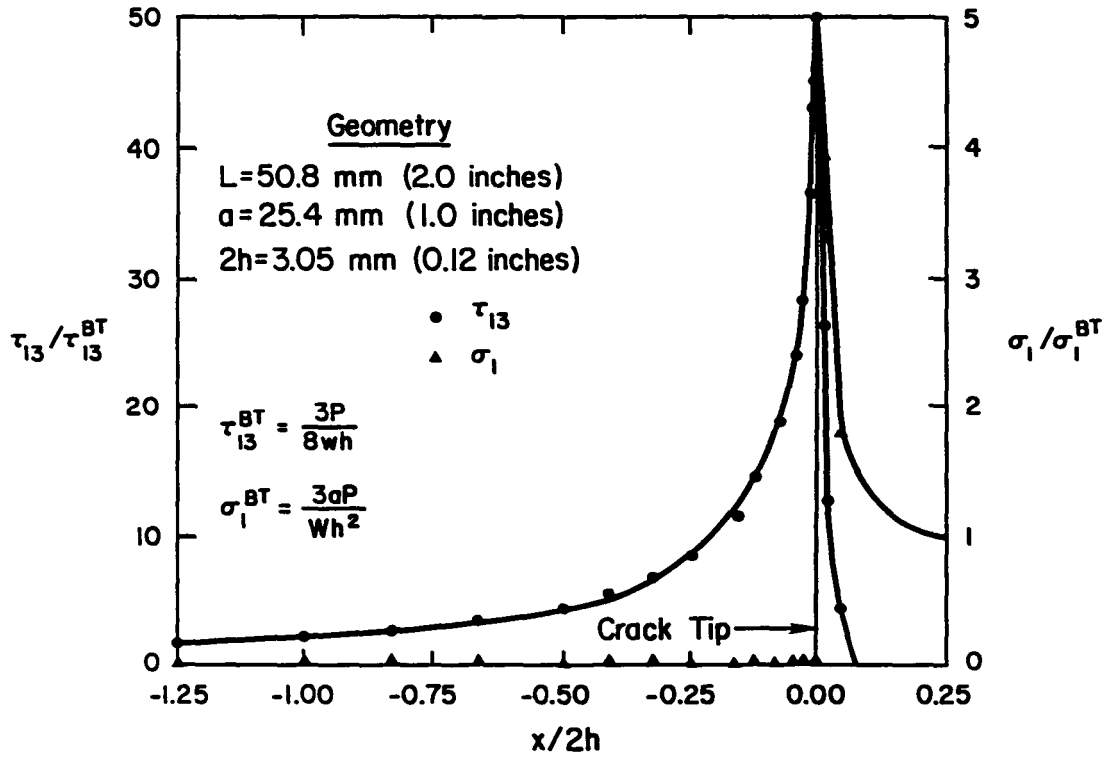

Fig. 20 Stress Distribution Ahead of the Crack Tip for the ENF Specimen

In Appendix 4, the influence of shear deformation on the strain energy release rate, G_{II}, for the ENF specimen has been derived from beam theory yielding the following expressions:

$$G_{II}^{SH} = \frac{9a^2P^2}{16E_1w^2h^3}\left[1 + 0.2(E_1/G_{13})(h/a)^2\right] \quad (7)$$

$$G_{II}^{BT} = 9a^2P^2/(16E_1w^2h^3) \quad (8)$$

where G_{II}^{SH} is the strain energy release rate including shear deformation and G_{II}^{BT} is the same quantity where shear deformation is neglected.

In Tables 14 to 17, finite element strain energy release rate calculations are compared with beam theory results. In general, the finite element results diverge significantly from G_{II}^{BT} and G_{II}^{SH} for any combination of specimen geometry and material properties which enhances shear deformation. Inspection of the results presented in Tables 14 to 17 indicates that errors approaching 200 percent are typical for these extreme cases. Although the inclusion of shear deformation in the derivation of G_{II}^{SH} reduces the discrepancy between beam theory and finite element results, 20 to 40 percent errors are still realized for the typical graphite fiber composite ($E_1/G_{13} \approx 26$).

The beam theory solution presented in Appendix 4 which provides reasonable estimates of global specimen compliance are

Table 14 Strain Energy Release Rate for the ENF Specimen. Comparison of Finite Element Results with Beam Theory Results. Material 3, L = 38.1 mm, a = 12.7 mm

	$\frac{E_1}{G_{13}}$	$\frac{G_{II}^{FE}}{G_{II}^{BT}}$	$\frac{G_{II}^{FE}}{G_{II}^{SH}}$
h = 1.70 mm	12.8	1.068	1.021
	25.7	1.263	1.156
	51.4	1.604	1.354
h = 2.62 mm	12.8	1.324	1.194
	25.7	1.576	1.294
	51.4	2.025	1.410

Table 15 Strain Energy Release Rate for the ENF Specimen. Comparison of Finite Element Results with Beam Theory Results. L = 38.1 mm, a = 19.3 mm

	$\frac{E_1}{G_{13}}$	$\frac{G_{II}^{FE}}{G_{II}^{BT}}$	$\frac{G_{II}^{FE}}{G_{II}^{SH}}$
Material 2	18.3	1.232	1.205
h = 1.52 mm	26.9	1.342	1.298
	122.0	2.311	2.006
	183.0	2.835	2.308
h = 1.70 mm	26.9	1.402	1.346
Material 3	12.8	1.198	1.175
h = 1.70 mm	25.7	1.375	1.322
	51.4	1.682	1.558
Material 3	12.8	1.342	1.282
h = 2.62 mm	25.7	1.554	1.420
	51.4	1.926	1.620

Table 16 Strain Energy Release Rate for the ENF Specimen. Comparison of Finite Element Results with Beam Theory Results. L = 38.1 mm, a = 25.4 mm

	$\frac{E_1}{G_{13}}$	$\frac{G_{II}^{FE}}{G_{II}^{BT}}$	$\frac{G_{II}^{FE}}{G_{II}^{SH}}$
Material 2	18.3	1.342	1.324
h = 1.52 mm	26.9	1.448	1.420
	122.0	2.368	2.177
	183.0	2.860	2.527
Material 3	12.8	1.290	1.275
h = 1.70 mm	25.7	1.455	1.422
	51.4	1.750	1.673
Material 3	12.8	1.366	1.330
h = 2.62 mm	25.7	1.559	1.478
	51.4	1.890	1.704

Table 17 Strain Energy Release Rate for the ENF Specimen. Comparison of Finite Element Results with Beam Theory Results. L = 50.8 mm, a = 25.4 mm

	$\frac{E_1}{G_{13}}$	$\frac{G_{II}^{FE}}{G_{II}^{BT}}$	$\frac{G_{II}^{FE}}{G_{II}^{SH}}$
Material 2	18.3	1.138	1.123
h = 1.52 mm	26.9	1.237	1.214
	122.0	2.122	1.950
	183.0	2.607	2.303
Material 3	12.8	1.113	1.100
h = 1.70 mm	25.7	1.277	1.248
	51.4	1.558	1.489
Material 3	12.8	1.269	1.255
h = 2.62 mm	25.7	1.460	1.427
	51.4	1.790	1.614

simply first order approximations to an elasticity solution (not presently available) for the calculation of strain energy release rates. The derivation of the beam theory expressions in Appendix 4 makes no attempt to include the intense shear deformation occuring at the crack tip. Consequently, it should not be surprising that beam theory provides conservative estimates of the strain energy release rate. This will be further discussed in Section 3.1.7.

An experimental observation reported by Murri and O'Brien [17] which appears to support the finite element results presented herein, is an absolute dependence of P_{cr}, the load at delamination onset, on span (L). For a given crack length, finite element results predict an absolute span dependence which is not predicted by beam theory. For example (Material 3, $E_1/G_{13} \approx 25.7$, h = 1.70 mm),

$$\frac{G_{II}^{FE}}{G_{II}^{BT}} = 1.28 \quad (L = 50.8 \text{ mm}, a = 25.4 \text{ mm}) \tag{9}$$

and

$$\frac{G_{II}^{FE}}{G_{II}^{BT}} = 1.46 \quad (L = 38.1 \text{ mm}, a = 25.4 \text{ mm}) \tag{10}$$

Since G_{IIC} is assumed to be a material property, the critical load at the onset of crack propagation would be approximately seven percent greater for the longer span since,

$$\frac{P_{cr}(L = 50.8 \text{ mm})}{P_{cr}(L = 38.1 \text{ mm})} = \left[\frac{1.46}{1.28}\right]^{1/2} = 1.07 \tag{11}$$

Murri and O'Brien [17] have reported a 13 percent increase of P_{cr} for the two spans investigated although their results are for a different crack length ($a \approx 19$ mm) and material system (T300/5208 graphite/epoxy). In any event, finite element results are in qualitative agreement with experimental observations that cannot be predicted by beam theory.

3.1.4. Sensitivity of ENF Strain Energy Release Rate on Crack Offset

In the fabrication of the ENF fracture specimen, implanted defects of Teflon, Kapton or Aluminum are placed at the laminate midsurface to provide a starter crack for subsequent testing. As a consequence of processing, however, the implanted defect is not likely to remain at the laminate midsurface. In Table 18, the sensitivity of the ENF strain energy release rate on the crack offset from the specimen midplane is presented for a typical 24 ply unidirectional graphite/epoxy laminate. The maximum realistic offset investigated in the present study is assumed to be one nominal ply thickness where the delamination is displaced toward both the tensile and compressive faces of the flexural specimen. Finite element results indicate that the ENF fracture specimen remains a pure Mode II test ($G_I = 0$). The strain energy release rate, G_{II}^{FE}, decreases by less than three percent of the midplane value for the offset and geometry investigated. Consequently, the ENF fracture specimen appears to be relatively insensitive to delamination offset and remains a pure Mode II test.

Table 18 Sensitivity of ENF Strain Energy Release Rate on Crack Offset From Laminate Midplane, Material 3, L = 50.8 mm, a = 25.4 mm and h = 1.70 mm

z/h*	$\frac{C^{FE}(z)}{C^{FE}(0)}$	$\frac{G_{II}^{FE}(z)}{G_{II}^{FE}(0)}$
+0.075	0.997	0.976
-0.075	0.997	0.976

*z/h = ±0.075 corresponds to the delamination displaced one ply thickness in the compressive (+) or tensile (-) direction in the ENF specimen.

3.1.5. Finite Element/Beam Theory-based data reduction schemes for the ENF Specimen

In an attempt to generalize finite elements results, non-dimensional expressions for the strain energy release rate are identified to accommodate slight variations in geometry or lamina properties that will inevitably arise in an experimental program to characterize G_{IIC}. Finite element results are assumed to be of the non-dimensional form derived in Appendix 4,

$$\frac{G_{II}^{FE}}{G_{II}^{BT}} = \left[\alpha+\beta\left(\frac{E_1}{G_{13}}\right)\left(\frac{h}{a}\right)^2\right] \qquad (12)$$

where

$$G_{II}^{BT} = \frac{9a^2P^2}{16E_1w^2h^2} \qquad (13)$$

α and β are parameters determined by a least squares fit to the numerical results presented in Tables 15 to 17 for spans of 38.1 and 50.8 mm (a/L = 0.5) to more accurately reflect the influence of shear deformation. In Fig. 21, G_{II}^{FE}/G_{II}^{BT} is indeed found to be a linear function of $(E_1/G_{13})(h/a)^2$ for a 24 ply laminate. Consequently, for a/L = 0.5,

$$G_{II}^{FE}/G_{II}^{BT} = \left[1.045 + 1.657\ (E_1/G_{13})(h/a)^2\right] \quad L = 38.1 \text{ mm} \qquad (14)$$

and

$$G_{II}^{FE}/G_{II}^{BT} = \left[0.967 + 2.644(E_1/G_{13})(h/a)^2\right] \quad L = 50.8 \text{ mm} \qquad (15)$$

Equations (14) and (15) accurately predict strain energy release rates for a broad range of the flexural modulus (E_1) and

E_1/G_{13} ratios as shown in Figure 21. These equations, however, are restricted to slight perturbation in a/L and laminate thickness. Subject to these constraints, the utility of Equations (14) and (15) cannot be overstated since the experimentalist does not need to perform a finite element analysis of each ENF specimen exhibiting slight variations in geometry to calculate G_{IIC}.

In most instances, specimen compliance will be measured during the fracture test directly by the crosshead displacement or appropriate instrumentation such as the LVDT shown schematically in Figure 6. In this situation, it is convenient to express E_1 in terms of the specimen compliance, C, instead of the absolute flexural modulus which requires an independent test. Assuming $C = C_{SH}$, E_1 can be expressed as a function of C by using Equation (3) for C_{SH}:

$$1/E_1 = \frac{8wh^3C}{[(2L^3 + 3a^3) + 2(1.2L + 0.9a)h^2(E_1/G_{13})]} \qquad (16)$$

The E_1/G_{13} value needed in the right hand side of Equation (16) may be obtained from literature data for the actual material system. As a first order approximation E_1 and G_{13} may be set equal to the tensile modulus and the in-plane shear modulus (G_{12}) respectively.

Equation (16) may then be substituted into Equation (8) for yielding the desired expression:

$$G_{II}^{BT} = \frac{9a^2P^2C}{2w[(2L^3 + 3a^3) + 2(1.2L + 0.9a)h^2(E_1/G_{13})]} \qquad (17)$$

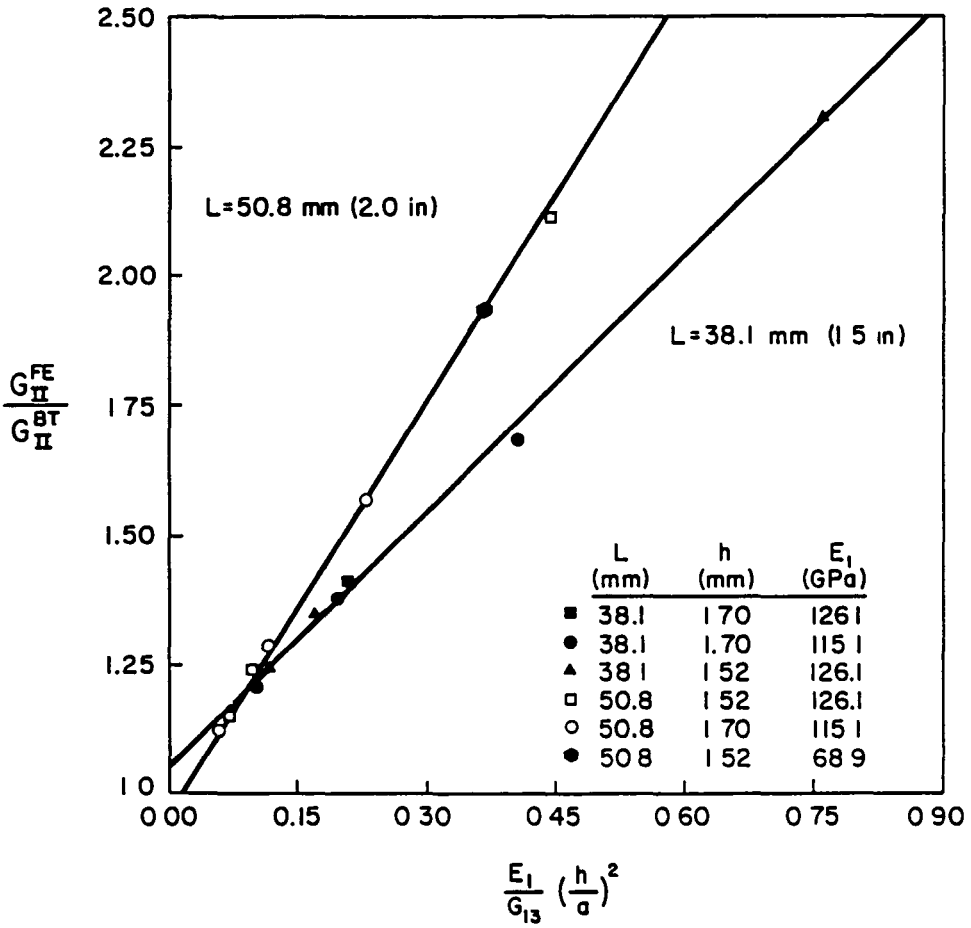

Fig. 21 Influence of Shear Deformation on Strain Energy Release Rate (a/L = 0.5).

Note that by neglecting the contribution of shear deformation, Equation (17) simplifies to the expressions reported in [16],

$$G_{II}^{BT} = \frac{9a^2P^2C}{2w(2L^3 + 3a^3)} \qquad (18)$$

Consequently, an improved data reduction scheme which retains the simplicity of beam theory and includes the accuracy of the finite element strain energy release rate calculations is presented. The procedure utilizes Equation (14) or (15) for G_{II}^{FE}/G_{II}^{BT} in conjunction with Equation (17) where G_{II}^{BT} is expressed in terms of the experimental compliance of the ENF test specimen.

3.1.6. Influence of friction on the Compliance and Strain Energy Release Rate of the ENF Specimen.

In general, an incremental formulation must be employed to investigate contact problems with friction [22, 23]. Linear elastic behavior and quasi-static application of the load are basic assumptions. The solution is based upon the minimization of the total incremental potential energy satisfying displacement constraints and the constitutive relations governing friction in the contact region where sticking, slipping and tension release are possible between two bodies in contact [23]. Non-conservative frictional forces are treated as known piecewise conservative tangential nodal forces calculated from the previous iteration. In a general problem, the size of the contact region cannot be predicted a priori and in all likelihood will vary with the applied load. Consequently, most contact algorithms consist of an iterative procedure within each load increment to find the contact area.

In the present investigation of the ENF fracture specimen, Coulomb's law of friction is utilized. The coefficient of static friction corresponds to sticking of the crack surfaces so that no relative sliding in the contact area is permissable. Sticking effects, due to static friction however, are not observed during loading and unloading of the test specimen. Consequently, static friction is neglected in the present model. The coefficient of sliding friction, μ, however, would reduce the specimen compliance upon loading and may be difficult to detect in an experiment.

Frictional forces, T_i, opposing the sliding deformation, are evaluated from the nodal normal forces, P_i, in the contact area from the frictionless solution, see Fig. 22,

$$T_i = \mu P_i \qquad (19)$$

Frictional forces are then applied as horizontal nodal forces as shown schematically in Figure 22. Inspection of finite element results show that the normal forces and contact area remain unchanged in the presence of the tangential loads. Consequently, no further iterations are required and the problem is solved within the constraints of small deflection theory.

In Table 19, the influence of sliding friction on the ENF compliance and strain energy release rate is presented. Two coefficients of sliding friction (μ= 0.25, 0.50) are investigated in the finite element model for a variety of crack lengths and laminate thicknesses to evaluate the validity of the non-dimensional parameter derived in Appendix 5 (Equation (11)). Results presented in Table 19, non-dimensionalized by the corresponding frictionless solution, show that $C_{FE}(\mu)$ and

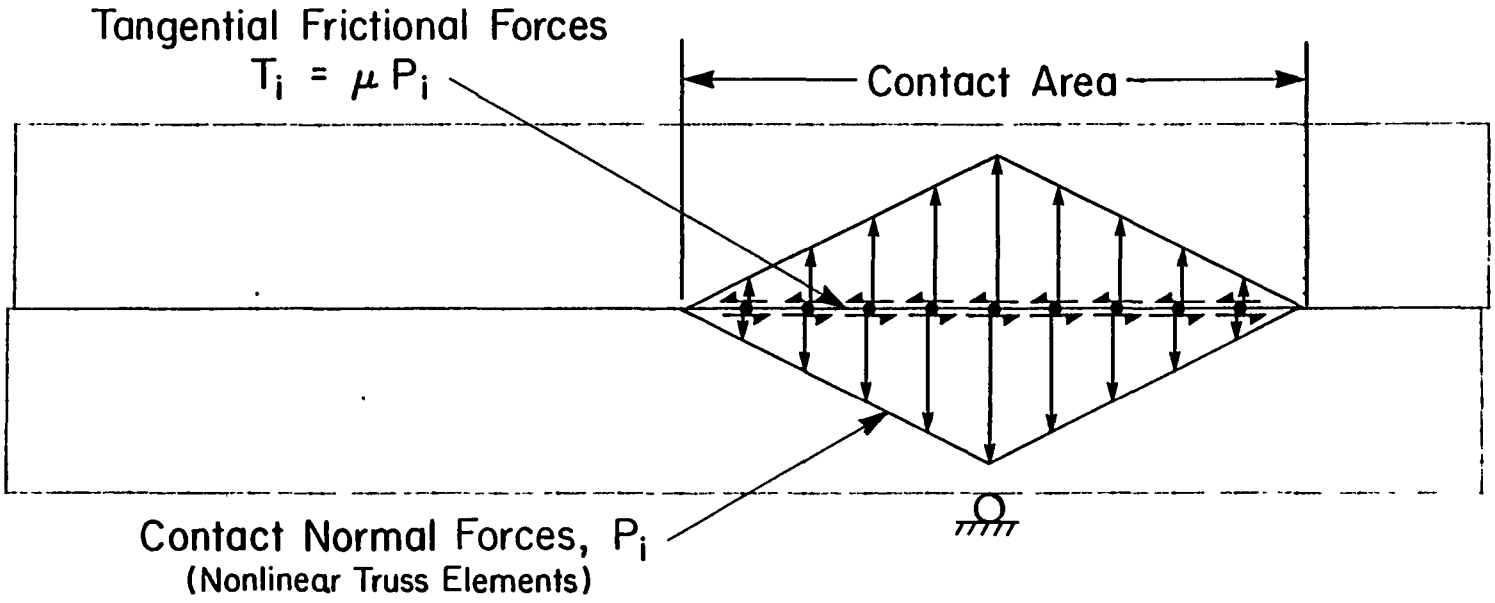

Fig. 22 Finite Element Analysis of Friction: Nodal Forces

Table 19 Influence of Friction on ENF Compliance and Strain Energy Release Rate (Material 3, E_1/G_{13} = 25.7)

	μ	$\frac{C_{FE}(\mu)}{C_{FE}(0)}$	$\frac{G_{II}^{FE}(\mu)}{G_{II}^{FE}(0)}$	$\frac{G_{II}^{FE}(0)-G_{II}^{FE}(\mu)}{G_{II}^{BT}}$	$\frac{4}{3}\mu\frac{h}{a}$	$\frac{\Delta_u^{FE}}{\Delta_u^{BT}}$
L=50.8 mm	0	1.000	1.000	0	0	1.075
a=25.4 mm	0.25	0.997	0.986	0.018	0.022	1.051
h=1.70 mm	0.50	0.994	0.976	0.031	0.045	1.028
L=50.8 mm	0	1.000	1.000	1.000	0	-
a=25.4 mm	0.25	0.996	0.983	0.025	0.034	1.075
h=2.62 mm	0.50	0.992	0.965	0.051	0.069	1.033
L=38.1 mm	0	1.000	0	0	0	-
a=25.4 mm	0.5	0.990	0.977	0.033	0.045	1.028
h=1.70 mm						
L=38.1 mm	0	1.000	1.000	0	0	-
a=12.7 mm	0.5	0.996	0.952	0.061	0.089	1.039

$G_{II}^{FE}(\mu)$ decrease with μ as expected. For the geometries considered, $C_{FE}(\mu)$ and $G_{II}^{FE}(\mu)$ are reduced by no more than one and five percent, respectively. In Fig. 23, finite element results are correlated with the non-dimensional parameter derived in Appendix 5,

$$\frac{G_{II}(\mu=0) - G_{II}(\mu)}{G_{II}^{BT}} = \frac{4\mu h}{3a}$$

Numerical results exhibit linear behavior over the entire domain and the analytical results are shown to provide a conservative upper bound on the effects of friction on G_{II}. The magnitude of the sliding deformation, Δu^{BT}, employed in the derivation of the non-dimensional parameter is also presented in Table 19. It is observed that the finite element results show larger degree of sliding than the beam theory results which must be due to the intense stress field at the crack tip. Furthermore, the amount of sliding decreases with increased coefficient of friction.

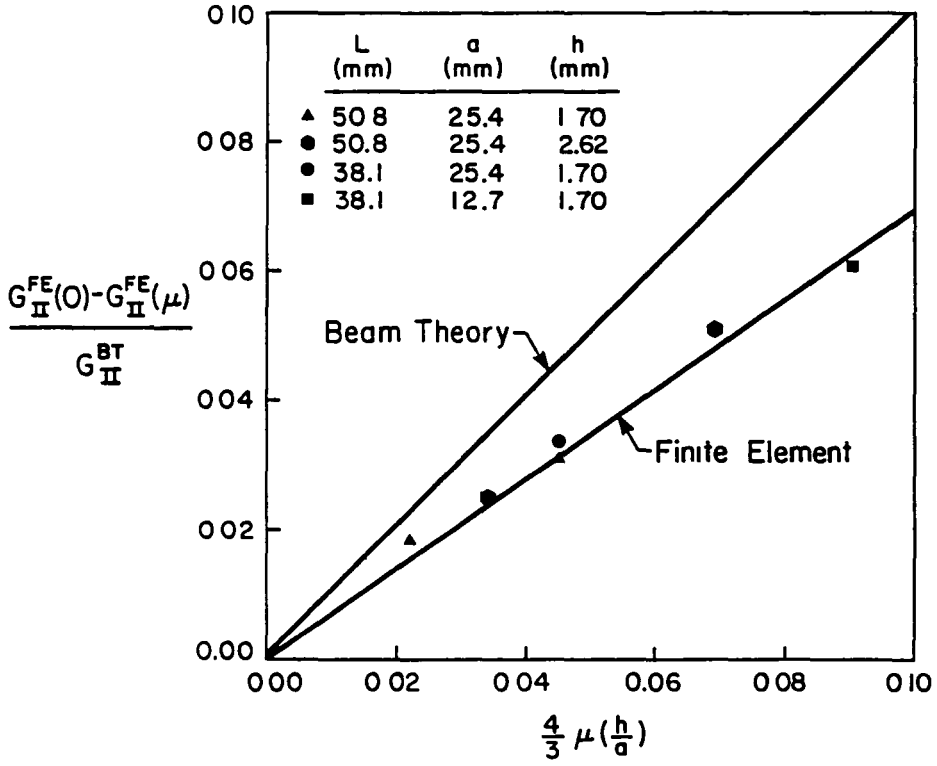

Fig. 23 Influence of Friction on ENF Strain Energy Release Rate

3.1.7. Discussion of ENF Data Reduction Scheme

It may appear contradictory that even if excellent agreement between compliance calculated from beam theory with shear deformations included and finite element is noted there is such a large discrepancy between the strain energy release rate calculated from the two methods. However, the strain energy is determined uniqued by dC/da not by the absolute specimen compliance, C. In an experimental program, dC/da should be ideally approximated by

$$\frac{dC}{da} = \lim_{\Delta a \to 0} \frac{\Delta C}{\Delta a} \qquad (20)$$

Unfortunately, Δa must be chosen sufficiently large so that ΔC can be measured accurately. The minimum Δa is limited by the sensitivity and experimental error induced by the instrumentation employed to measure specimen compliance. Consequently, most experimental approaches consist of measuring compliance for a variety of crack lengths where Δa is typically 6 to 13 mm. Experimental results are then curve fitted to a function based upon simple beam theory (Appendix 4) assumed to accurately model the compliance-crack length response,

$$C_{BT} = \frac{2L^3 + 3a^3}{8E_1 wh^3} \qquad (21)$$

This experimental approach is illustrated in Figure 18 where dC/da is determined from the average slope of compliance versus a^3, (see Appendix 1). The onset of delamination growth, however, is governed by the pointwise variation in dC/da not the averaged response over a large range of crack lengths. Consequently, the validity of this approach is determined solely by the accuracy of

the solution to predict the pointwise variation in dC/da.

On the average, the experimental data appear to fit the assumed form quite well over the range of a/L = 0 to 1. In practice, ENF fracture testing is limited to delamination lengths in the range of $0.5 < a/L < 0.75$ to minimize load introduction effects. In this region, however, the experimental rate of change of compliance with crack length, is significantly different than the beam theory prediction as shown in Figure 18, even though the absolute compliance is adequately predicted by the beam theory expression. Admittedly, the response exhibited by the data in Figure 18 may be simply attributed to experimental errors in compliance measurements. Finite element results, however, substantiate the trend observed in Figure 18 and the beam theory data reduction schemes provide an average value which is too conservative in the determination of the fracture toughness.

To further emphasize this point, finite element compliance (C_{FE}) minus the beam theory compliance (C_{SH}) normalized with the simple beam theory compliance (C_o) is plotted in Figs. 24 and 25. The results clearly illustrate that dC_{FE}/da (and therefore G_{II}^{FE}) is significantly greater than dC_{SH}/da even though $C_{FE}/C_{SH} < 1.04$ for all cases investigated in the parametric study (see Tables 10 to 13). A logical extension of the present work would be to analyze larger crack lengths to further examine the validity of the beam theory results and relate the finite element compliance to experimental compliance over a range of crack lengths and ENF geometries.

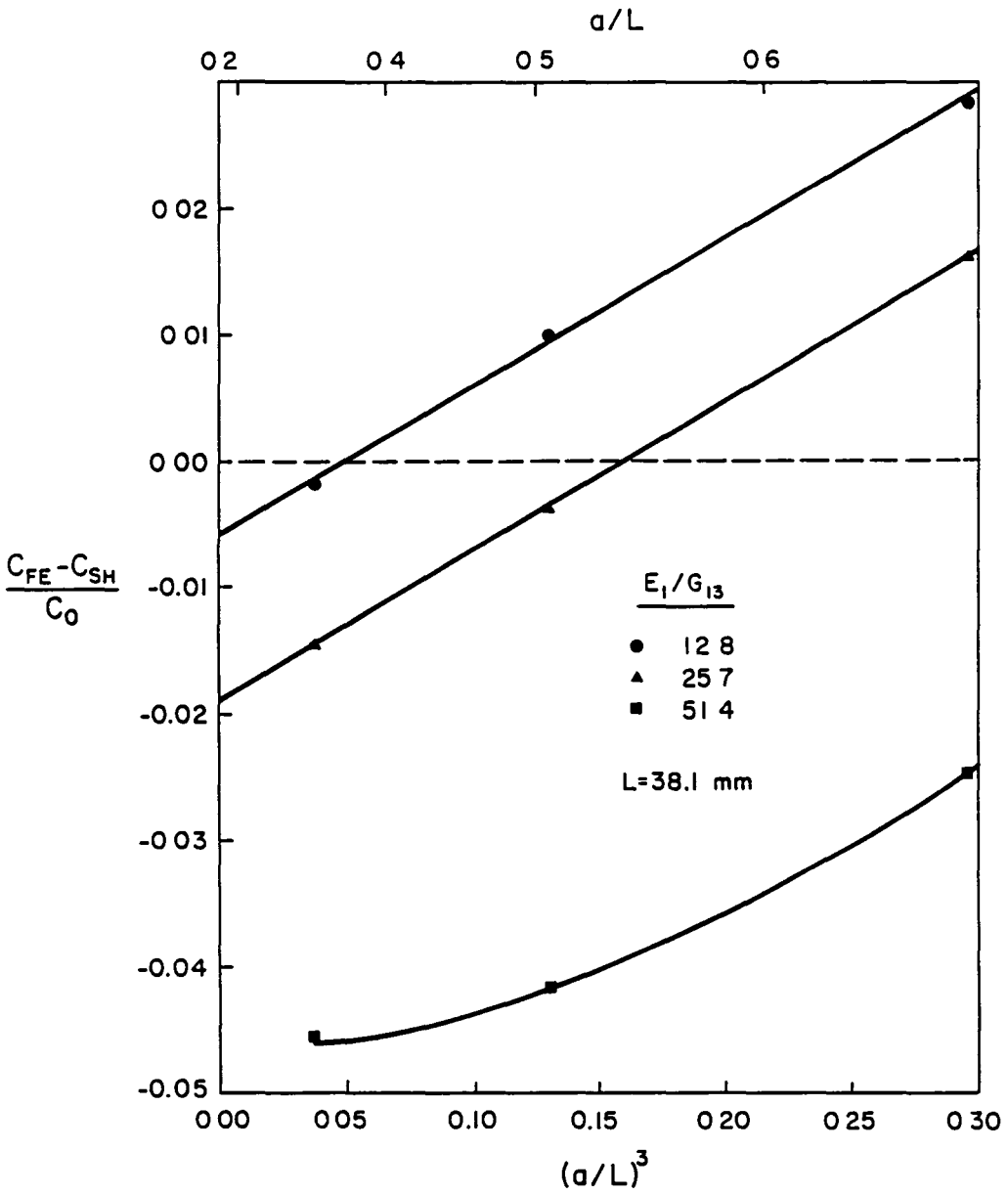

Fig. 24 ENF Compliance as a function of Crack Length (Material 3, h = 2.62 mm) $C_o = L^3/(4E_1wh^3)$.

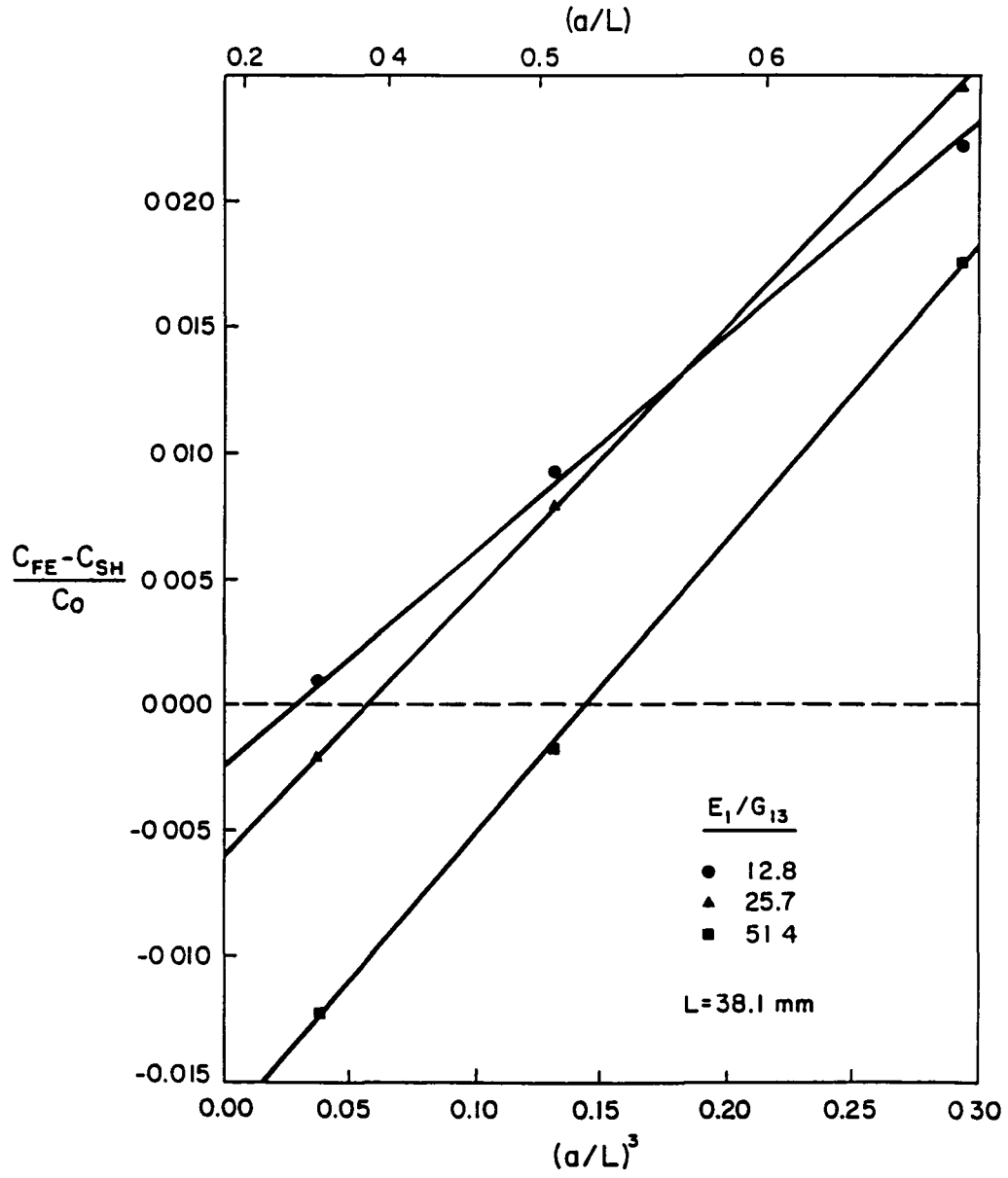

Fig. 25 ENF Compliance as a function of Crack Length (Material 3, h = 2.62 mm) $C_o = L^3/(4E_1wh^3)$.

Finally, strain energy release rate calculations are further substantiated by exhibiting good agreement with results presented by Barrett and Foschi who evaluated Mode II stress-intensity factors for cracked wood beams [24]. The stress intensity factors in their analysis of the ENF geometry were determined by the finite element method, using singular, orthotropic, isoparametric elements which incorporated the exact displacement field in the region surrounding the crack tip. Strain energy release rates were calculated from the stress intensity by the following relationship:

$$G_{II} = K_{II}^2 \frac{1}{\sqrt{2}\, E_1} \left[\left(\frac{E_1}{E_3}\right)^{1/2} + \left(\frac{E_1}{2G_{13}} - \nu_{13}\right) \right]^{1/2} \qquad (22)$$

The correlation of results are presented in Table 20 for ENF geometries exhibiting similar span/thickness ratios.

Table 20 Correlation of Strain Energy Release Rates (G_{II}^{FE}) with the Results of Barrett and Foshi (G_{II}^{SI}) (h=2.62 mm, L=38.1 mm, Material 3)

a/L	E_1/G_{13}	G_{II}^{FE}/G_{II}^{BT}	G_{II}^{SI}/G_{II}^{BT}
0.33	12.8	1.32	1.26
0.33	25.7	1.58	1.62
0.33	51.4	2.03	2.18
0.50	12.8	1.34	1.19
0.50	25.7	1.55	1.54
0.50	51.7	1.93	2.07
0.67	12.8	1.37	1.16
o.67	25.7	1.56	1.50
0.67	51.4	1.87	2.01

4. INTERLAMINAR FRACTURE TEST RESULTS

One of the objectives in this investigation is to evaluate mixed-mode fracture criteria for the prediction of delamination growth in the ITWD test specimen geometry. Two graphite fiber composite materials (APC-2 and CYCOM 982) having significantly different fracture toughnesses are included in the experimental effort to provide additional insight into instability related delamination growth as a function of G_{IC} and G_{IIC}. The validity of any mixed-mode fracture criterion, however, is strongly dependent on the accuracy of indepedent critical strain energy release rate measurements. Consequently, a detailed experimental study characterizing the Mode I and Mode II fracture toughness is conducted in conjunction with preliminary testing of the ITWD test specimen geometry (see Section 4.4).

Initial testing was conducted at room temperature and at a cross-head rate of 1.25 mm/min (0.05 in/min) for both the DCB and ENF fracture tests. The original intent of the DCB testing was to straightforwardly characterize G_{IC} at initiation and during propagation using the compliance and area method data reduction schemes summarized in Appendix 1. The ENF test matrix was designed to investigate the influence of span and laminate thickness on G_{IIC} to complement the analysis presented in Chapter 3 in additon to the basic materials characterization. Furthermore, the sensitivity of G_{IIC} on precracking technique (Mode I, Mode II or none) is also

investigated. This is an important issue to resolve since self-consistent precracking of the ITWD specimen is desired. Test results are discussed in subsequent sections and summarized in Appendix 7.

Initial testing, however, revealed fundamental differences in the fracture behavior between the thermoset and thermoplastic unidirectional graphite fiber composite materials. In general, the CYCOM 982 thermoset material exhibits linear load-deflection response and data reduction schemes based upon linear elastic fracture mechanics are appropriate for both the Mode I and Mode II tests. The APC-2 thermoplastic, however, exhibits significant non-linear behavior, particulariy evident for the Mode II loading. In Figure 26, a characteristic load-deflection response is presented for an ENF test of the APC-2 material. The degree of non-linearity is quantified in subsequent discussions by the strain energy release rates based upon the initial compliance and the load at the onset of non-linearity (G_{ISC} or G_{IISC}) and the initial compliance and the maximum load (G_{IC} or G_{IIC}), respectively, as defined in Figure 26.

In Figure 27, the test fixture utilized for ENF testing is presented. A travelling microscope is employed to monitor the crack tip during the test. Unstable crack growth is observed for both the thermoset and thermoplastic materials (a/L=0.5). The APC-2 material, however, exhibits subcritical crack growth prior to the unstable growth to the center load pin. The response is shown

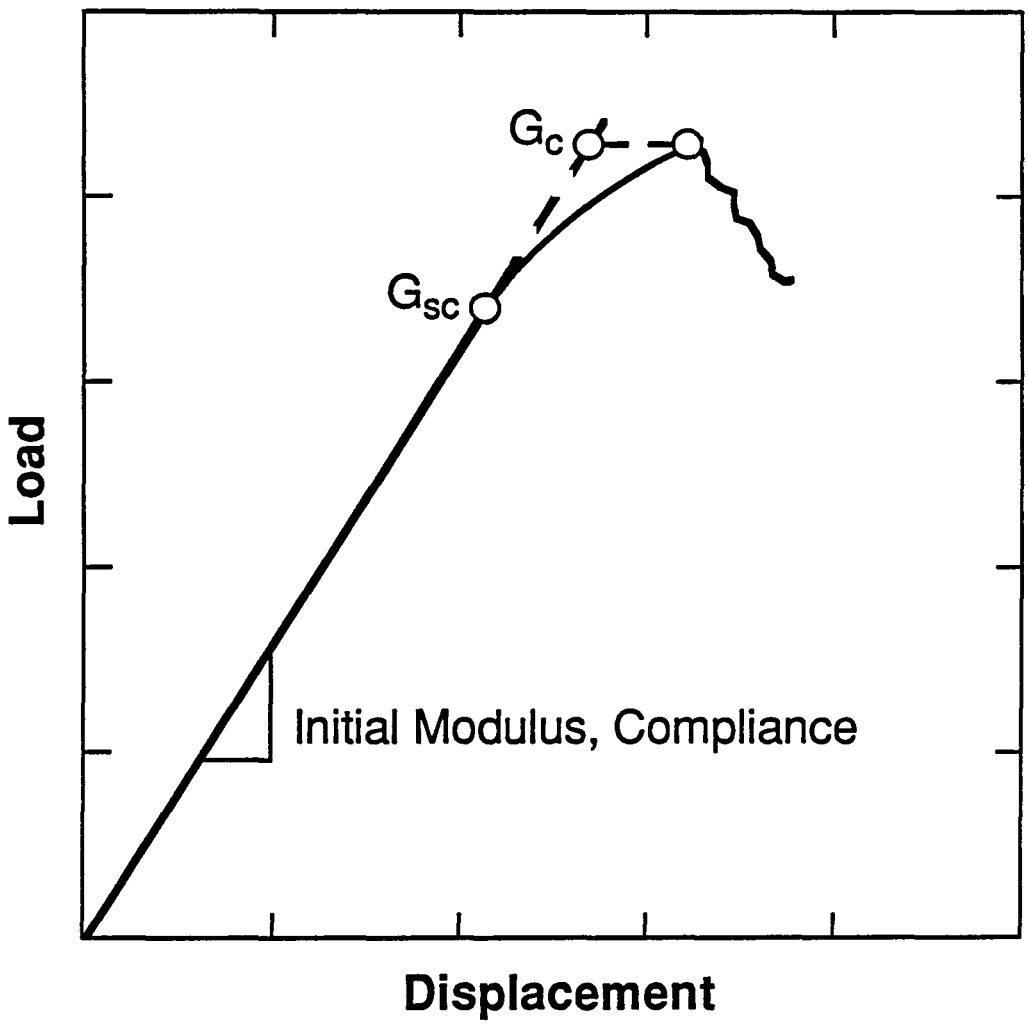

Figure 26. Strain energy release rate definitions to characterize non-linear behavior.

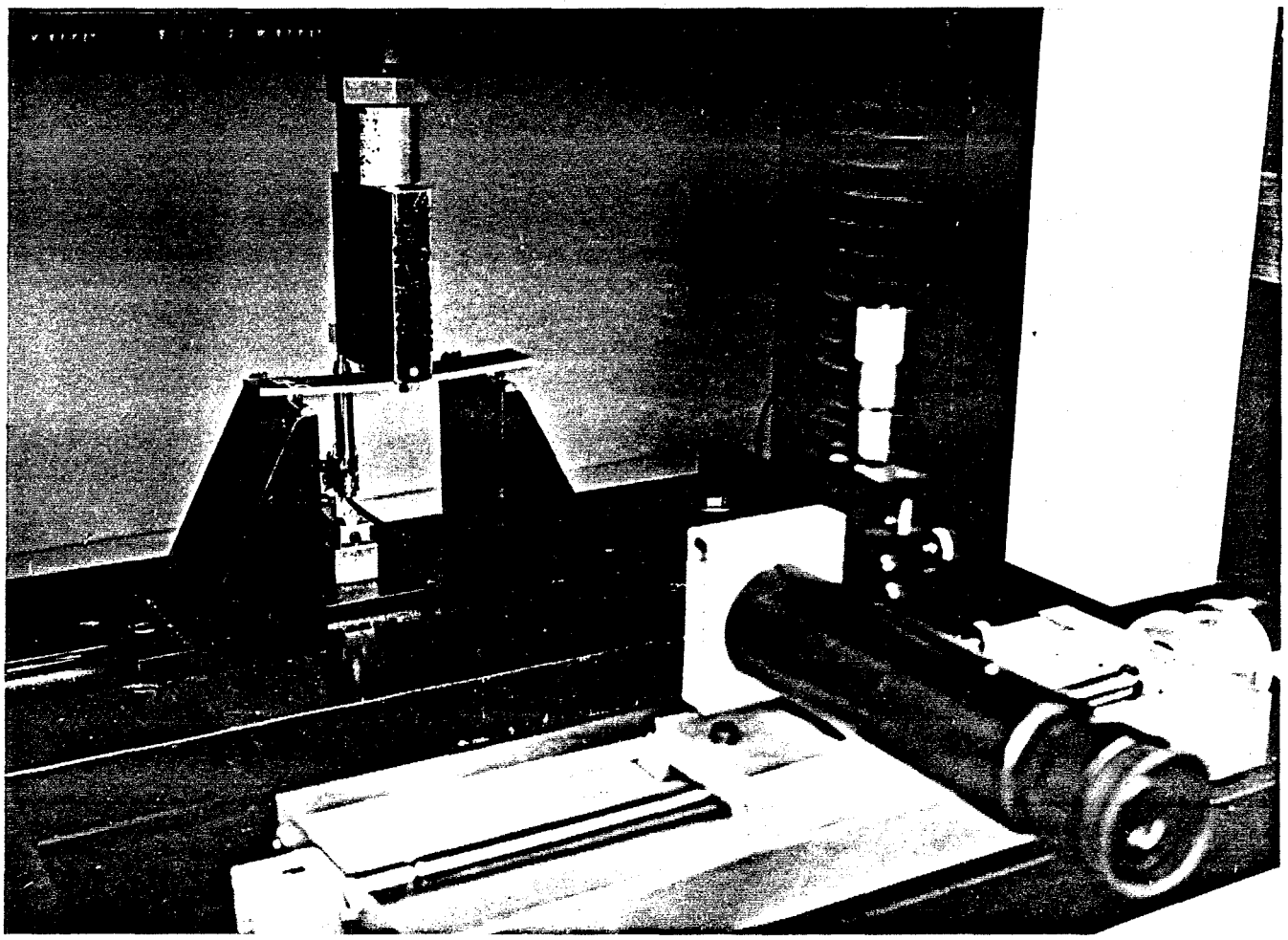

Fig. 27 ENF Test Fixture

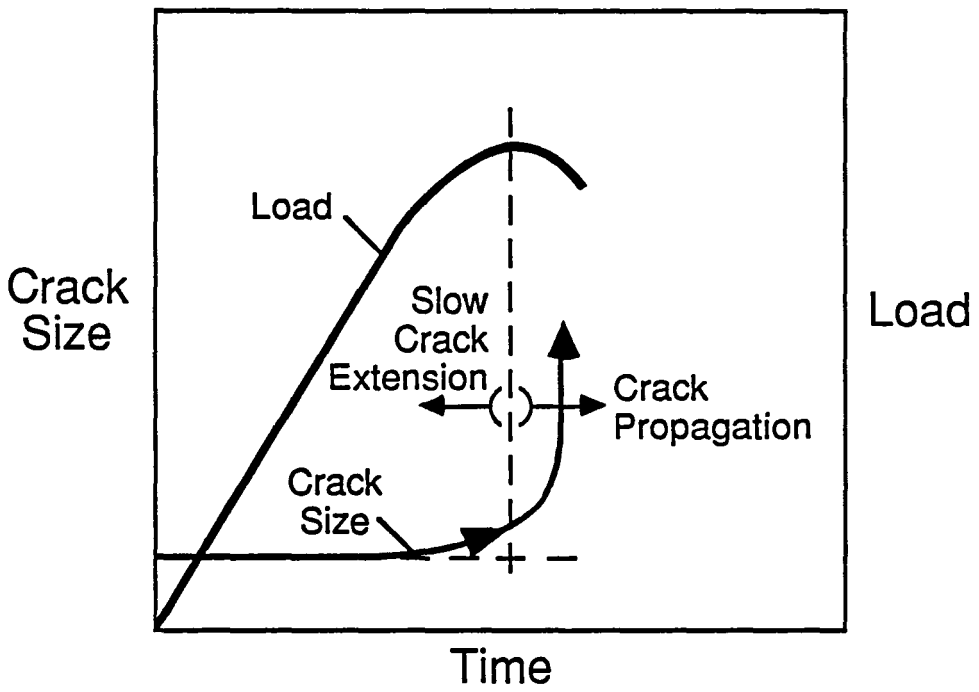

Fig. 28 Influence of Subcritical Crack Growth on Load

schematically in Figure 28. The onset of non-linearity in load-displacement response corresponds approximately with the onset of subcritical crack growth as detected with the travelling microscope. This observation does not eliminate the possibilty that matrix yielding and viscoelastic effect may contribute significantly to the non-linear response observed experimentally. In all probability, crack extension in a ductile resin such as PEEK may be preceeded by the development of a process zone, constrained by the elastic fibers, where extensive deformation and microcracking may occur [25]. The subcritical crack growth may therefore correspond to the coalescence of microcracks within the process zone prior to unstable crack growth.

4.1 DCB Test Results

The minimum number of plies required to maintain linear reponse for the largest crack length tested is based on the analysis presented in Appendix 3 and summarized in Figure 7. Measured G_{IC} values confirm that $[0]_{26}$ APC-2 and $[0]_{24}$ CYCOM 982 provide adequate thickness to minimize errors induced by geometric non-linearites. Hinges are employed for load introduction into the delaminated beams for both materials. Hinges were adhesively bonded to the CYCOM 982 specimens and crack lengths were measured from the center of the hinge pivot pin. Due to an initial weak bonding of the hinges to the APC-2 specimens, hinges were fastened with small screws. Crack lengths in this situation were measured

from the center of the screw. Subsequently, hinges were sucessfully bonded to the APC-2 samples. Test results showed no change in G_{IC} values due to different hinge fastening or crack length definitions. Furthermore, crack length definitions were consistent with compliance versus crack length measurements.

The compliance and area method data reduction schemes summarized in Appendix 1 are employed in the present investigation. In Figure 29, typical load-deflection curves for a CYCOM 982 DCB specimen is presented. Linear elastic response is observed and stable, slow growth initiates at the highest load level for all rates tested. Further imposed deflection yields additonal stable crack growth and a monotonic decrease in load. From the loading and unloading curves, the compliance versus crack length and critical load versus crack length is obtained as shown in Figure 30 (see Appendix 7). The compliance method yields an initiation energy of $G_{IC} = 0.25 \pm 0.02$ kJ/m^2. The area method yields a slightly greater propagation interlaminar fracture tougness of $G_{IC} = 0.26 \pm 0.02$ kJ/m^2.

In contrast to the stable crack growth observed in the epoxy specimens, the Mode I crack growth in the APC-2 was often unstable. This 'stick-slip' phenomenon has been documented previously by other researchers [26]. In Figure 31, typical load-deflection curves for a cross-head speed of 25mm/min are presented to illustrate the variety of crack growth mechanisms observed during

the Mode I testing of APC-2. In general, stable, unstable and subcritical crack growth are possible as shown in Figure 31. Rate effects to be further discussed in Section 4.3, indicates that stable growth is achievable as crosshead speeds diminish. As shown in Figure 32, linear elastic, stable crack growth is realized for a crosshead speed of 0.5 mm/min.

The area method was employed to characterize the average fracture energy consumed during unstable and stable delamination growth, respectively. An average value of G_{IC} = 1.50 ± 0.20 kJ/m^2 was measured for the unstable crack growth mechanism in APC-2. Stable crack growth data analyzed using the area method yielded a significantly higher toughness of G_{IC} = 2.00 ± 0.10 kJ/m^2. The G_{IC} value for stable growth of APC-2 (V_f = 0.62) is in good agreement with earlier published results as shown in Figure 33, where G_{IC} is found
to diminish with increasing fiber volume fraction. The initiation energy based on the compliance method and maximum load yields G_{IC} = 1.75 ± 0.13 kJ/m^2, an intermediate value falling between the two area method measurements. The DCB test results discussed in this section are summarized in Table 21.

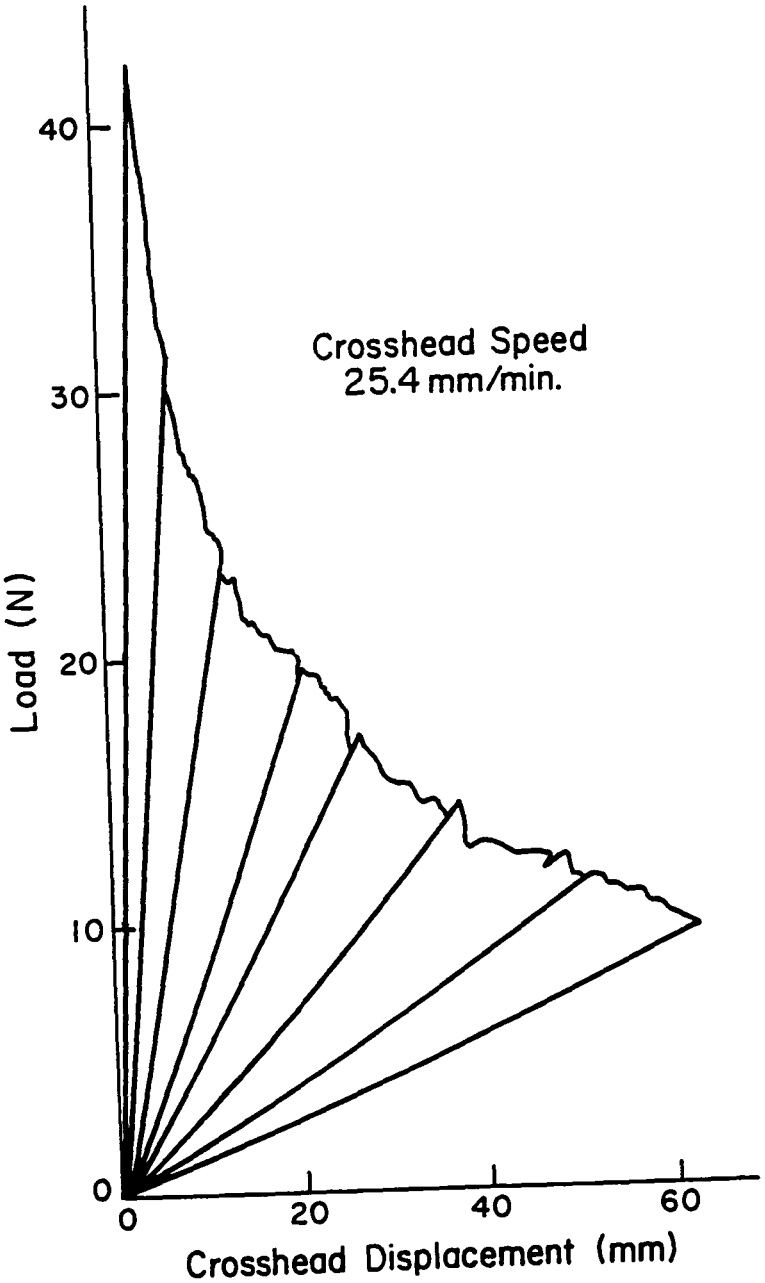

Fig. 29 Typical Load vs. Displacement Curves for CYCOM 982 DCB Test.

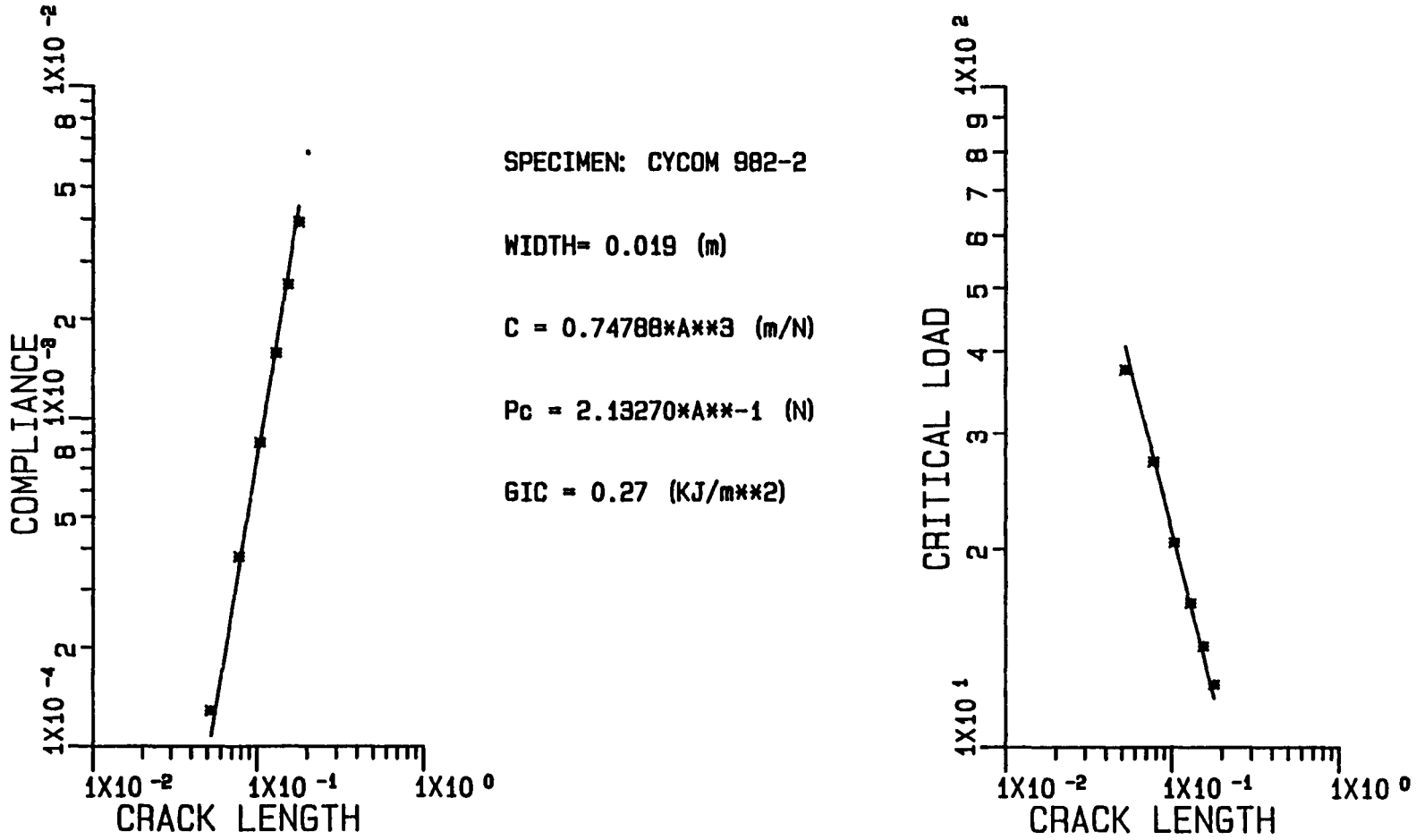

Fig. 30 Typical Compliance vs Crack Length and Critical Load vs. Crack Length for DCB Testing of CYCOM 982.

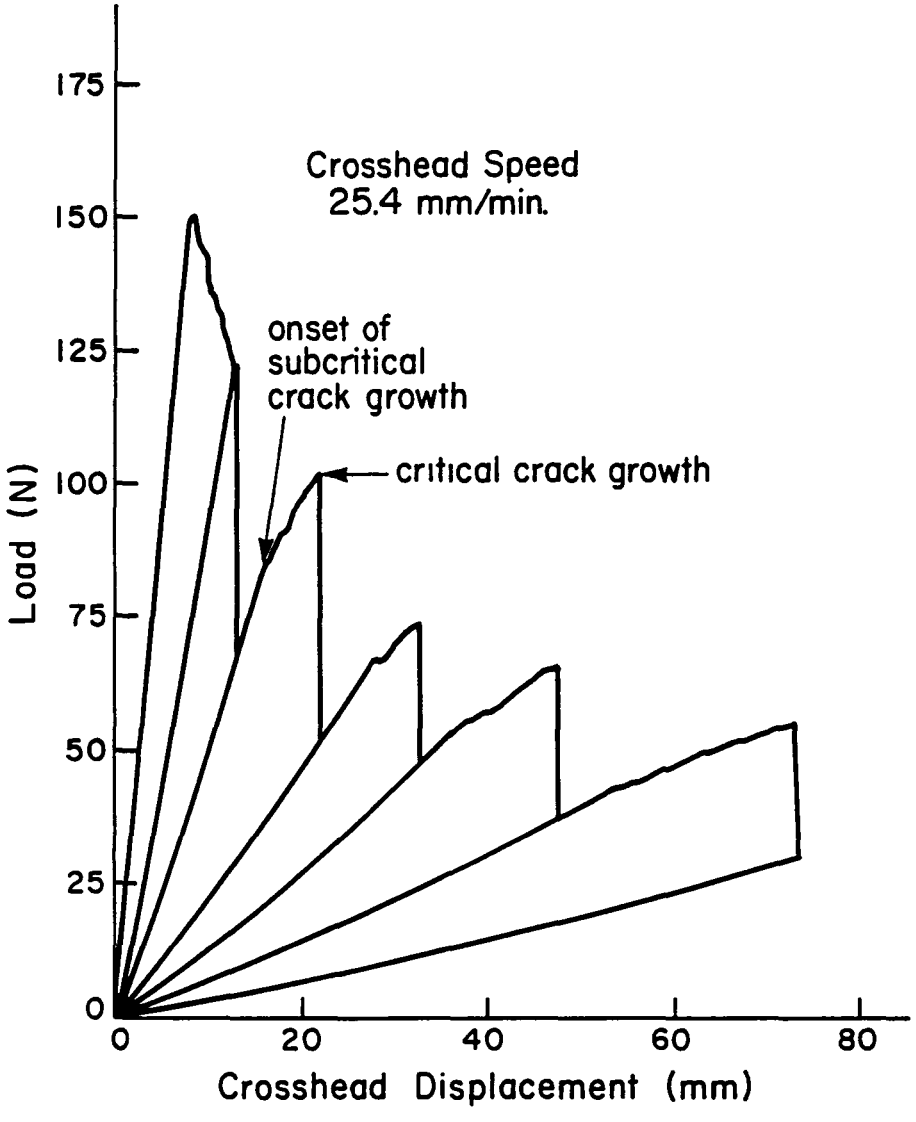

Fig. 31 Load vs. Displacement Curves For APC-2 DCB Test (Crosshead speed = 25mm/min).

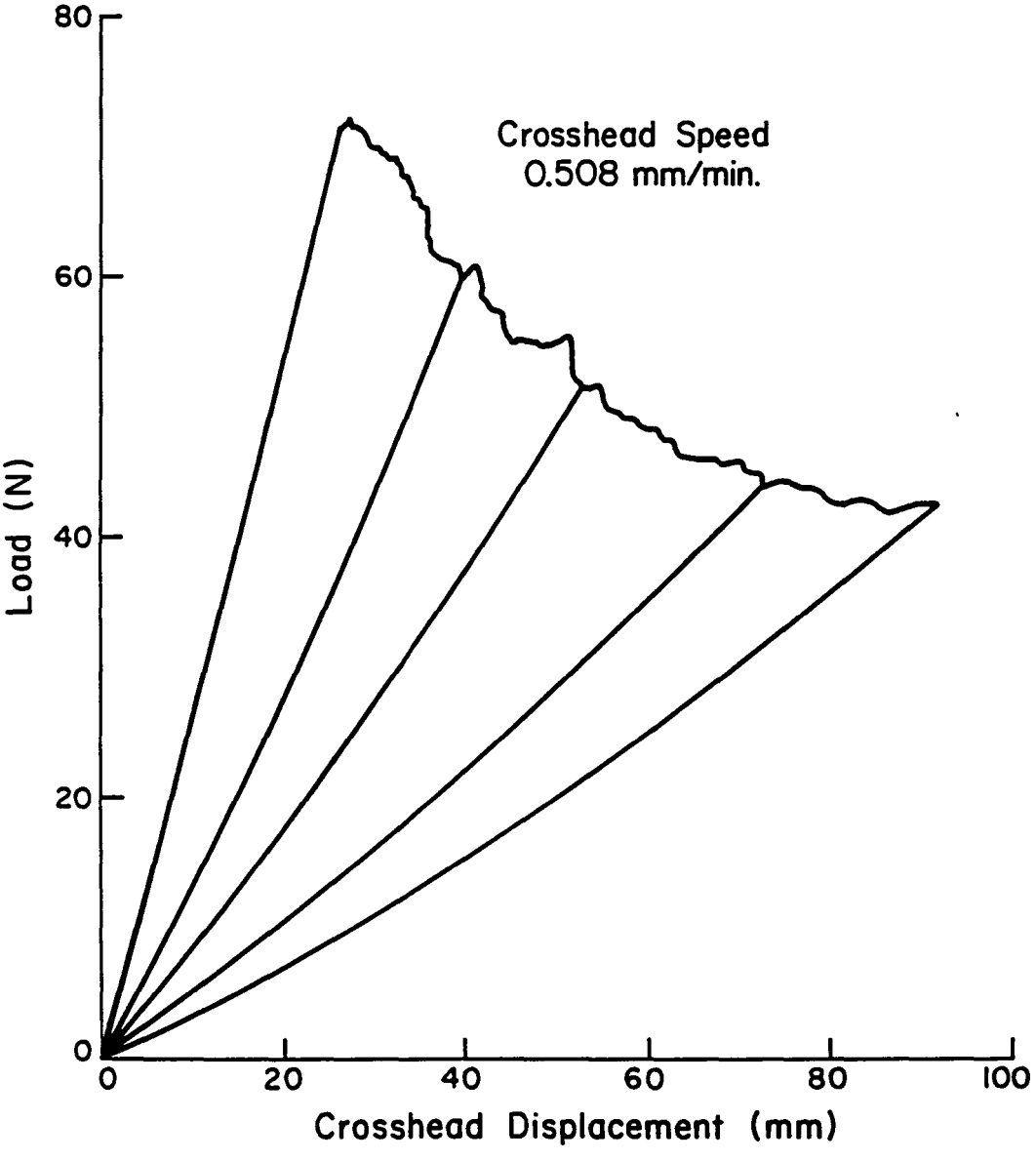

Fig. 32 Load vs Displacement Curves for APC-2 DCB Test (Crosshead speed = 0.5mm/min).

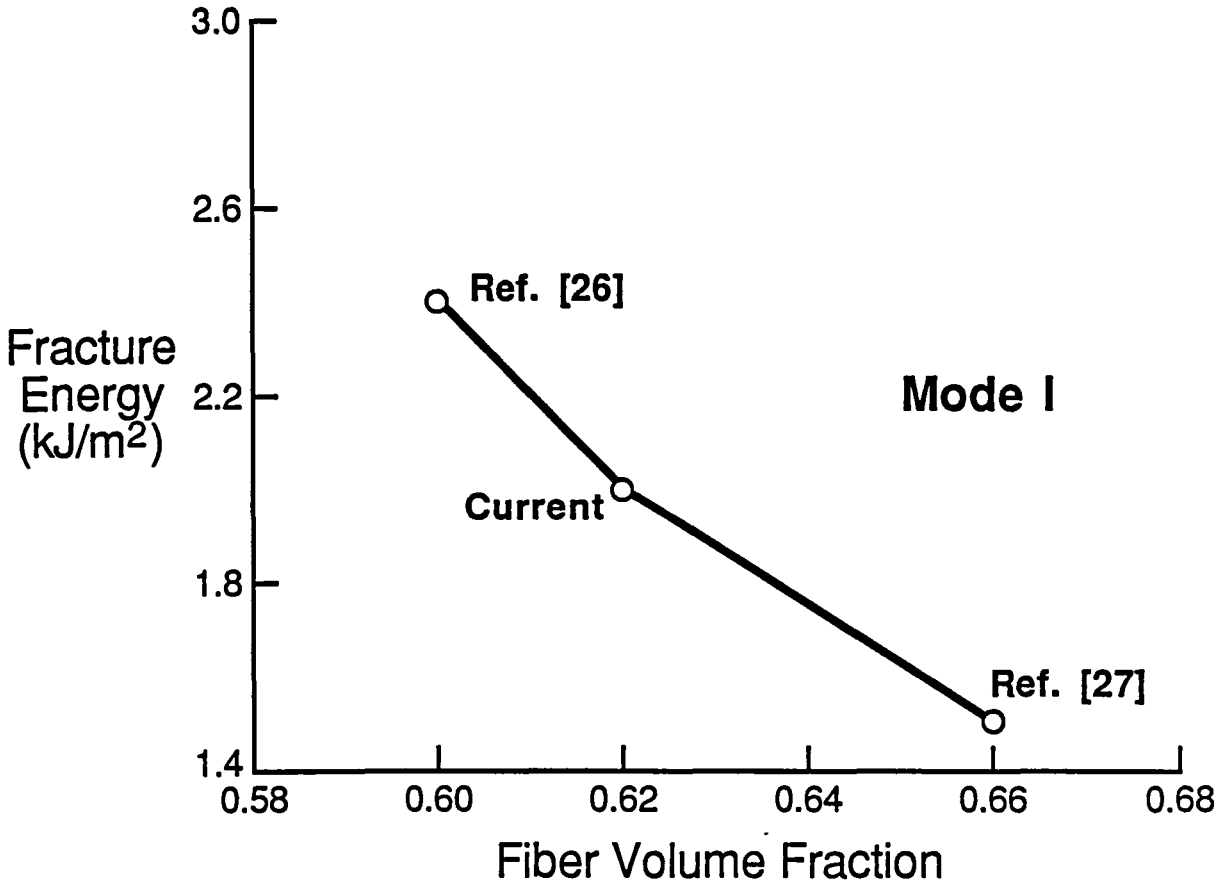

Figure 33. Mode I fracture toughness versus fiber volume fraction for APC-2.

Table 21. DCB Test Results: G_{IC} (kJ/m^2)

Material	Compliance Method*	Area Method	
		Stable	Unstable
APC-2	1.75 ± 0.13	2.00 ± 0.09	1.50 ± 0.20
CYCOM 982	0.25 ± 0.02	0.26 ± 0.02	NONE

*Averaged results based on maximum load.

Instron rate: 1.25 to 2.5 mm/min (0.05 to 0.10 in/min)

4.2 ENF Test Results

In this section the influence of precracking on the Mode II fracture toughness will be discussed. Furthermore, finite element based data reduction will be illustrated on the CYCOM 982 material which essentially behaves in a linear elastic manner.

Three techniques of precracking were studied. The first technique, illustrated in Figure 34, was to wedge the crack surfaces open with a razor to propagate the crack away from the Kapton insert film. The crack was allowed to propagate a distance of about 5 mm until it was arrested at the clamp, see Figure 34. In this way a Mode I precrack was achieved which produces a distinct

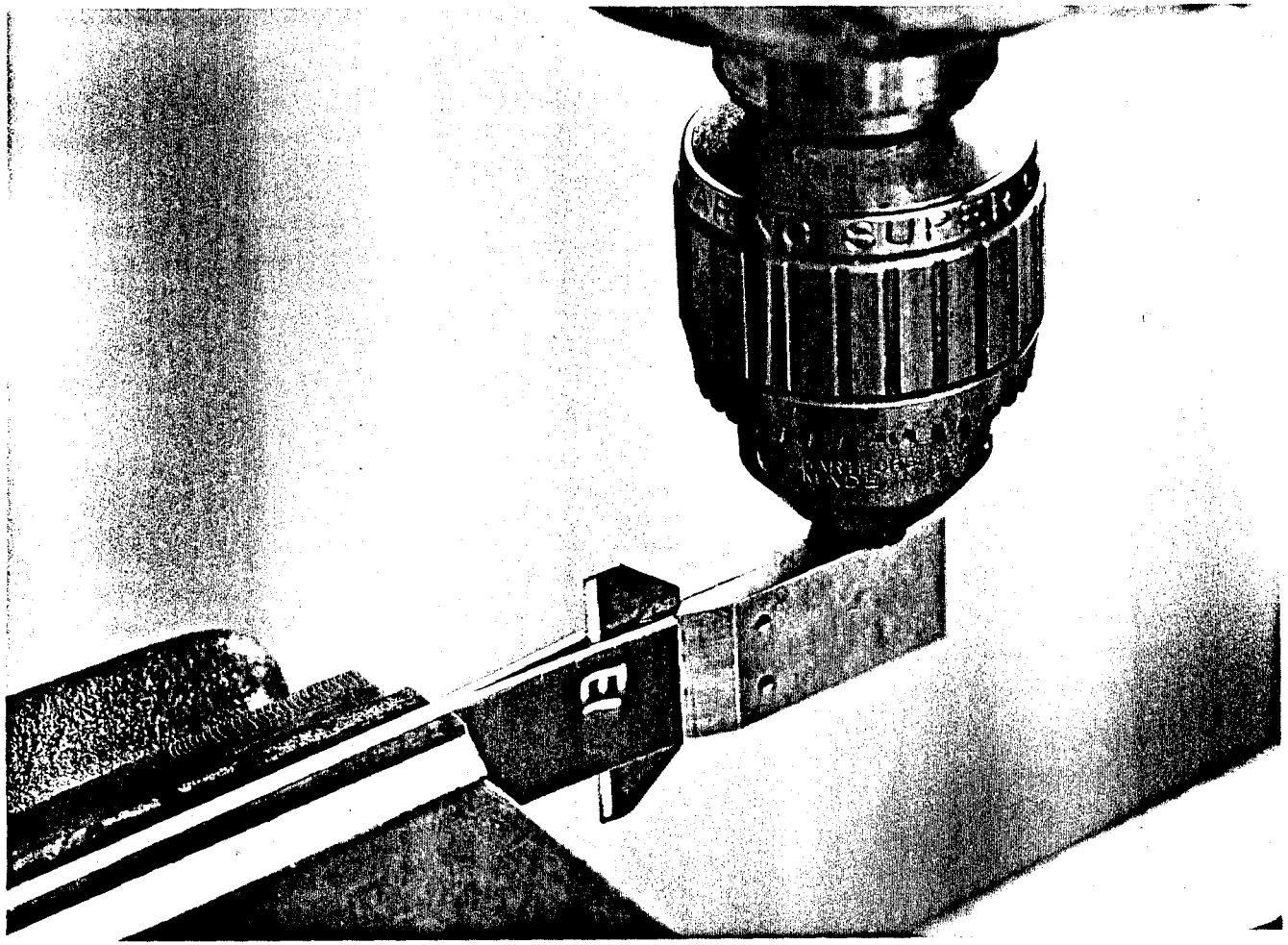

Figure 34. Mode I precraking for an ENF specimen.

mark on the fracture surface at the Mode II initiation line.

The second way of introducing a precrack was to load the specimen in the TPB fixture. Based upon the stability analysis presented in Appendix 2, a/L > 0.7 was chosen to propagate the crack slowly in a stable manner to the center load pin. This produced a Mode II precrack. By carefully wedging the crack open the crack tip was marked on both sides with a fine pencil. The third technique was to use the Kapton insert as a starter crack (no precrack).

Table 22 shows the results in terms of G_{IISC} and G_{IIC} defined in Figure 26. It is observed that the CYCOM 982 material behaves essentially in a linear elastic manner reflected in the closeness of the G_{IISC} and G_{IIC} values. Furthermore, compared to the Mode I precracking, the Mode II precracking results in larger fracture toughness values and brings G_{IISC} and G_{IIC} closer. However, the most striking effect is the high toughness values for the case where no precracking was used. This effect is evidently a result of the blunted crack tip at the end of the Kapton insert film (two plies of nominal thickness 0.025 mm).

For the APC-2 material significant nonlinear behavior was observed manifested in the large difference in the G_{IISC} and G_{IIC} values presented in Table 22. The Mode I precracking produced consistent G_{IIC} values at different thicknesses and spans. The Mode II precracking resulted in a higher G_{IIC} value and decreased the

percentage difference between G_{IISC} and G_{IIC}. As for the CYCOM 982 material, however, the largest G_{IIC} value was obtained for the no precrack situation.

Table 22 Mode II test results. Influence of precracking. Five replicates. a/L=0.5. Displacement rate is 1.25 mm/min (0.05 in/min.). Data reduction is based on simple beam theory.

Material/No. of Plies	Precrack	Half Span, L mm	G_{IISC} kJ/m^2	G_{IIC} kJ/m^2
CYCOM 982/24	Mode I	51	0.61±0.04	0.68±0.02
CYCOM 982/24	Mode II	51	0.75±0.07	0.77±0.07
CYCOM 982/24	"	38	0.65±0.09	0.68±0.11
CYCOM 982/24	No precrack	51	--	1.45±0.16
CYCOM 982/24	"	38	--	1.40±0.18
APC-2/26	Mode I	51	1.37±0.20	1.78±0.11
APC-2/40	"	51	--	1.87±0.11
APC-2/26	"	38	--	1.89±0.16
APC-2/40	"	38	--	1.84±0.07
APC-2/26	Mode II	51	1.63±0.28	1.93±0.28
APC-2/26	No precrack	51	1.84±0.07	2.73±0.33

The nonlinearities observed before unstable crack growth appear to be due to inelastic material behavior (viscoelastic or plastic yield), in the vicinity of crack tip combined with some amount of stable crack growth, here denoted by subcritical crack growth as detected with the travelling microscope. Crack propagation in a ductile resin has been found to be preceeded by the development of a process zone, constrained by the rigid, elastic fibers, where extensive deformation and microcracking may occur [25]. The subcritical crack growth may therefore correspond to the coalescence of microcracks within the process zone prior to unstable crack growth. In the context of this mechanism, the Mode I precracking appears to produce an initially sharper crack leading to larger amount of subcritical crack growth before unstable Mode II crack growth initiates. The Mode II precracking, on the other hand, creates a precrack which is more conditioned for shear loading resulting in less amount of subcritical crack growth or inelastic material behavior prior to unstable growth evidenced by the relative closeness of G_{IISC} and G_{IIC} for this situation. For the no precrack situation the blunted precrack amplifies the extent of inelastic material behavior in the vicinity of the crack tip and increases the apparent fracture toughness.

To illustrate the finite element (FE) based data reduction scheme for the ENF specimen discussed in Chapter 3, the CYCOM 982 data in Table 22, which essentially fullfill the linear elastic assumptions made in the finite element analysis, were employed. In particular the data for a/L=0.5 at two different half spans L=38 mm and 51 mm, respectively, for Mode II precracks were used to obtain a consistent comparison of the results. Table 23 shows that the FE based data reduction scheme results in more consistent values of the fracture toughness in Mode II.

Table 23 Finite element based data reduction for CYCOM 982 ENF specimens with Mode II precracks. See Tables 15 and 17 for material 3 (E_1/G_{13} = 25.7)

Half Span mm	G_{IIC}^{BT} kJ/m^2	G_{IIC}^{FE} kJ/m^2
51	0.77±0.07	0.98±0.09
38	0.68±0.11	0.94±0.15

4.3 Rate Effects in Mode I and II Fracture

In this section the influence of rate on the Mode I and II fracture behavior is examined over a range of Instron crosshead rates for the APC-2 material. The following crosshead rates were used ; 0.25, 2.5, 25 and 250 mm/min (0.01, 0.10, 1.00 and 10.0 in/min).

Typical load-displacement curves for the DCB test (Mode I) are shown in Figure 35. At low rates the response may be characterized as linear elastic-stable while at higher rates a deviation from linearity is noted at some point before critical crack growth occurs. The knee point in the load-displacement record appears to be related to subcritical crack growth as discussed in Section 4.2 for the Mode II testing. A significant difference, however, between Mode I and II loading is that in Mode II the subcritical crack growth is associated with some degree of inelastic material behavior, while the deviation from linearity in the Mode I case almost entirely is related to subcritical crack growth with negligible inelastic material behavior observed, see Figure 31 for more detail. At low rates the critical crack growth (crack growth that leads to a load drop) is stable but becomes unstable, "stick-slip", at higher rates. The "stick-slip" phenomenon apparently reflects strain rate effects occuring in the process zone. Before further discussing the rate effects the load-displacement behavior for Mode II loading will be outlined. Figure 36 shows typical load-displacement curves for the APC-2 ENF

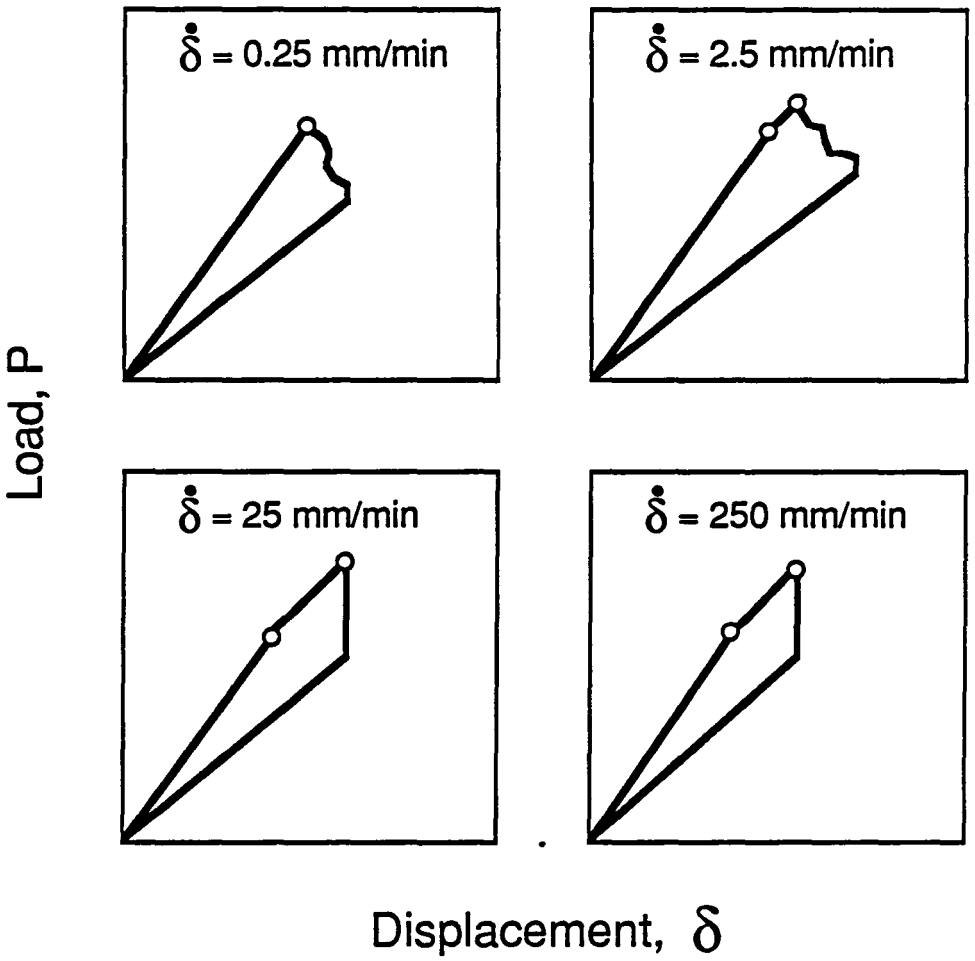

Figure 35. Typical load-displacement response for APC-2 DCB specimen at various crosshead rates.

tests at various displacement rates. At low rates significant nonlinear response was observed before the initiation of unstable crack growth. As mentioned earlier in this section, the nonlinearities are attributed to subcritical crack growth in combination with crack front inelastic material behavior. The tracing of the subcritical crack growth prior to the onset of rapid fracture, based on surface measurements by the travelling microscope is not entirely satisfactory due to the possibility of tunneling which may obscure the true tip of the crack [28] and the possible influence of edge effects. However, qualitatively, the subcritical crack growth observed here appears to be similar to what has been observed in metals [28], namely, a slow stable crack growth sometimes associated with small "pop-ins" in the load-displacement record. At higher displacement rates, the load-displacement response becomes more linear and at the highest rate tested (250 mm/min) negligible nonlinearities are observed, see Figure 36.

Apparently the nonlinear response in both Mode I and II is higly rate dependent indicating that the development of the process zone and the subcritical crack growth are viscoelastic in nature. To gain further insight into the rate dependency it is useful to discuss rate effects more locally, i.e. in the crack tip region. For the DCB specimen, Smiley [29] derived the following expression for the rate of crack opening displacement, $\dot{\delta}_{CT}$, at any instant preceeding crack propagation,

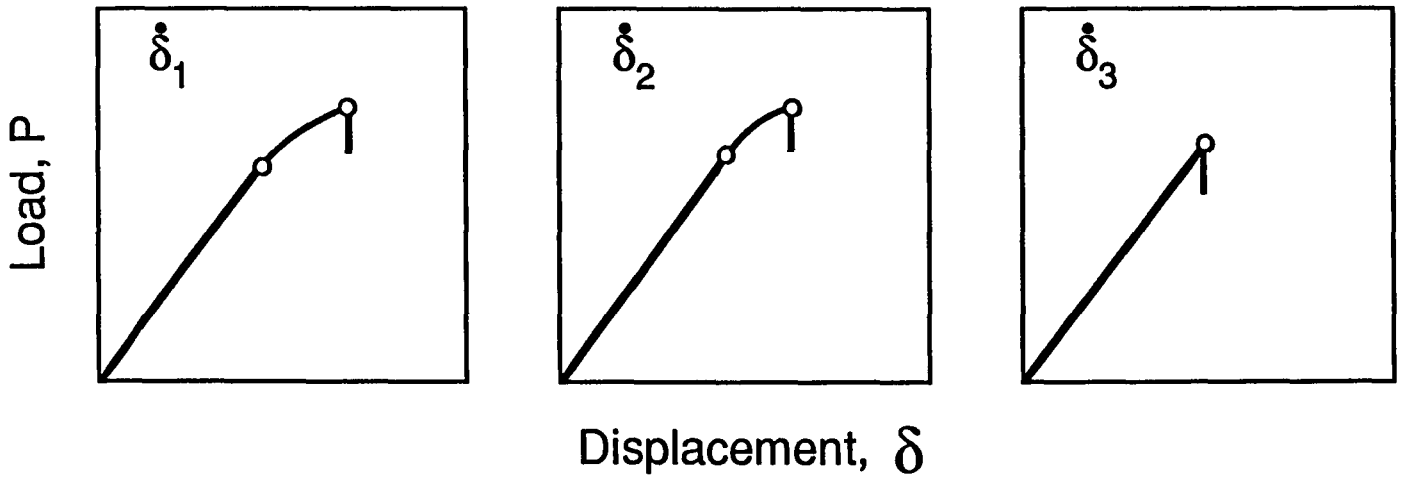

Figure 36. Load displacement response for APC-2 ENF specimen at various crosshead rates, $\dot{\delta}$. $\dot{\delta}_1 < \dot{\delta}_2 < \dot{\delta}_3$. The range in $\dot{\delta}$ is from 0.25 to 250 mm/min.

$$\dot{\delta}_{CT} = 1.5\dot{\delta}\xi^2 \qquad (23)$$

where $\dot{\delta}$ is the displacement rate at the point of load introduction and ξ is a nondimensional distance, x/a, measured from the crack tip ($x/a << 1$).

Prior to the onset of crack propagation, at the crack tip, $\xi = 0$ and $\dot{\delta}_{CT} = 0$. Therefore, the crack tip velocity is defined at an arbitrarily small distance, in this case about two ply thicknesses (x=0.25 mm), away from the crack tip. Defining a local displacement rate is particularly important in quantifying rate effects in the DCB specimen where the crack tip velocity diminishes with the square of crack length, see equation (23).

For the Mode II specimen the corresponding expression for the relative sliding rate, $\dot{u}_{CT}$, at a distance ξ from the crack tip is,

$$\dot{u}_{CT} = \frac{24\, ha^2\, \dot{\delta}}{(2L^3 + 3a^3)}\,\xi \qquad (24)$$

Ten DCB specimens (72 crack lengths) and 20 ENF specimens (20 crack lengths) were included in the experimental study of rate effects in Mode I and II fracture. The response was studied over four decades of Instron rates, viz. 0.25, 2.5, 25 and 250 mm/min.

Average results for the DCB and ENF specimens are summarized in Tables 24 and 25, respectively. In Mode I the toughness for onset of subcritical crack growth, G_{ISC}, decreases somewhat with increased displacement rate while the toughness for critical crack growth, G_{IC}, peaks at an intermediate displacement rate. For the Mode II situation, Table 25, G_{IISC} is relatively constant up to the highest rate where an increase is noted. To relate the rate effects to local crack tip behavior the crack tip velocities for the DCB and ENF specimens were calculated from equations (23) and (24), respectively.

Table 24 Rate dependency of APC-2 Mode I fracture toughness. Data reduction is based on beam theory, $G_{Ix} = 3A_1P_x^2a^2/2w$ where x = SC and C respectively (Fig. 31) and A_1 is an initial compliance coefficient defined in Appendix 1.

Displacement Rate mm/min	$\dot{\delta}_{CT}$ m/s x 10^{10}	G_{ISC} kJ/m^2	G_{IC} kJ/m^2
0.25	0.02-1.6	1.56±0.05	1.56±0.05
2.5	1-10	1.60±0.26	1.75±0.13
25	8-118	1.41±0.21	1.98±0.13
250	108-1102	1.37±0.15	1.71±0.16

Table 25 Rate dependency of APC-2 Mode II fracture toughness. Data reduction is based on beam theory (initial compliance) and load at onset of nonlinearity, P_{SC}, and load at critical crack growth, P_C (Fig. 26).

Displacement Rate mm/min	$\dot{\delta}_{CT}$ m/s x 10^9	G_{IISC} kJ/m^2	G_{IIC} kJ/m^2
0.25	2.86	0.95±0.18	1.84±0.27
2.5	28.6	1.01±0.09	1.82±0.20
25	286	0.98±0.16	1.40±0.13
250	2860	1.40±0.13	1.40±0.13

Figure 37 shows the toughness values plotted versus crack tip displacement rate. It is observed that G_{IC} goes through a maximum and G_{ISC} goes through a slight minimum as the crack tip opening rate increases. G_{IIC} and G_{IISC}, on the other hand, remain fairly constant at all crack tip velocities up to the highest velocity where G_{IIC} decreases and G_{IISC} increases. At the highest rate the response in both Mode I and II loading is approximately linear elastic resulting in,

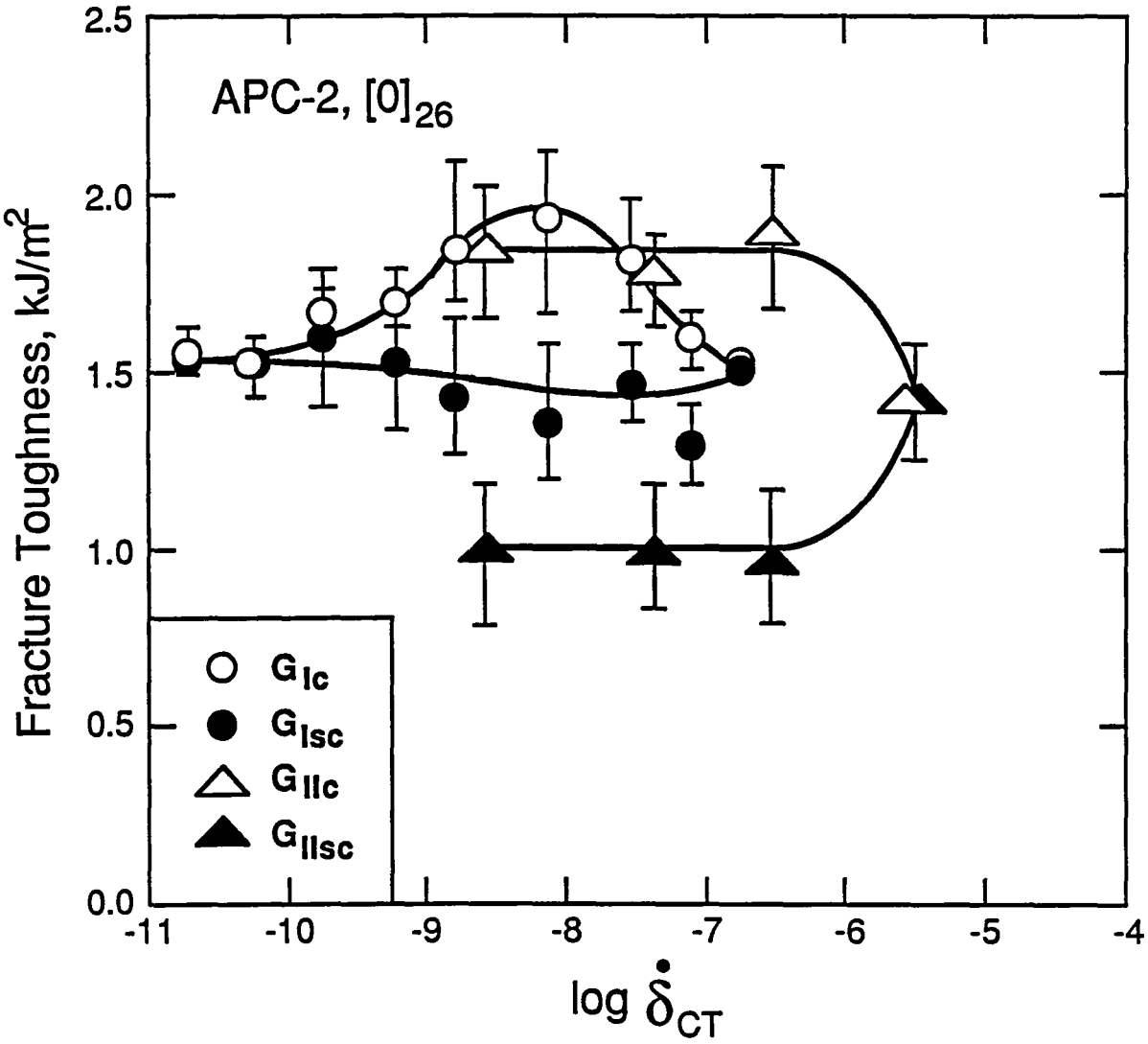

Figure 37. Rate dependence of Mode I and II fracture toughness.

$$G_{ISC} = G_{IC} \quad (25)$$

$$G_{IISC} = G_{IIC}$$

To further illustrate the rate dependency of toughness the difference between the toughnesses for critical crack growth and subcritical crack growth in Mode I and II, respectively, was calculated,

$$\Delta G_{IC} = G_{IC} - G_{ISC} \quad (26)$$

$$\Delta G_{IIC} = G_{IIC} - G_{IISC} \quad (27)$$

Figure 38 shows that ΔG_{IC} peaks at an intermediate crack tip velocity that is achieved at a displacement rate of about 25 mm/min. At the highest crack tip velocities negligible subcritical crack growth is observed as reflected in the small ΔG_{IC} values. For Mode II loading ΔG_{IIC} decreases slowly initially and drops to a small magnitude at the highest rate tested.

Discussion

The rate effects on interlaminar fracture of APC-2 observed

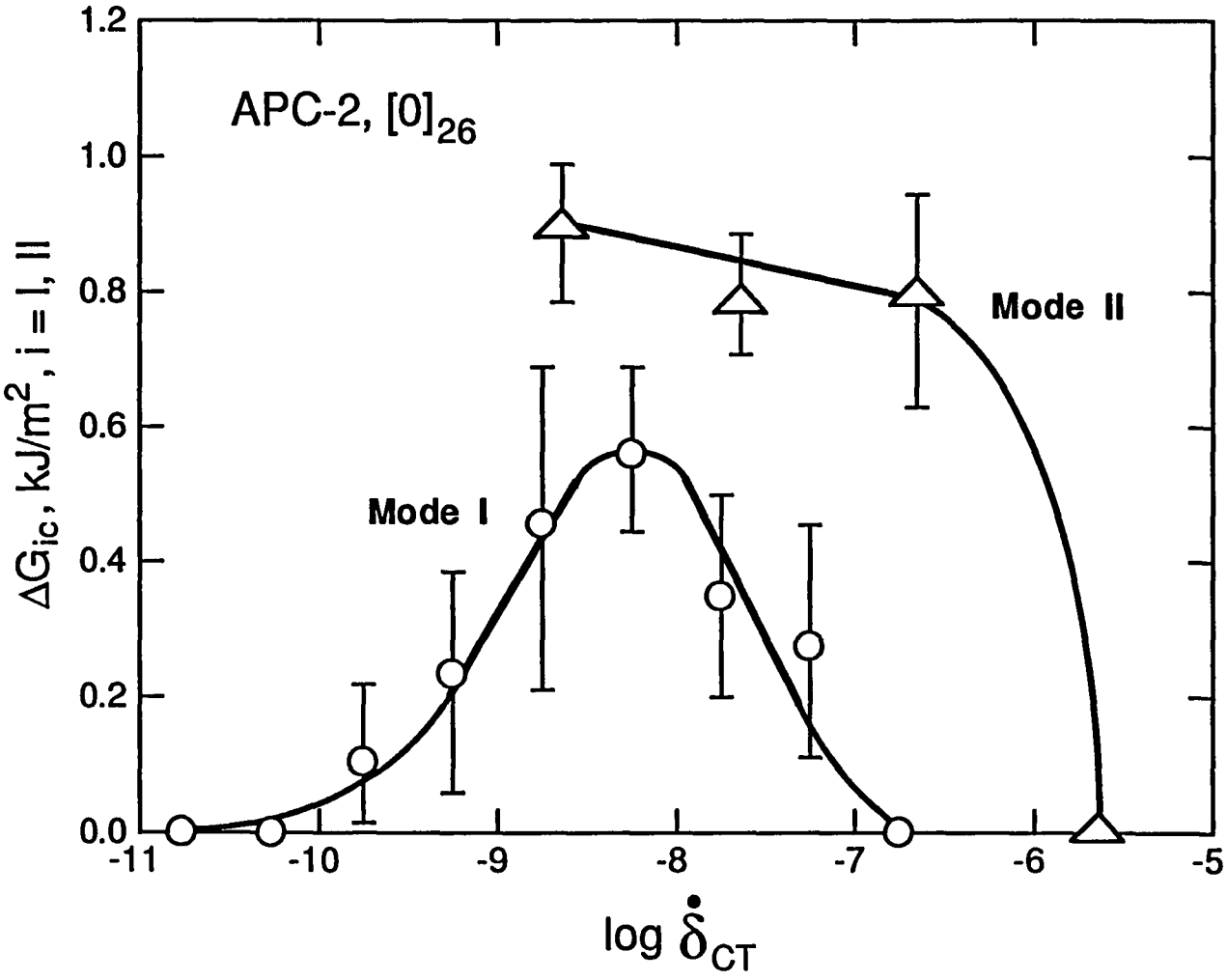

Figure 38. ΔG_{IC} and ΔG_{IIC} versus crack tip velocity for APC-2.

herein appear to be viscoelastic in nature. Based on insitu scanning electron microscopic examination of the fracture process, it has been found that a significant process zone develops around the crack tip [25]. The process zone is assumed, in the present discussion, to contain all inelastic behavior such as matrix plasticity, viscoelasticity and microcracking as well as fiber debonding. The discussion of rate effects is based on the following premises:

On a micromechanics level, the plastic zone surrounding the crack tip will develop instantaneouesly relative to the loading rate when the yield stress in the matrix is exceeded. The plastic zone will continue to grow with increased load until an equilibrium geometry of the zone is established. In this situation, the size of the plastic zone will be determined by the yield stress of the matrix in conjunction with the stress redistribution to adjacent elastic fibers. The constraint imposed by the fibers will clearly diminish the plastic zone size relative to the neat polymer response [25]. Furthermore, the yield stress for most glassy polymers increases in direct proportion to the logarithm of strain rate [30]. It is therefore anticipated that the size of the plastic zone in the vicinity of the crack tip will be inversely proportional to the crack tip displacement rate.

The second premise in the discussion addresses the influence of rate on the material response within the process zone external to the plastic zone where viscoelastic effects may dominate. At low rates, viscoelastic effects will be prevalent yielding an upper

bound on the size of the process zone. At the highest rates, viscoelastic effects will be negligible and the process zone will tend to be coincident with the developing plastic zone. Intermediate rates will yield intermediate process zone sizes.

In Figure 38, the influence of rate on the degree of nonlinearity in the load displacement response is quantified for the APC-2 material by ΔG_{IC} and ΔG_{IIC} defined in equations (26) and (27) for Mode I and Mode II loading, respectively. In Mode II loading the polymer in the process zone is subjected to an intense shear stress. Polymers are known to be more viscoelastic and to yield more easily in pure shear than in dilatation (Mode I) [30]. The degree of nonlinearity in the load-displacement response is significantly greater than for the Mode I situation evidenced by $\Delta G_{IIC} > \Delta G_{IC}$ as shown in Figure 38. This indicates that the process zone in the ENF specimen is significantly larger than in the DCB specimen.

At the lowest rates tested, linear elastic load deflection response and stable crack growth is observed in Mode I where $\Delta G_{IC} = 0$, see Figure 38. In this situation, the yield stress exhibit a minimum value which corresponds to maximum plastic zone and process zone sizes. It is hypothesized that the stable crack growth corresponds to a slow drawing of the polymer and the coalescence of microcracks within the process zone. More

importantly, however, the loading rate is sufficiently low so that the crack growth rate and the process zone growth rate are the same order of magnitude.

Crack growth occuring entirely within the evolving process zone is the mechanism associated with subcritical crack growth. The above scenario is analogous to the Crack Layer Theory [31,32] where this type of behavior is observed in metals and polymers. It is interesting to note that on a macroscopic level, linear elastic load-displacement response is observed for a rate where viscoelastic and plastic response dominate crack growth.

As crack tip displacement rates increase, however, the Mode I fracture toughness, G_{IC}, increases prior to attaining a maximum value while G_{ISC} is relatively rate independent. The increase in G_{IC} is attribated qualitatively to an increase in the matrix yield stress within the plastic zone. Similar trends in the fracture toughness of neat polymers have been reported [30]. It has also been observed that the "stick-slip" phenomen and subcritical crack growth occurs over this range of displacement rate in Mode I loading. It is hypothesized that the subcritical crack growth rate is greater than the growth of the evolving process zone. When the crack is contained within the process zone, stable growth occurs as noted for the lowest rates tested. When the crack grows to the boundary of the evolving process zone, unstable growth occurs. Since the size of the process zone diminishes with increased rate, it is anticipated that an increasing amount of unstable crack

growth occurs as rates increase. This is substantiated by trends exhibited by experimental data presented herein.

Further increase in displacement rate results in a ductile/brittle transition and a reduction in G_{IC} as shown in Figures 37 and 38. The transition is evident from the inspection of the SEM fracture surfaces shown in Figures 39 and 40, where plastic deformation of the matrix normal to the plane of crack growth is significantly reduced.

With respect to the Mode II loading, similar mechanisms as discussed for the Mode I situation are proposed to explain the influence of rate on fracture toughness. Significant nonlinearity in the load-displacement curves is observed for all but the highest rate tested. This response is shown schematically in Figure 36 and quantified by ΔG_{IIC} in Figure 38. The nonlinearity is attributed to inelastic material response and subcritical crack growth within the process zone.

In contrast to the Mode I loading, ΔG_{IIC} does not tend to zero for the lowest rate tested, see Figure 38. Although the lowest rate tested for the ENF specimen results in a crack tip velocity that is two decades higher than the corresponding rate for the DCB specimen, it is not anticipated that ΔG_{IIC} will tend to zero with diminishing rate for the following reasons: Multiple crack lengths are routinely tested in the DCB test. After the first crack growth

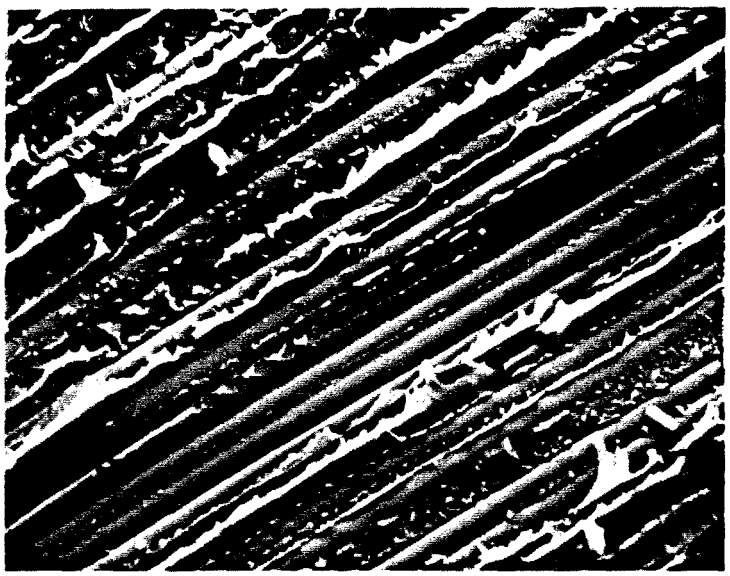

640 X

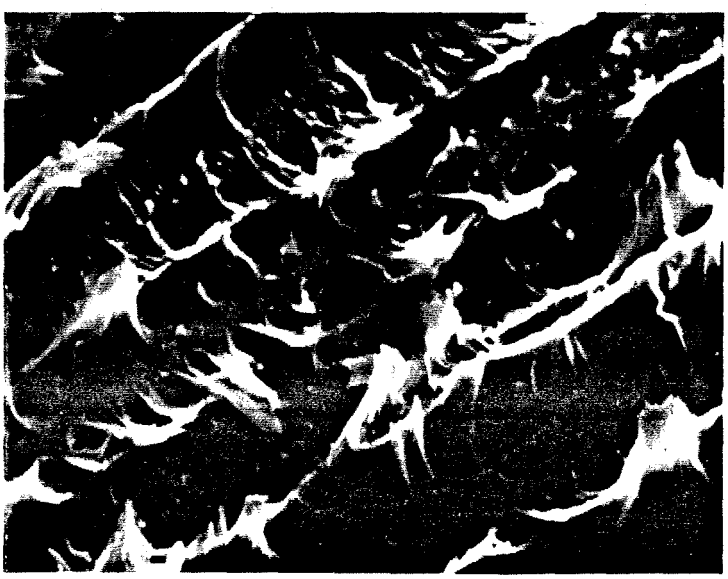

2500 X

Figure 39. Mode I fracture surface of APC-2 loaded at a low displacement rate showing ductile behavior.

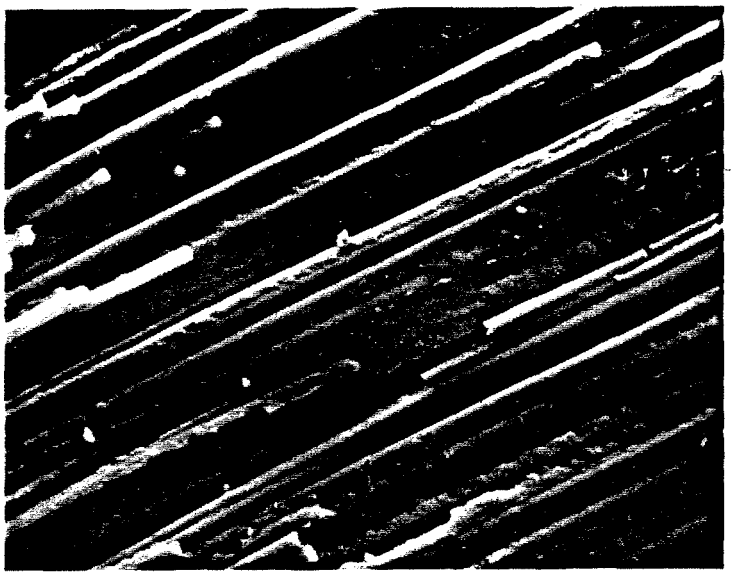

640 X

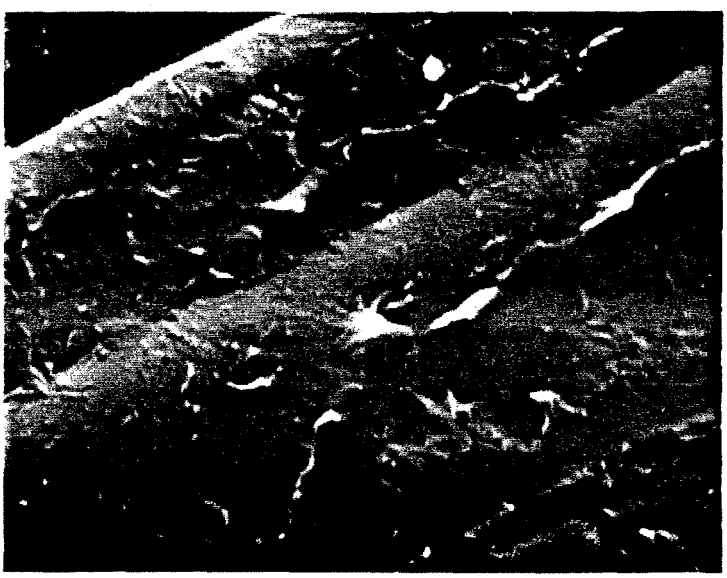

2500 X

Figure 40. Mode I fracture surface of APC-2 loaded at a high displacement rate showing brittle behavior.

increment the process zone, if fully developed, would not significantly contribute to a nonlinear load deflection response in subsequent loading cycles. In the Mode II test, only a single crack length is tested. The onset of nonlinearity is therefore associated with the development of the process zone. As stated previously, the size of the process zone will tend to increase with diminishing rate. The process zone in the Mode II situation will also be significantly larger than in the Mode I case since inelastic effects are more pronounced in shear. Furthermore, crack lengths are 2-6 times smaller than those in the DCB fracture specimen. A larger process zone in conjunction with shorter crack lengths will certainly contribute to the macroscopic nonlinearity in the load-deflection response observed. Based on the above discussion, one might expect ΔG_{IIC} to increase prior to reaching a plateau value with diminishing rate. This trend is observed experimentally as shown in Figure 38.

The second reason which precludes the possibility of ΔG_{IIC} tending to zero with decreasing crack tip displacement rate is the fundamental difference between the DCB and ENF fracture tests. Under fixed grip conditions, the Mode II specimen yields unstable crack growth (see Appendix 2) while the Mode I specimen is inherently stable. The mechanism of subcritical crack growth due to coalescence of microcracks within the process zone also occurs and contributes to the nonlinear load-deflection response. Since the strain energy release rate increases with crack length, subcritical

crack growth initiating in the developing process zone will be accelerated as shown schematically in Figure 28. In contrast to the DCB response at low rates, the growth of the process zone will not match the subcritical crack growth rate. Consequently, the crack will growth towards the boundary of the process zone resulting in unstable crack growth.

At the highest rate tested, linear elastic behavior is observed and a reduction in G_{IIC} corresponds to a ductile/brittle transition in the fracture process. The transition is evident from the inspection of the fracture surfaces of the APC-2 material shown in Figures 41 and 42. A significant reduction in plastic deformation associated with the formation of hackles, characteristic of the shear loading, is noted.

4.4 ITWD Test Results

Fabrication of the ITWD specimen is accomplished by implanting 2 layers 0.025 mm thick Kapton film betwen plies at various depths. 64 plies was chosen as the laminate thickness in order to study a wide range of delamination depths. Furthermore, a thick laminate minimizes global bending of the 100 mm test section.

Experience gained during compression testing reported in Section 2.2 clearly demonstrated that the IITRI compression fixture would not be suitable for the 64 ply ITWD specimen since end tab shear failures would occur for the high loads required to propagate

2500 X

Figure 41. Mode II fracture surface of APC-2 loaded at a low displacement rate showing ductile behavior.

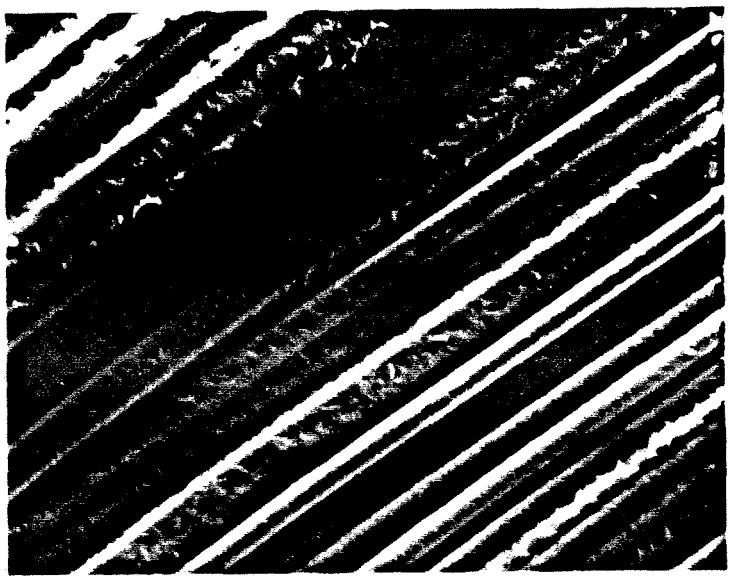

640 X

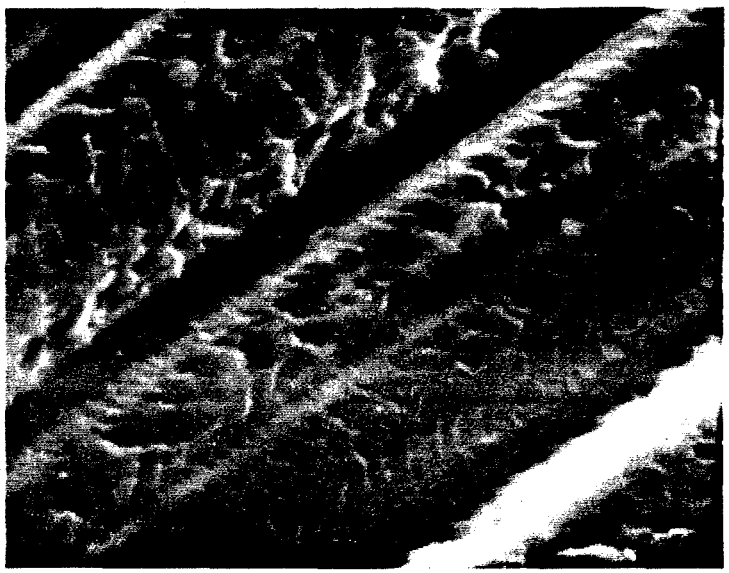

2500 X

Figure 42. Mode II fracture surface of APC-2 loaded at a high displacement rate showing brittle behavior.

the delamination. A new fixture was designed which successfully end loads the specimen without initiating damage to the load introduction surfaces, see Figure 43. This is achieved by clamping the specimen over a 38 mm distance from either end. To assess the uniformity in load introduction, strain gages were mounted on all four sides of a no defect sample at the center of the gage section. Minimal strain gradients were observed indicating a uniform loading of the specimen.

Cylindrical clamps were developed, see Figures 43 and 44, to arrest the potentially unstable crack growth at specified lines before the delamination propagates to the end of the test section. In this manner, precracking to obtain a natural crack tip is achieved. Precracking is essential because the resin pockets created at the ends of the implanted delamination would significantly increase the apparent fracture toughness. This effect was verified through testing of ENF specimens that where not precracked, see Section 4.2. Clamping just beyond the crack front may also provide a means to test one specimen with multiple crack lengths. Additional testing and analysis of the influence of the clamped crack arrest is in progress. Figure 44 shows a specimen with a delamination of an initial length of 38 mm arrested with clamps at 54 mm. Compressive loading of the specimen shown in Figure 44 maintains the post-buckled shape of the delaminated region. Close examination of Figure 44 also reveals the presence of global bending due to the reduction in stiffness of the buckled sublaminate.

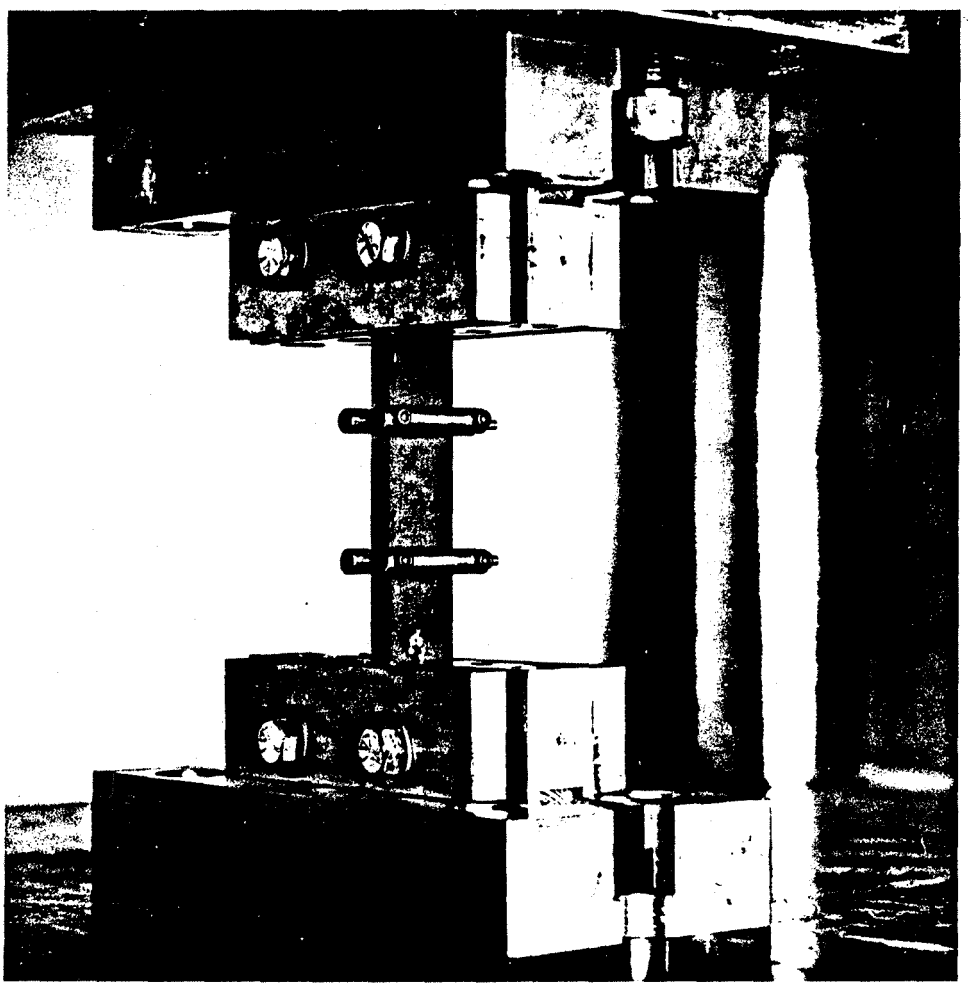

Figure 43. End loading compression fixture.

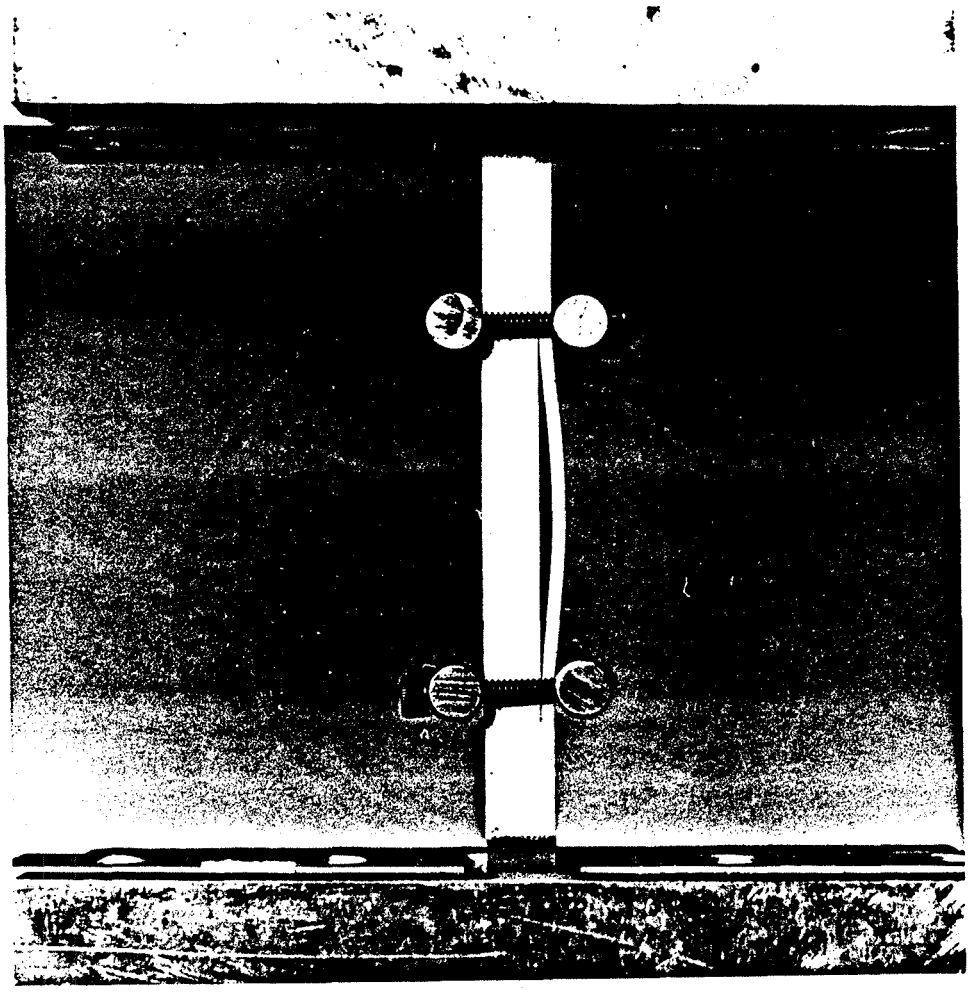

Figure 44. 64 ply ITWD specimen with postbuckled subleminate (at 110 KN load.)

The compresive strengths and failure modes of 64 ply laminates without implanted delaminations have been investigated. Preliminary tests of $[0]_{64}$ APC-2 and CYCOM 982 specimens indicate compressive strengths of about 900 and 650 MPa, respectively. The basic mechanical properties characterization showed that $[0]_{16}$ APC-2 and CYCOM 982 specimens have compressive strengths of 1250 and 1300 MPa respectively, for the brooming failure mode. The difference appears to be related to a change in the mode of failure in compression.

Shear type of failures through the width of the $[0]_{64}$ CYCOM 982 may be responsible for the loss 50% in compressive strength. However, the shear mode of failure of $[0]_{64}$ APC-2 laminates decreased the strength by only 28%. Figure 45 shows a through the width shear type of failure of a CYCOM 982 specimen after buckling of the 38 mm long, 12 plies thick, delaminated region.

Consequently, the reduction in compressive strain to failure must be incorporated into the sizing of the ITWD specimen. Based upon the superposition analysis of Whitcomb [13], delamination lengths and depths will be chosen in conjunction with the appropriate fracture toughness values to quarantee crack growth at desired G_I/G_{II} ratios prior to compressive failure. In this manner, the ITWD test specimen geometry can be employed to assess the validity of various mixed-mode failure criteria for the onset of delamination growth.

Preliminary results have been obtained for the out-of-plane

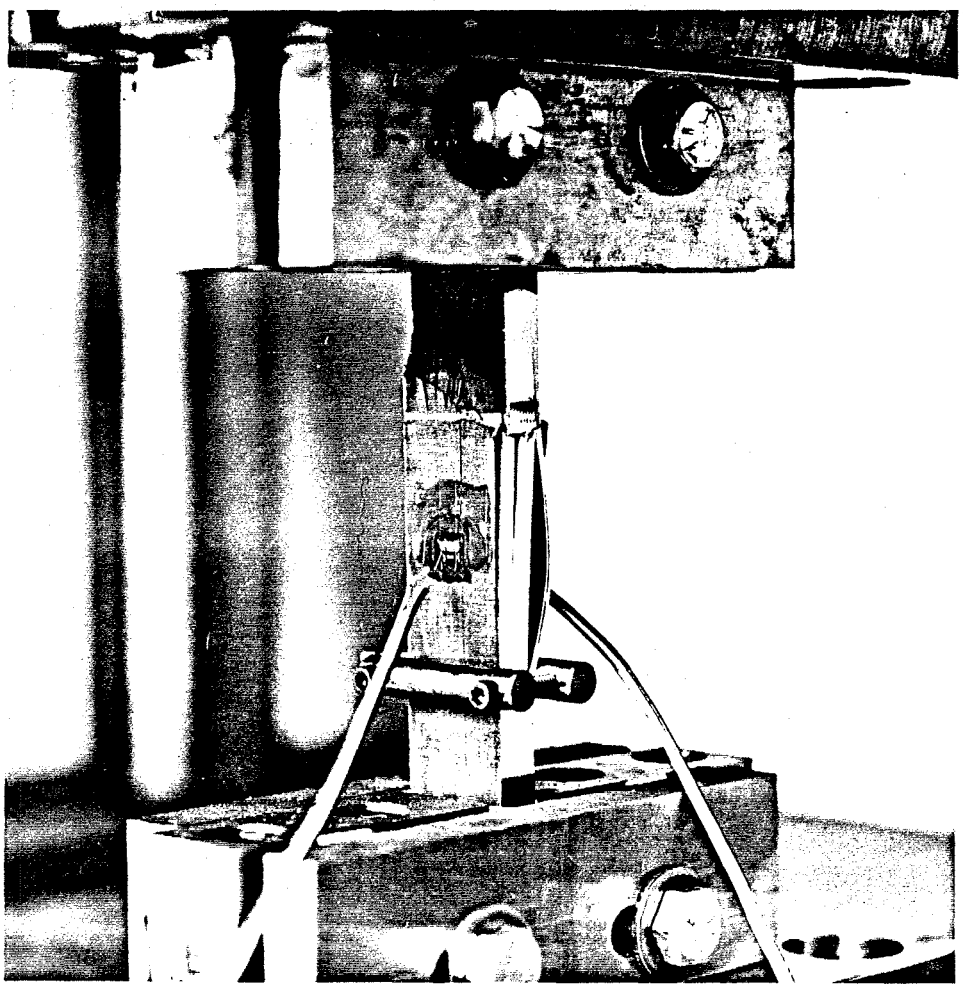

Figure 45. Shear type failure in an ITWD specimen.

displacement of the delaminated region. When the load is removed after precracking a finite out-of-plane displacement of the delaminated region remains. Upon reloading, the out-of-plane deformation increases monotonically from zero load as expected. Figure 46 shows measured and predicted out-of-plane deformation for an ITWD specimen with an initial displacement of the delaminated region. The predictions by Whitcomb [13], Ashizawa [4] and Gillespie [1] underestimate the out-of-plane deformation in the upper region of the loading curve. This discrepancy may possibly be caused by global bending of the test section. An analytical prediction for the out-of-plane deformation as a function of the applied load, including global bending, is underway for this program. Nonlinear finite element results will also be compared to the analytical and experimental data.

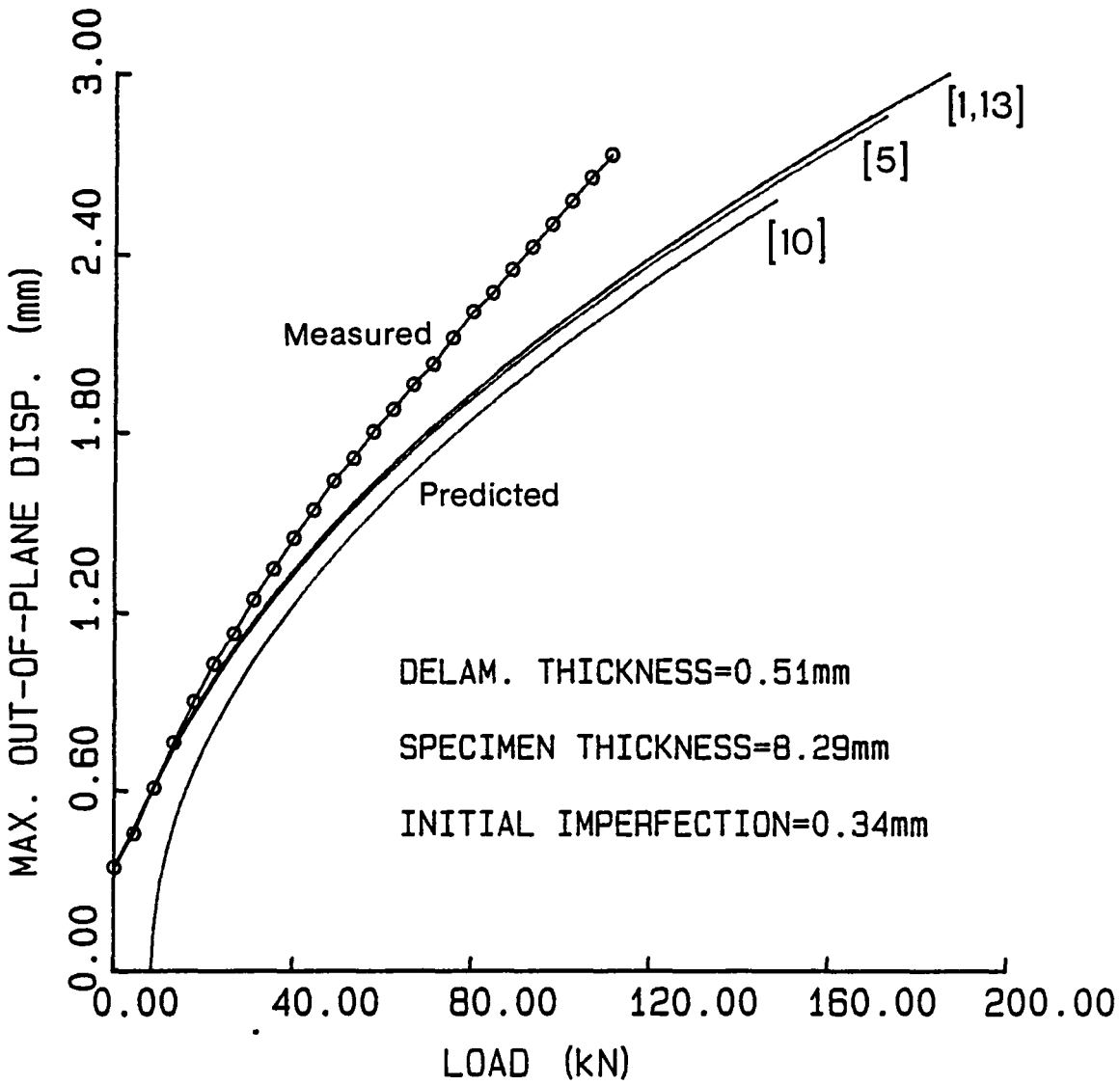

Figure 46. Comparison of measured and predicted out-of-plane displacement as a function of the applied load. (APC-2, Delamination length = 54.1 mm)

5. CONCLUSIONS

Based on the results presented in this report the following conclusions may be drawn:

- Processing techniques developed for thermoplastic graphite/PEEK composites appear to produce high quality laminates.

- Sizing of fracture specimens is important in order to achieve crack growth prior to geometric nonlinearities or material failure.

- Interlaminar shear deformation may have to be considered for certain ENF specimen geometries.

- Friction between the crack surfaces can be minimized through suitable design of the ENF specimen based on beam theory analysis.

- For ENF geometries commonly in use friction reduces G_{II} by 2 to 4 percent.

- Finite element analysis confirms that the ENF specimen is a pure Mode II test.

- Finite element analysis of the ENF specimen reveals that beam theory underestimates G_{II} by 20 to 40 percent depending on the crack length to span ratio.

- ENF specimen insensitive to delamination offset from laminate midsurface.

- Data reduction scheme for ENF specimen may have to rely on a combination of beam theory and finite elements.

- Precracking essential for the ENF specimen.

- Nonlinear response observed for the DCB and ENF specimen is attributed to subcritical crack growth and/or inelastic material behavior.

- Nonlinear effects are highly rate dependent.

- Stick-slip behavior in Mode I testing of APC-2 is a rate effect.

- Preliminary ITWD testing reveals that test fixture is appropriate.

6. FUTURE WORK

Future work related to this project consists of:

- Sizing the ITWD specimen to achieve crack growth prior to global buckling or compressive failure.

- Defining a test matrix for ITWD specimens.

- Implement the shodow moire technique to characterize full field out-of-plane displacements of the delaminated region as well as global bending.

- Beam theory analysis of ITWD specimen including global bending.

- Finite element analysis of the ITWD specimen to assess beam theory results.

- Prediction of the onset of delamination growth for CYCOM 982 and APC-2 via mixed-mode fracture criteria.

- Assessment of nonlinear effects in interlaminar fracture.

REFERENCES

1. J. W. Gillespie and R. B. Pipes, "Compressive Strength of Composite laminates with Interlaminar Defects," Composite Structures, Vol. 2, 1984, p. 49.

2. J. W. Gillespie and R. B. Pipes, "Compressive Strength of Composite Laminates with Interlaminar Defects," CCM-79-17, Center for Composite Materials, University of Delaware, 1979.

3. J. D. Webster, "Flaw Criticality of Circular Disbond Defects in Composite Laminates," CCM-81-03, Center for Composite Materials, University of Delaware, 1981.

4. M. Ashizawa, "Fast Interlaminar Fracture of a Compressively Loaded Composite Containing a Defect," Douglas Paper 6994, January 1981.

5. M. Ashizawa, "Improving Damage Tolerance of Laminated Composites Through the Use of New Tough Resins," Douglas Paper 7250, January 1983.

6. R. L. Ramkumar, S. V. Kulkarni, and R. B. Pipes, "Definition and Modeling of Critical Flaws in Graphite Fiber Reinforced Epoxy Resin Matrix Composite Materials," Naval Air Development Center Report No. NADC-76228-30, January 1978.

7. S. N. Chatterjee, Z. Hashin, and R. B. Pipes, "Definition and Modeling of Critical Flaws in Graphite Fiber Reinforced Resin Matrix Composite Materials," Naval Air Development Center Report No. NADC 77278-30, August 1979.

8. S. N. Chatterjee and R. B. Pipes, "Composite Defect Significance," Proceedings of the Mechanics of Composites Review Meeting, Dayton, Ohio, October 1982.

9. J. D. Whitcomb, "Finite Element Analysis of Instability Related Delamination Growth," J. Composite Materials, Vol. 15, Sept. 1981, pp. 403.

10. J. D. Whitcomb, "Approximate Analysis of Postbuckled Through-Width Delaminations," NASA Technical Memorandum 83167, June 1981.

11. J. D. Whitcomb, "Strain Energy Release Rate Analysis of Cyclic Delamination Growth in Compressively Loaded Laminates," NASA Technical Memorandum 84598, January 1983.

12. J. D. Whitcomb, "Delamination Growth in Compressively Loaded Laminates," Presented at the ASTM Symposium on Effects of Defects in Composite Materials, San Francisco, California, December 1982.

13. J. D. Whitcomb, "Parametric Analytical Study of Instability-Related Delamination Growth," paper presented at the CCM Symposium 24-25 Sept. 1984.

14. D. J. Wilkins, J. R. Eisenmann, R. A. Camin, W. S. Margolis, and R. A. Benson, "Characterizing Delamination Growth in Graphite/Epoxy," Damage in Composite Materials, ASTM STP 775, 1982, p. 168.

15. R. L. Ramkumar, "Performance of a Quantitative Study of Instability-Related Delamination Growth," NASA Contract Report No. NASA-16727, March 1983.

16. A. J. Russell and K. N. Street, "Factors Affecting the Interlaminar Fracture Energy of Graphite/Epoxy Laminates," Hayashi, T. et. al. ed., ICCM-IV, Tokyo, 1982.

17. G. B. Murri and T. K. O'Brien, "Interlaminar G_{IIc} evaluation of Toughened Resin Matrix Composites Using the End-Notched Flexure Test," 26th AIAA/ASME/ASCE/AHS Structures, Structural Dynamics and Materials Conference, Orlando, April 15, 1985.

18. D. R. Carlile and D. C. Leach, "Damage and Notch Sensitivity of Graphite-PEEK Composites," Sampe Conference, Cincinnati, (USA), October 2-3, 1983.

19. H. Chai, "The Growth of Impact Damage in Compressively Loaded Laminates," Ph.D. Thesis, CalTech, March, (1982).

20. ADINA: A Finite Element Program for Automatic Dynamic Incremental Nonlinear Analysis, Report AE81-ADINA Engineering INC., September 1981.

21. E. F. Rybicki and M. F. Kanninen, "A Finite Element Calculation of Stress Intensity Factors By a Modified Crack Closure Integral," Eng. Fracture Mechanics, Vol. 9, 1977, p. 931.

22. B. Torstenfelt, "Finite Elements in Contact and Friction Applications, " Ph.D. Dissertation No. 103, Linkoping University, Sweden (1983).

23. K. R. Bathe and A. Chandhany, "A Solution Method for Planar and Axisymmetric Contact Problems," Int. J. Num. Meth. Eng. in Press, (1985).

24. J. D. Barrett and R. O. Foshi, "Mode II Stress Intensity Factors for Cracked Wood Beams," Eng. Fracture Mechanics, Vol. 9, (1977), p. 371.

25. W. L. Bradley and R. N. Cohen, "Matrix Deformation and Fracture in Graphite-Reinforced Epoxies," Delamination and Debonding of Materials, ASTM STP 876, (1985), p. 389.

26. D. C. Leach and D. R. Moore, "Toughness of Aromatic Polymer Composites," presented at a Symposium at University of Delaware, September, 1984, to be published in Composites Science and Technology.

27. A. J. Russell and K. N. Street, "The Effect of Matrix Toughness on Delamination: Static and Fatigue Fracture Under Mode II Shear Loading of Graphite Fiber Composites," presented at NASA/ASTM Symposium on Toughened Composites, Houston, TX, March, 1985.

28. R. W Boyle, "A Method for Determining Crack Growth in Notched Sheet Specimens," Mater. Res. Stand., 2, (1968), p. 646.

29. A. Smiley, "Rate Sensitivity of Interlaminar Fracture Toughness," MSc. Thesis, University of Delaware,(1985).

30. A. J. Kinloch and R. J. Young," Fracture Behavior of Polymers," Applied Sci. Publishers Ltd., (1983).

31. A. Chudnovsky, "Crack Layer Theory", NASA Report NAG-3-23, Dec. 1983, NASA Lewis Research Center.

32. A. Chudnovsky, A. Dolgopolsky and M. Cachanov, "On Stress Analysis of a Crack Layer", NASA Report NAG-3-223, Oct. 1984, NASA Lewis Research Center.

APPENDIX 1

Data Reduction schemes for DCB, ENF and CLS Specimens

1. DCB DATA REDUCTION

1.1 Compliance Method [1]

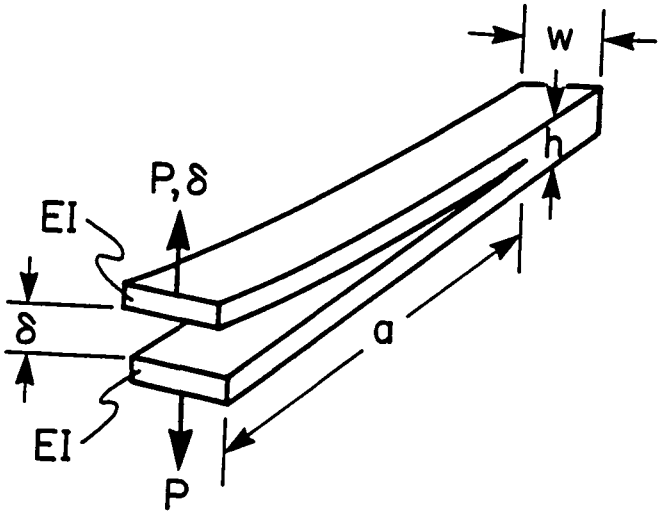

$$\delta = 2Pa^3/3EI$$

$$C = \delta/P = 2a^3/3EI = A_1 a^3 \qquad (1)$$

where $A_1 = \frac{2}{3EI}$

The energy release rate G is obtained from

$$G = \frac{P^2}{2w}\frac{dC}{da} \qquad (2)$$

Eq. (1) in (2) gives

$$G = 3A_1P^2a^2/2w \tag{3}$$

$G = G_c$ for $P = P_c$ gives

$$3A_1^2P_c^2\, a/2w = G_c \tag{4}$$

$$P_c = \sqrt{\frac{2w\,G_c}{3A_1}}\,\frac{1}{a} \tag{5}$$

consequently

$$P_c = A_2/a \tag{6}$$

Experimentally the C-a and P_c-a relations are measured giving the constants A_1 and A_2.

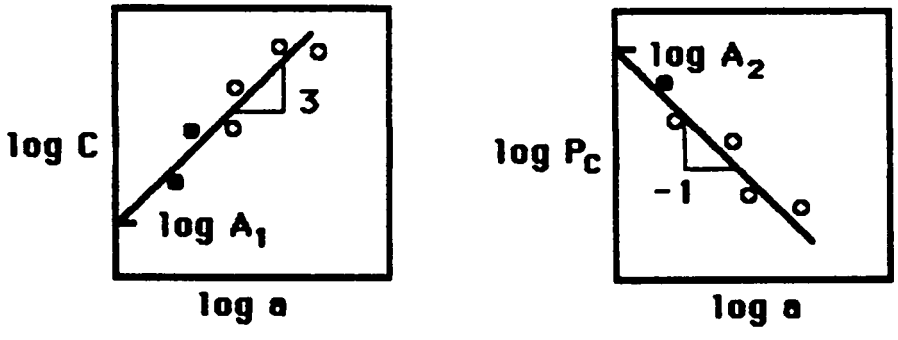

The critical energy release rate G_c is obtained by substituting Equation (6) into Equation (4).

$$G_c = 3A_1A_2^2/2w \tag{7}$$

1.2. Area Method [2]

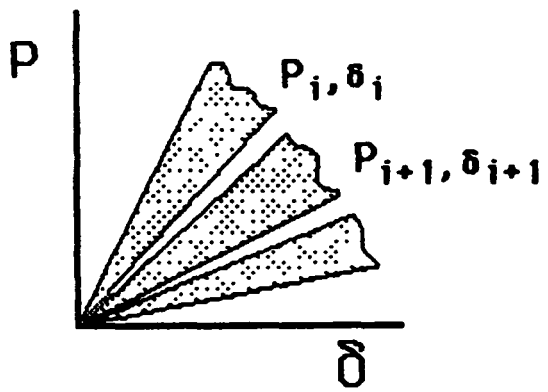

For linear elastic behavior and the case where the load deflection curve during crack propagation can be approximated by a straight line, the energy release rate can be determined from,

$$G = \frac{1}{2w\Delta a} \left| P_1\delta_{1+1} - P_{1+1}\delta_1 \right| \tag{8}$$

This quantity is equal to the area between the loading and unloading curves. An average G_{IC} value may be obtained from a series of loading and unloading curves.

2. CLS DATA REDUCTION

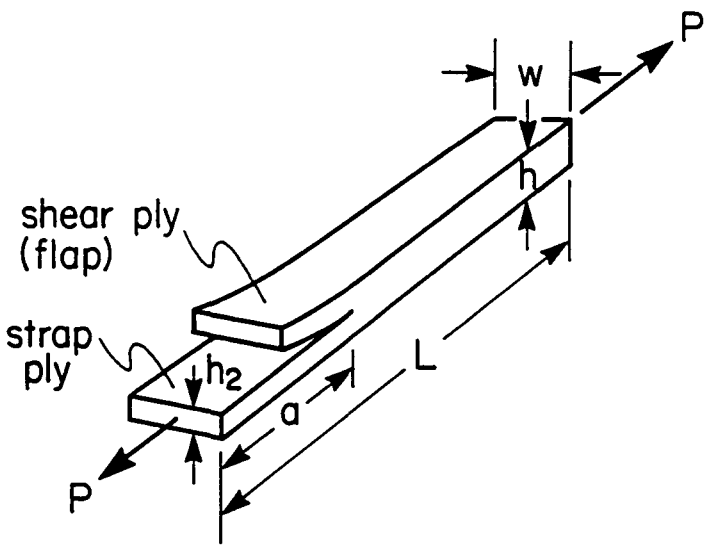

Strength of materials analysis gives:

$$\delta = \frac{P(L-a)}{wh_1E} + \frac{Pa}{wh_2E} \tag{9}$$

$$C = \frac{\delta}{P} = \frac{(L-a)}{wh_1E} + \frac{a}{wh_2E} = \frac{L}{wEh_1} + \frac{A(h_1-h_2)}{wEh_1h_2} \tag{10}$$

$$G_c = \frac{P_c^2}{2w} \frac{dC}{da} \tag{11}$$

From Equation (10), C may be expressed as a linear function of a,

$$C = A_3 a + A_4 \tag{12}$$

Equations (11) and (12) give

$$G_c = \frac{p_c^2}{2w} A_3 \tag{13}$$

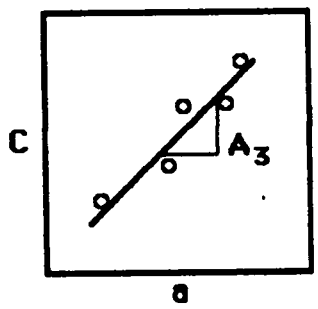

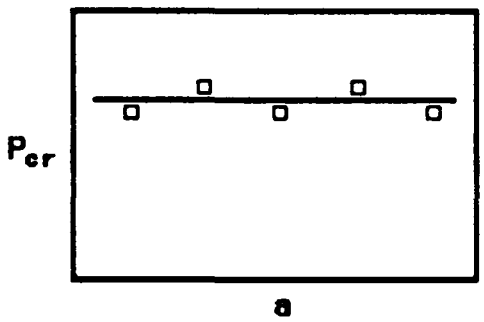

3. ENF DATA REDUCTION [3]

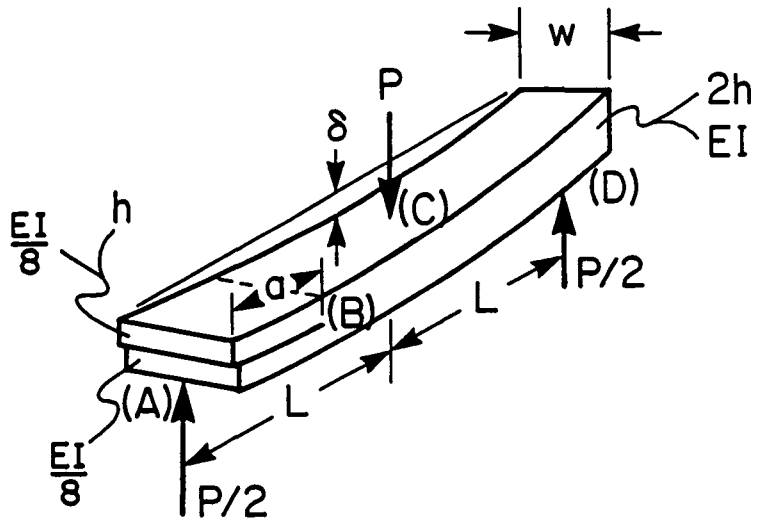

For the undelaminated regions BC and CD the displacements are,

$$\Delta_{BC} = P[2L^3 - 3aL^2 + a^3]/8Ewh^3 \qquad (14)$$

$$\Delta_{CD} = PL^3/4Ewh^3 \qquad (15)$$

The deflection of the delaminated region due to the slope at B is:

$$\Delta_{AB,S} = 3P[aL^2 - a^3]/8Ewh^3 \qquad (16)$$

The deflection of the delaminated region due to bending is,

$$\Delta_{AB,B} = Pa^3/Ewh^3 \tag{17}$$

Total deflection of the delaminated part is then:

$$\Delta_{AB} = \Delta_{AB,S} + \Delta_{AB,B} = \frac{3P(aL^2-a^3)}{8Ewh^3} + \frac{8Pa^3}{8Ewh^3} \tag{18}$$

$$= \frac{P[aL^2+ 5a^3]}{8Ewh^3}$$

For small deflections the total deflection δ is:

$$\delta = (\Delta_{BC} + \Delta_{CD} + \Delta_{AB})/2 \tag{19}$$

$$\delta = \frac{P}{8Ewh^3} [2L^3 + 3a^3] \tag{20}$$

The compliance C may thus be expressed:

$$C = \frac{\delta}{P} = \frac{[2L^3 + 3a^3]}{8Ewh^3} \tag{21}$$

$$\frac{dC}{da} = \frac{9a^2}{8Ewh^3} = \frac{9a^2C}{[2L^3 + 3a^3]} \tag{22}$$

$$G = \frac{P^2}{2w}\frac{dC}{da} = \frac{9a^2P^2C}{2w[2L^3 + 3a^3]} \tag{23}$$

$$C = \frac{2L^3}{8Ewh^3} + \frac{3a^3}{8Ewh^3} = A_5a^3 + A_6 \tag{24}$$

$$\frac{dC}{da} = 3A_5 a^2 \tag{25}$$

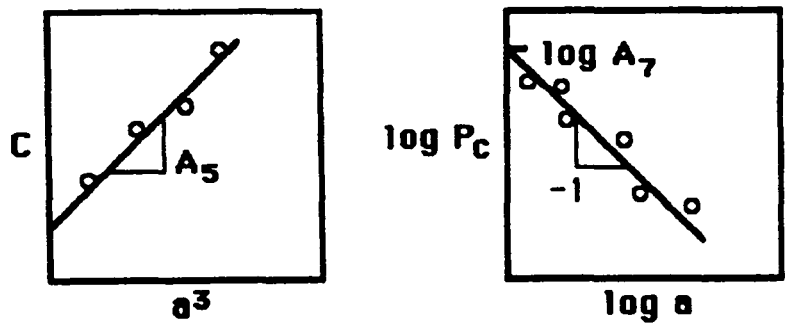

$$G_c = \frac{P_c^2 \, 3A_5 a^2}{2w} \tag{26}$$

$$P_c = \sqrt{\frac{2wG_c}{3A_5}} \frac{1}{a} = A_7/a \tag{27}$$

$$G_c = 3A_5 A_7^2/2w \tag{28}$$

In many cases unstable crack growth occurs with this specimen. For that case G_c is calculated directly from Eq. (22),

$$G_c = \frac{9a^2 P_c^2 C}{2w(2L^3+3a^3)} \tag{29}$$

where C is the measured compliance (corrected for the machine compliance).

REFERENCES

[1] D. J. Wilkins, J. R. Eisenmann, R. A. Camin, W. S. Margolis and R. A. Benson, "Characterizing Delamination Growth in Graphite/Epoxy", Damage in Composite Materials, ASTM STP 775,(1982), p. 168

[2] J. M. Whitney, C. E. Browning and Hoogsteden, W.,"A Double Cantilevier Beam Test for Characterizing Mode I Delamination of Composite Materials", J. Reinforced Plastics and Composites, vol. 1, (1982),p. 297

[3] A. J. Russell and K. N. Street, "Moisture and Temperature effects on the mixed-mode delamination fracture of unidirectional Graphite/Epoxy" Paper presented at an ASTM Symposium on Delamination and debonding of Materials, Nov. 8-10, (1983) Pittsburgh, Pennsylvania

APPENDIX 2

Stability of Crack Growth For the ENF Specimen [1]

The stability of crack growth may be judged from the sign of dG_{II}/da. If dG_{II}/da is positive unstable crack growth will occur, while stable crack growth occur if dG_{II}/da is zero or negative. G_{II} is obtained from the general expression:

$$G_{II} = \frac{P^2}{2w}\frac{dC}{da} \tag{1}$$

For fixed load conditions dG_{II}/da is directly obtained from eq. (22), Appendix 1,

$$\frac{dG_{II}}{da} = \frac{9aP^2}{8Ew^2h^3} \tag{2}$$

This quantity is always positive, hence the crack growth is unstable.

For fixed grip conditions, which is more common in testing G_{II} is expressed by

$$G_{II} = \frac{\delta^2}{2wC^2} \frac{dC}{da} \tag{3}$$

Differentiation of this expression yields:

$$\frac{dG_{II}}{da} = \frac{\delta^2}{2wC^2} \left[\frac{d^2C}{da^2} - \frac{2}{C} \left(\frac{dC}{da}\right)^2\right] \tag{4}$$

If the influence of shear is neglected, Eq. (22),Appendix 1, gives,

$$\frac{dG_{II}}{da} = \frac{9\delta^2 a}{8Ew^2h^3C^2} \left[1 - \frac{9a^3}{2L^3 + 3a^3}\right] \tag{5}$$

For stable crack growth, a ,is thus required to be:

$$a > L/\sqrt[3]{3} \approx 0.7L \tag{6}$$

Consequently for the commonly used a/L ≈ 0.5, the crack growth is unstable under fixed grip conditions.

REFERENCE

[1] L.A. Carlsson, J.W. Gillespie and R.B. Pipes, "On the Analysis of the End Notched Flexure (ENF) Specimen for Mode II Testing", Submitted for Publication.

APPENDIX 3

Design Considerations for DCB, ENF and CLS Specimens

1. DCB Specimen Design

The main requirement on the DCB specimen is that the beams act as linear elastic beams. An investigation by Dewitt et. al [1] shows that geometric nonlinearities occur in the DCB specimen for

$$\frac{\delta}{2a} > 0.3 \qquad (1)$$

See Figure 1.

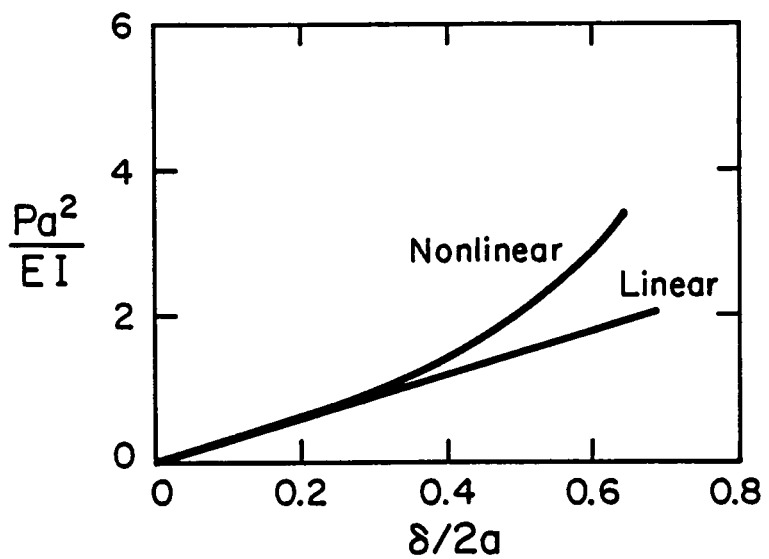

Fig. 1 Nondimensional load vs. nondimensional displacement [1]

At $\delta/2a = 0.3$, i.e. $\delta/a = 0.6$ the error induced in the load by assuming linear behaviour is approximately 10%. This is also the error in G [1].

Relation between the thickness required to keep the beams in the linear regime and G_c.

Equation (1) in Appendix 1 is

$$C = A_1 a^3 \tag{1}$$

in which $A_1 = \frac{2}{3EI}$

Here EI is the flexural rigidity of each beam of the DCB specimen. Consequently,

$$I = w(h/2)^3/12 = wh^3/96 \tag{2}$$

This in Equation (1) yeilds,

$$C = \frac{64a^3}{Ewh^3} \tag{3}$$

or

$$\delta_c = \frac{64a^3}{Ewh^3} P_c \tag{4}$$

The critical strain energy release rate may be expressed as

$$G_c = \frac{96P_c^2 a^2}{Ew^2h^3} \tag{5}$$

Substitution into Equation (4) gives

$$\frac{\delta_c}{a} = a\sqrt{\frac{128G_c}{Eh^3}} \tag{6}$$

To keep δ_c/a less or equal to 0.6 requires:

$$a\sqrt{\frac{128G_c}{3Eh^3}} < 0.6 \tag{7}$$

or

$$\frac{128G_c a^2}{3Eh^3} < 0.36 \tag{8}$$

This is equivalent to,

$$h > 4.9\ (G_c/E)^{1/3}\ a^{2/3} \tag{9}$$

Note that the required thickness increases with crack length a. The longest crack length expected in the testing is about 150 mm

2. CLS Specimen Design

The design of the CLS specimen has been discussed by Mangalari and Johnson [2]. Based on the two possible failure modes, viz. delamination and adherend failure, the minimum thickness may be determined. Figure 2 shows the geometry of the specimen.

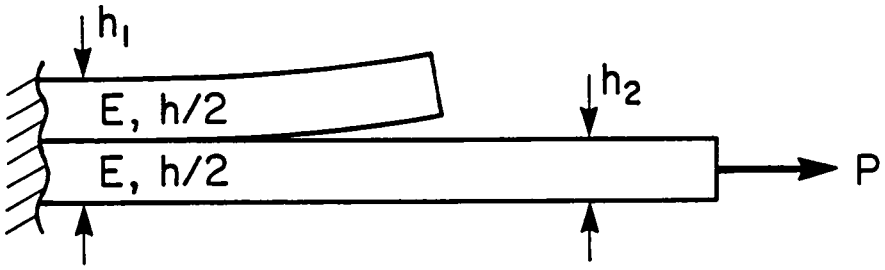

Fig. 2 Geometry of the CLS specimen.

From Equations (10) and (11) in Appendix 1,

$$G_c = \frac{P_c^2}{2w^2} \frac{(h_1-h_2)}{Eh_1h_2} \tag{10}$$

With $h_1 = h$, $h_2 = h/2$ we get

$$G_c = \frac{P_c^2}{2w^2Eh} \tag{11}$$

i.e.

$$P_c = w\sqrt{2EhG_c} \tag{12}$$

To avoid failure in the strap ply (if the stress concentration at the crack tip and the rotation of the specimen is neglected) we need

$$P_c < X_1^T wh_2 \tag{13}$$

where X_1^T is the uniaxial tensile strength.

Equations (12) and (13) yield

$$w\sqrt{2EhG_c} \leq X_1^T wh/2 \tag{14}$$

This yields:

$$h \geq 8EG_c/(X_1^T)^2 \tag{15}$$

3. ENF Specimen Design [3]

The analysis of the ENF specimen presented here, is based on small deflection theory. Large deflection/rotations increase the complexities of the analysis and the data reduction scheme substantially. In this section, an analysis based on beam theory, will be presented which allows sizing of the ENF specimen to obtain crack growth within the linear elastic regime. Influences of interlaminar shear and friction are not considered in this approximate analysis.

In linear beam theory the following expression for the curvature:

$$\frac{1}{R} = \frac{d^2y/dx^2}{\left[1 + (dy/dx)^2\right]^{3/2}} \tag{16}$$

is generally approximated with

$$1/R \approx d^2y/dx^2 \tag{17}$$

since the square of the slope $(dy/dx)^2$ is assumed to be much less than unity.

The maximum slope occurs at the end of the delaminated region. Neglecting influence of shear deformation it may be calculated from the slope of the beam at the tip of the delaminated crack

$$\left(\frac{dy}{dx}\right)_B = \frac{3P(L^2-a^2)}{8Ewh^3} \tag{18}$$

The slope due to bending of the delaminated beams is obtained from the deflection curve for a cantilever beam (see Appendix 4).

$$y = \frac{-P}{4I}\left(\frac{x^3}{6E} - \frac{a^2x}{2E} + \frac{a^3}{3E}\right) \tag{19}$$

$$\frac{\partial y}{\partial x} = \frac{-P}{8EI}(x^2 - a^2) \tag{20}$$

The maximum slope occurs at x = 0 and is

$$\left(\frac{\partial v}{\partial x}\right)_0 = \frac{Pa^2}{8EI} \tag{21}$$

This leads to

$$\left(\frac{dy}{dx}\right)_0 = \frac{3Pa^2}{2Ewh^3} \tag{22}$$

The maximum slope is then approximately

$$\left(\frac{dy}{dx}\right)_m \approx \left(\frac{dy}{dx}\right)_B + \left(\frac{dy}{dx}\right)_0 \tag{23}$$

Equations (18) and (22) give:

$$\left(\frac{dy}{dx}\right)_m = \frac{3P(L^2+3a^2)}{8Ewh^3} \tag{24}$$

In terms of displacement, δ, the maximum slope is:

$$\left(\frac{dy}{dx}\right)_m = \frac{3(L^2 + 3a^2)\delta}{2L^3 + 3a^3} \tag{25}$$

For $(dy/dx)_m < 0.2$ the error in eq. (16) is approximately 6%. The integrated form of eq. (16) which should be employed in a large deflection analysis would lead to less than 6% error since the above estimate is based on the maximum slope, at a point.

Denoting the maximum allowable slope by y_a^1, the maximum allowable displacement, δ_a, corresponding to y_a^1 may be calculated from Eq. (25),

$$\delta_m < \frac{y_a^1 (2L^3 + 3a^3)}{3(L^2 + 3a^2)} \tag{26}$$

Relation between δ_c and G_{IIc}

$$G_{IIc} = \frac{9P_c a^2 \delta_c}{2w(2L^3 + 3a^3)} \tag{27}$$

The critical load P_c may also be obtained from Eq. (20) of Appendix 1,

$$P_c = \frac{8wEh^3}{2L^3 + 3a^3}\,\delta_c \tag{28}$$

Substitution into Eq. (28) yields,

$$\delta_c = \frac{(2L^3+3a^3)}{6a}\sqrt{\frac{G_{IIc}}{E_1 h^3}} \tag{29}$$

Combination of Eqs. (29) and (26) with the requirement $\delta_c < \delta_m$ gives:

$$G_{IIc} < \frac{4(y_a^1)^2 a^2 Eh^3}{(L^2 + 3a^2)^2} \tag{30}$$

This relation shows that the small deflection regime may be increased by increasing E and h or by decreasing L. For example, if thickness is the controlling parameter,

$$h > \sqrt[3]{\frac{G_{IIc}\,(L^2+3a^2)^2}{4(y_a^1)^2\, a^2 E}} \tag{31}$$

Designing versus nonlinear material behavior or flexural failure

Material nonlinearities or flexural failure may also be avoided by proper sizing of the ENF specimen. For crack lengths, a, less than or equal to L/2 the maximum bending stress (disregarding the localized stress singularity at the crack tip) occurs in the center of the beam.

The maximum bending moment is,

$$M = \frac{P}{2} L \tag{32}$$

The maximum bending stress is

$$\sigma_m = Mh/I \tag{33}$$

Combination of equations (32) and (33) gives

$$\sigma_m = \frac{PLh}{2I} = \frac{3PL}{4wh^2} \tag{34}$$

The maximum strain ε_m is then,

$$\varepsilon_m = \frac{\sigma_m}{E} = \frac{3PL}{4Ewh^2} \tag{35}$$

In terms of displacement this gives

$$\varepsilon_m = \frac{6Lh\delta}{2L^3+3a^3} \tag{36}$$

where δ is the displacement of the central loading pin. By similar reasoning, a thickness requirement may be formulated from the condition $\delta_c < \delta_a$ where δ_a is the maximum allowable displacement related to the maximum allowable strain, $\varepsilon_{m,a}$, to maintain linear material behavior. Calculations of the required thickness yields:

$$h > \frac{L^2 G_{IIc}}{a^2 \varepsilon_{m,a}^2 E} \tag{37}$$

REFERENCES

[1] D.F. Dewitt, R. A. Shapery and W. L. Bradley, "Method for determining the Mode I delamination Fracture toughness of Elastic and Viscoelastic Composite Materials", J. Compos. Material., Vol. 14, (1980), p. 270.

[2] P. D. Mangalgiri and S. W. Johnson, "Design of CLS Specimen for Different Resin Toughnesses", ASTM Meeting Minutes D 30.02.02, test group on interlaminar fracture toughness, measurement, Dallas/Ft. Worth, Oct. 24, (1984)

[3] L. A. Carlsson, J. W. Gillespie and R. B. Pipes, "On the analysis of the End Notched Flexure (ENF) Specimen for Mode II Testing", Submitted for publication.

APPENDIX 4

Influence of shear deformations on the ENF Compliance and strain energy release rate [1]

In Figure 1, the ENF specimen geometry is defined and modeled as three beams. For small deflections, the deflection, δ, at the center (C) is simply the algebraic sum,

$$\delta = \frac{\Delta_{CD} + \Delta_{BC} + \Delta_{AB}}{2} \qquad (1)$$

where Δ_{CD}, Δ_{BC}, and Δ_{AB} are the maximum deflections of the three beams CD, BC and AB, respectively. Beams BC and CD and modeled as the cantilever beam presented in Figure 2. The deflection due to a point load at one end including shear deformation [2] is,

$$\delta = \frac{P\ell^3}{3E_1 I} + \frac{P\ell h^2}{10G_{13} I} \qquad (2)$$

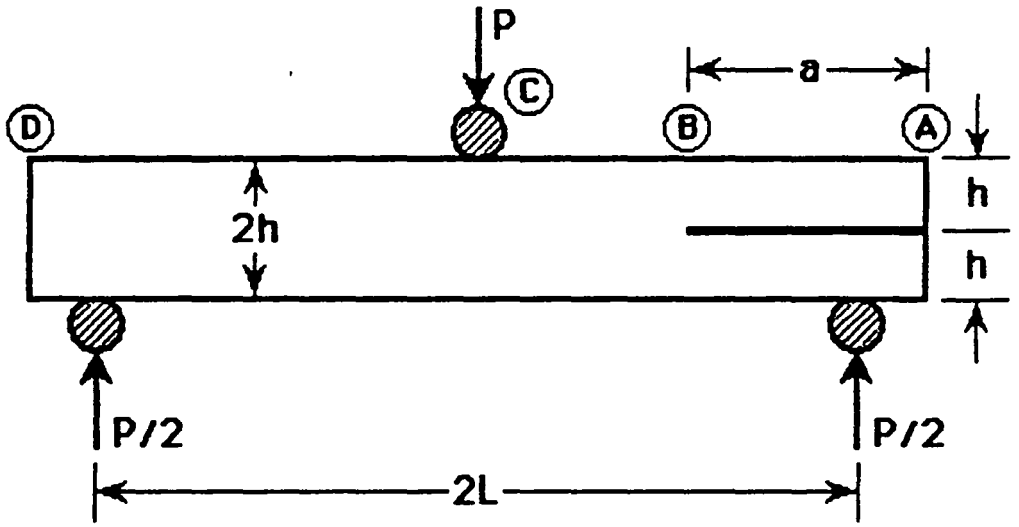

Fig. 1 ENF Geometry

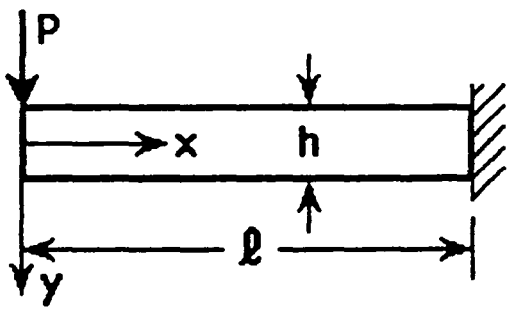

Fig. 2 Cantilever Beam

where E_1 and G_{13} are the flexural modulus and interlaminar shear modulus, respectively, and I is the moment of inertia of the beam. Implicit in the derivation of Equation (2) is the assumption that the built-in end does not warp under the action of shearing stress. This appears to be a reasonable assumption for beams CD and BC since the point of load introduciton (Point C) in Figure 1 is an approximate line of symmetry. Consequently,

$$\Delta_{CD} = \frac{PL^3}{4E_1wh^3} + 0.3\,\frac{PL}{G_{13}wh} \tag{3}$$

$$\Delta_{BC} = \frac{P(2L^3 - 3aL^2 + a^3)}{8E_1wh^3} + 0.3\,\frac{P(L - a)}{G_{13}wh} \tag{4}$$

For the delaminated region, AB, of the ENF geometry, the ends of the parallel beams at point B in Figure 1 are allowed to warp. For a beam of thickness h = 2c, the horizontal and vertical displacements (u,v), according to Timoshenko [3], may be expressed with respect to Figure 2 as

$$u = \frac{P}{I}\left(\frac{-x^2y}{2E_1} - \frac{\nu_{12}y^3}{6E_1} + \frac{y^3}{6G_{13}} + \frac{\ell^2y}{2E_1}\right) \tag{5}$$

$$v = \frac{P}{I}\left(\frac{\nu_{12}xy^2}{2E_1} + \frac{x^3}{6E_1} + \frac{dI}{P}(x-\ell) - \frac{\ell^3}{6E_1}\right) \qquad (6)$$

where

$$\frac{dI}{P} = -\frac{1}{2}\left(\frac{\ell^2}{E_1} + \frac{c^2}{G_{13}}\right) \qquad (7)$$

The total deformation of the delaminated region has two components. The bending and shearing deformation is defined in Equation (6). The second component arises from the rotation of the built-in end for the delaminated region at point B in Figure 1. The deflection, $\Delta_{AB,S}$ due to the local slope is shown to be [1]

$$\Delta_{AB,S} = \frac{P}{8E_1wh^3}\left(aL^2-a^3+ ah^2(E_1/G_{13})\right) \qquad (8)$$

The total deflection of the delaminated region assuming each beam carries an equal load of P/4 is obtained from the summation of Equations (6) and (8),

$$\Delta_{AB} = \frac{P}{8E_1wh^3}\left(3aL^2+5a^3+6ah^2(E_1/G_{13})\right) \qquad (9)$$

Substitution of Equations (3), (4) and (9) into (1) yields an expression for the displacement at the point of load introduction.

$$\delta = \frac{P}{w}\left(\frac{2L^3+3a^3}{8E_1h^3} + \frac{1.2L+0.9a}{4G_{13}h}\right) \tag{10}$$

The compliance including shear deformation is,

$$C_{SH} = \frac{\delta}{P} = \frac{2L^3 + 3a^3}{8E_1wh^3}\left(1 + \frac{2(1.2L + 0.9a)h^2E_1}{(2L^3+3a^3)G_{13}}\right) \tag{11}$$

This equation with,

$$G_{II}^{SH} = \frac{P^2}{2w}\frac{dC_{SH}}{da} \tag{12}$$

gives,

$$G_{II}^{SH} = \frac{9a^2P^2}{16E_1w^2h^3}\left(1 + 0.2\left(\frac{E_1}{G_{13}}\right)\left(\frac{h}{a}\right)^2\right) \tag{13}$$

Neglecting the contribution of shear deformation, Equations (11) and (13) simplify to the expression reported in [4],

$$C_{BT} = \frac{2L^3 + 3a^3}{8E_1wh^3} \tag{14}$$

and

$$G_{II}^{BT} = \frac{9a^2P^2}{16E_1w^2h^3} \tag{15}$$

REFERENCES

[1] L. A. Carlsson, J. W. Gillespie and R. B. Pipes, "On the Analysis of the End Notched Flexure (ENF) Specimen for Mode II Testing", Submitted for publication.

[2] S. P. Timoshenko, "Strength of Materials", Part 1, Krieger Publishing, (1984).

[3] S. P. Timoshenko and J. N. Goodier, "Theory of Elasticity", Mc-Graw Hill (1970)

[4] A. J. Russell, and K. N. Street., "Moisture and Temperature effects on the mixed-mode delamination fracture of unidirectional graphite/epoxy", Paper presented at an ASTM Symposium on Delamination and Debonding of Materials, Nov. 8-10, 1983, Pittsburgh, Pennsylvania.

APPENDIX 5

Influence of friction on the ENF Strain Energy Release Rate [1]

A potential, energy absorbing mechanism in the ENF specimen, is the friction between the crack surfaces. Finite element results discussed in Section 3 show that the contact area is located symmetrically over the outer support pin and is less than 4h in length where h is the thickness of each beam in the delaminated region. Summation of the normal forces within the contact area verifies that each beam carries an equal load.

With this insight, an approximate expression to quantify the work of friction during crack growth may be obtained from beam theory[1]. The frictional work, W_F, can be expressed as:

$$W_F = \int_{-2h}^{2h} \mu N(x) \Delta u(x) dx \qquad (1)$$

where μ is the coefficient of friction, $N(x)$ is the normal force distribution and $\Delta u(x)$ is the relative displacement (sliding) of the crack surfaces. The integral is calculated over the contact area.

The induced normal stress field may, as an approximation, be represented by the Dirac delta function, $\delta(x)$, [2]

$$N(x) = \frac{P}{4}\,\delta(x) \tag{2}$$

Substitution into Eq. (1) yields the following upper bound,

$$W_F \leq P\,u(0)/4 \tag{3}$$

The sliding, $\Delta u(0)$, may be calculated from the expression given in Timoshenko and Goodier [3] for the displacement of a cantilever beam:

$$\Delta u(0) = 2\,|u(0)| = \frac{3P}{2E_1 wh^2}\left[a^2 + h^2(E_1/G_{13})/12\right] \tag{4}$$

The frictional work is thus:

$$W_F = \frac{3P^2\mu}{8E_1 wh^2}\left[a^2 + h^2(E_1/G_{13})/12\right] \tag{5}$$

The crack growth criterion may be formulated by considering the energy changes as the crack increases its area by an amount dA:

$$\frac{dW}{dA} - \frac{dU}{dA} \geq G_{IIc} + \frac{dW_F}{dA} \tag{6}$$

where W is the work supplied by the movement of the external load, U is the stored strain energy in the body and G_{IIc} is the work required to create a unit new crack surface.

A resonable assumption is that the compliance of the specimen is unaffected by friction. For this case Eqs. (6), and (5) give:

$$G_{II}^{SH} > G_{IIc} + \frac{3P^2\mu a}{4E_1 w^2 h^2} \tag{7}$$

where G_{II}^{SH}, given in Appendix 4 is,

$$G_{II}^{SH} = \frac{9a^2P^2}{16E_1 w^2 h^3} \left[1 + 0.2(E_1/G_{13})(h/a)^2\right] \tag{8}$$

The energy available for creating new crack surfaces, may thus be expressed:

$$G_{II}(\mu) = G_{II}^{SH} - \frac{3P^2\mu a}{4E_1 w^2 h^2} \tag{9}$$

or by using equation (8):

$$G_{II}(\mu) = G_{II}^{BT}\left[1 + 0.2(E_1/G_{13})(h/a)^2 - 4\mu(h/a)/3\right] \tag{10}$$

where $G_{II}^{BT} = 9a^2P^2/(16E_1 w^2 h^2)$ is the expression for G_{II} where influences of interlaminar shear and friction are neglected.

A non-dimensional strain energy release rate parameter quantifying the influence of friction to the reduction in strain energy release rate is defined in Eq. (11),

$$\frac{G_{II}(\mu=0) - G_{II}(\mu)}{G_{II}^{BT}} = 4\mu(h/a)/3 \qquad (11)$$

The results discussed in Chapter 3 show that Eq.(11) indeed provides an upper bound to the numerical finite element results.

REFERENCES

[1] L. A. Carlsson, J. W. Gillespie and R. B. Pipes, "On the Analysis of the End Notched Flexure (ENF) Specimen for Mode II Testing", Submitted for publication.

[2] M.D. Greenberg, "Foundations of Applied Mathematics", Prentice-Hall (1978).

[3] S. P. Timoshenko, and J. N. Goodier, "Theory of elasticity", 3rd.ed., McGraw-Hill (1970).

APPENDIX 6

Stress-Strain Curves for APC-2 and CYCOM 982

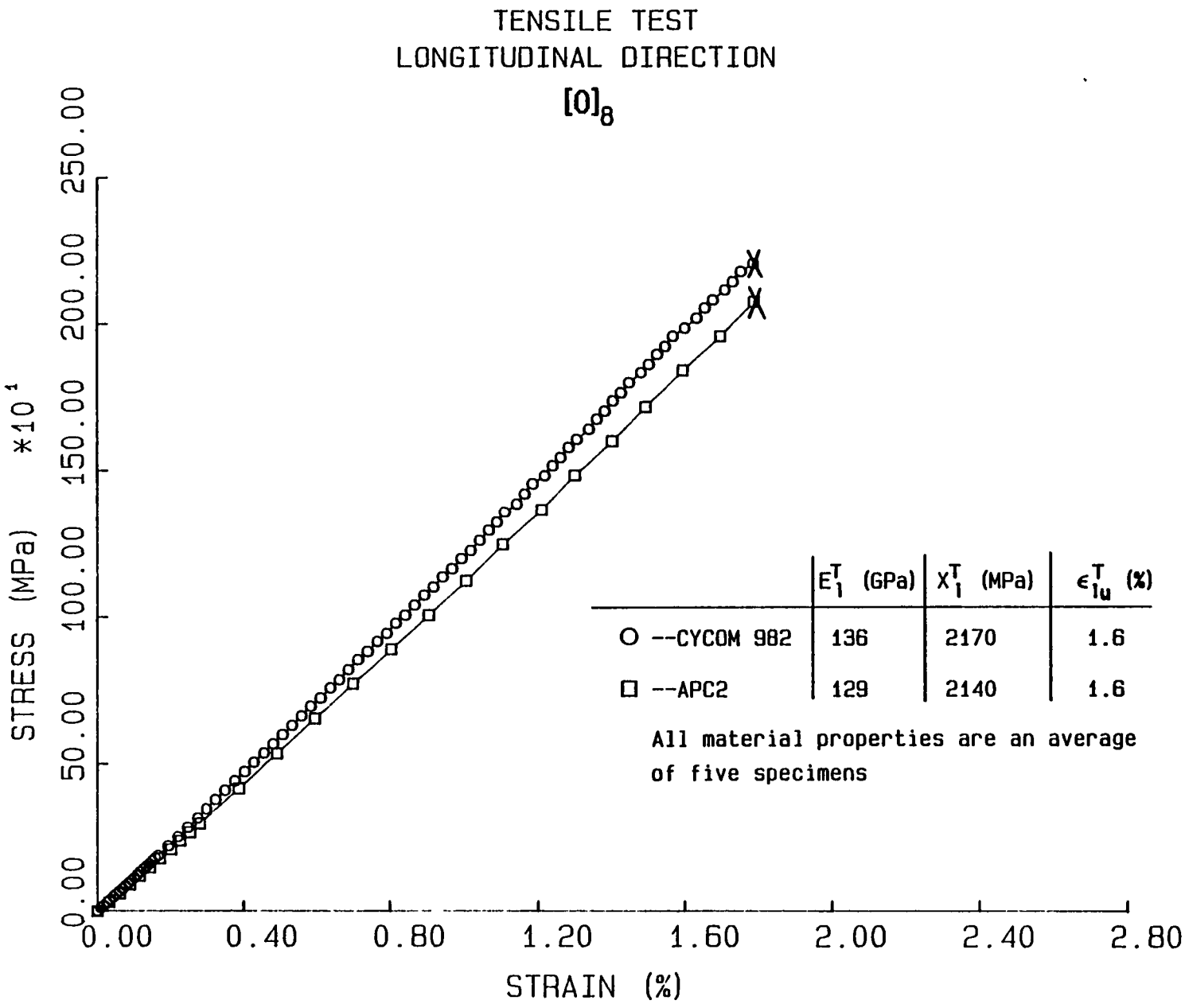

	E_1^T (GPa)	X_1^T (MPa)	ϵ_{1u}^T (%)
O --CYCOM 982	136	2170	1.6
□ --APC2	129	2140	1.6

All material properties are an average of five specimens

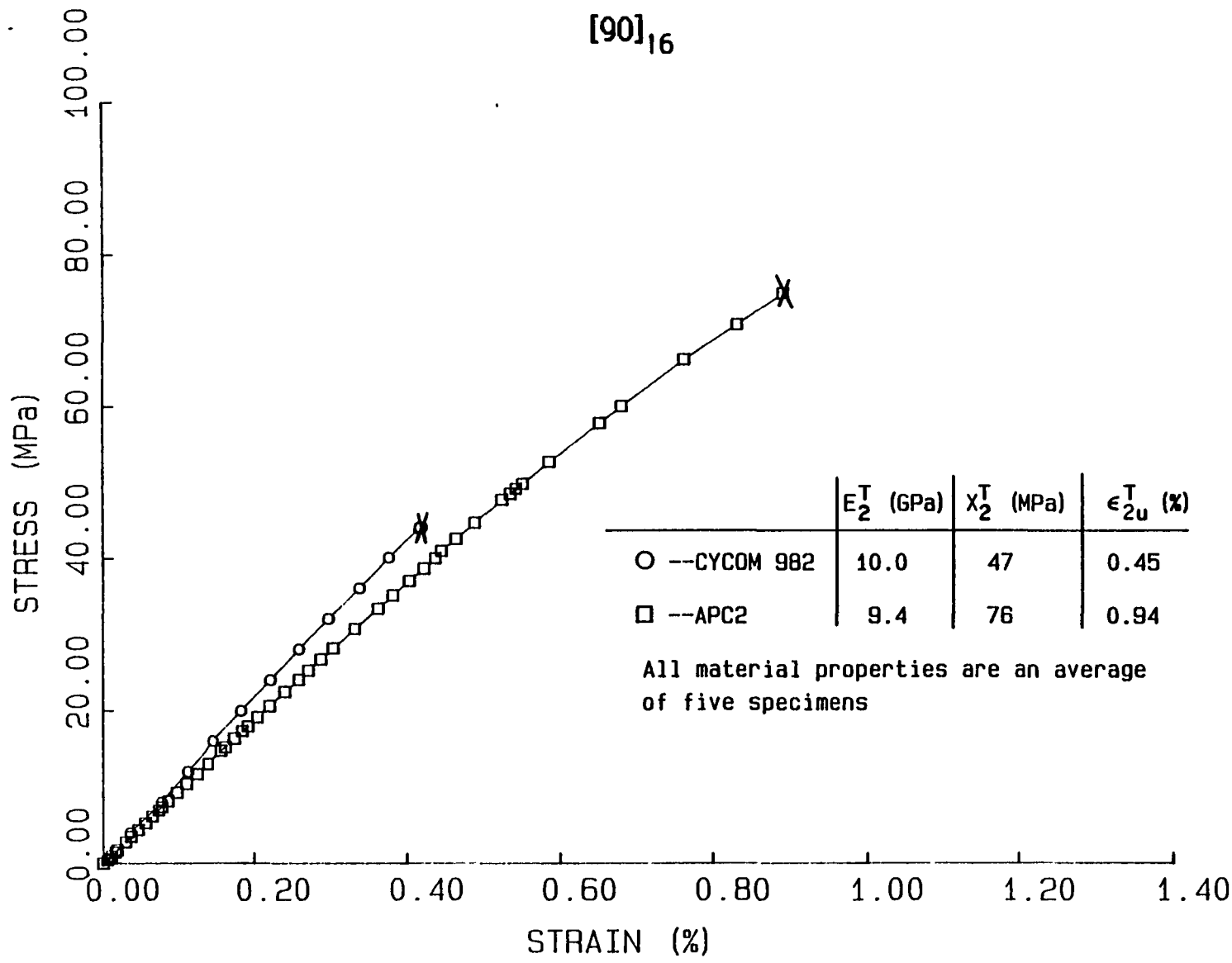
TENSILE TEST
TRANSVERSE DIRECTION
[90]16
STRESS (MPa)
0.00
20.00
40.00
60.00
80.00
100.00
0.00
0.20
0.40
0.60
0.80
1.00
1.20
1.40
STRAIN (%)
E2T (GPa)
X2T (MPa)
ε2uT (%)
O --CYCOM 982
10.0
47
0.45
□ --APC2
9.4
76
0.94
All material properties are an average of five specimens

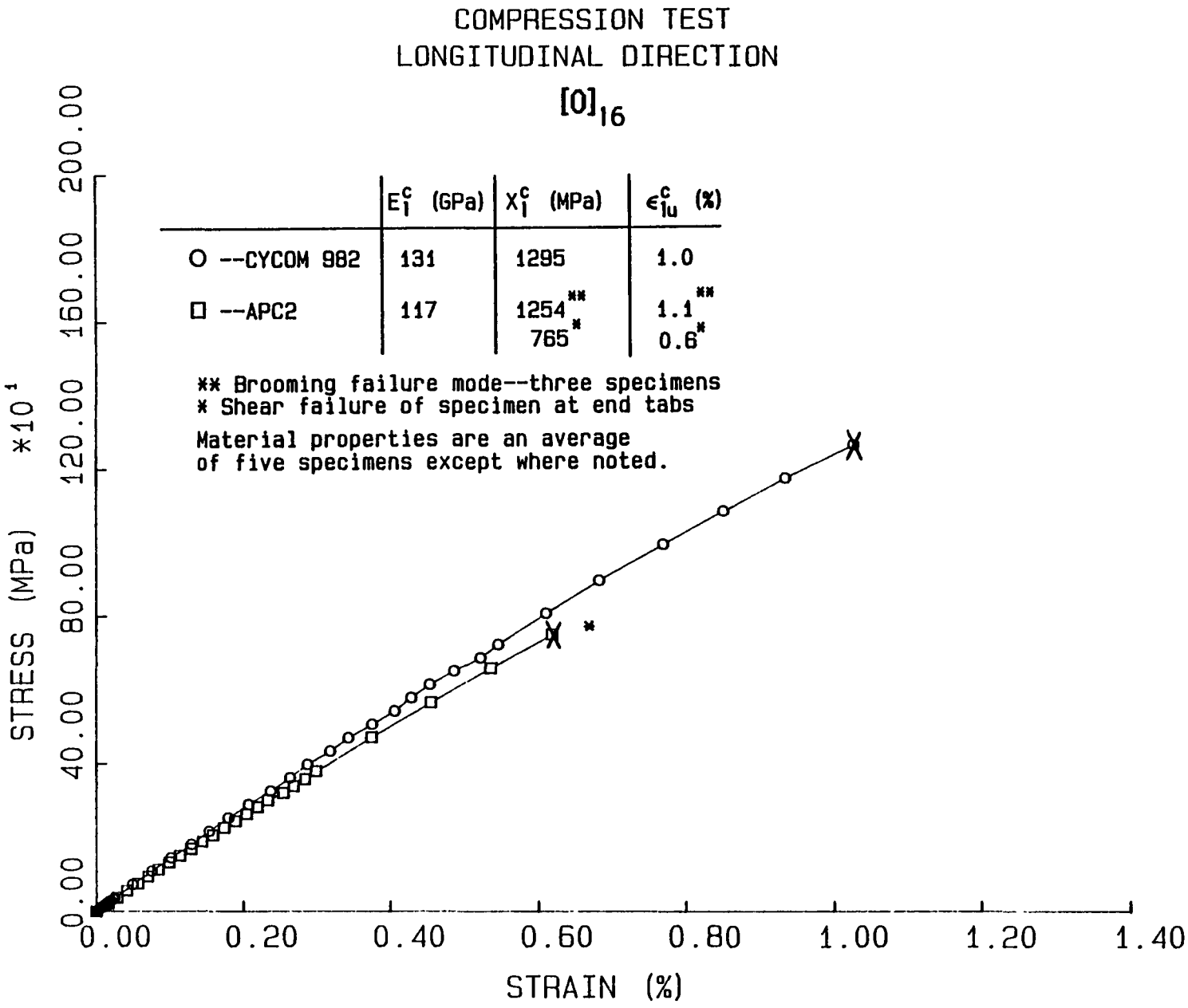
COMPRESSION TEST
LONGITUDINAL DIRECTION
[0]16
E1c (GPa)
X1c (MPa)
ε1uc (%)
O --CYCOM 982
131
1295
1.0
□ --APC2
117
1254**
765*
1.1**
0.6*
** Brooming failure mode--three specimens
* Shear failure of specimen at end tabs
Material properties are an average
of five specimens except where noted.
STRESS (MPa) *10¹
0.00
40.00
80.00
120.00
160.00
200.00
0.00
0.20
0.40
0.60
0.80
1.00
1.20
1.40
STRAIN (%)

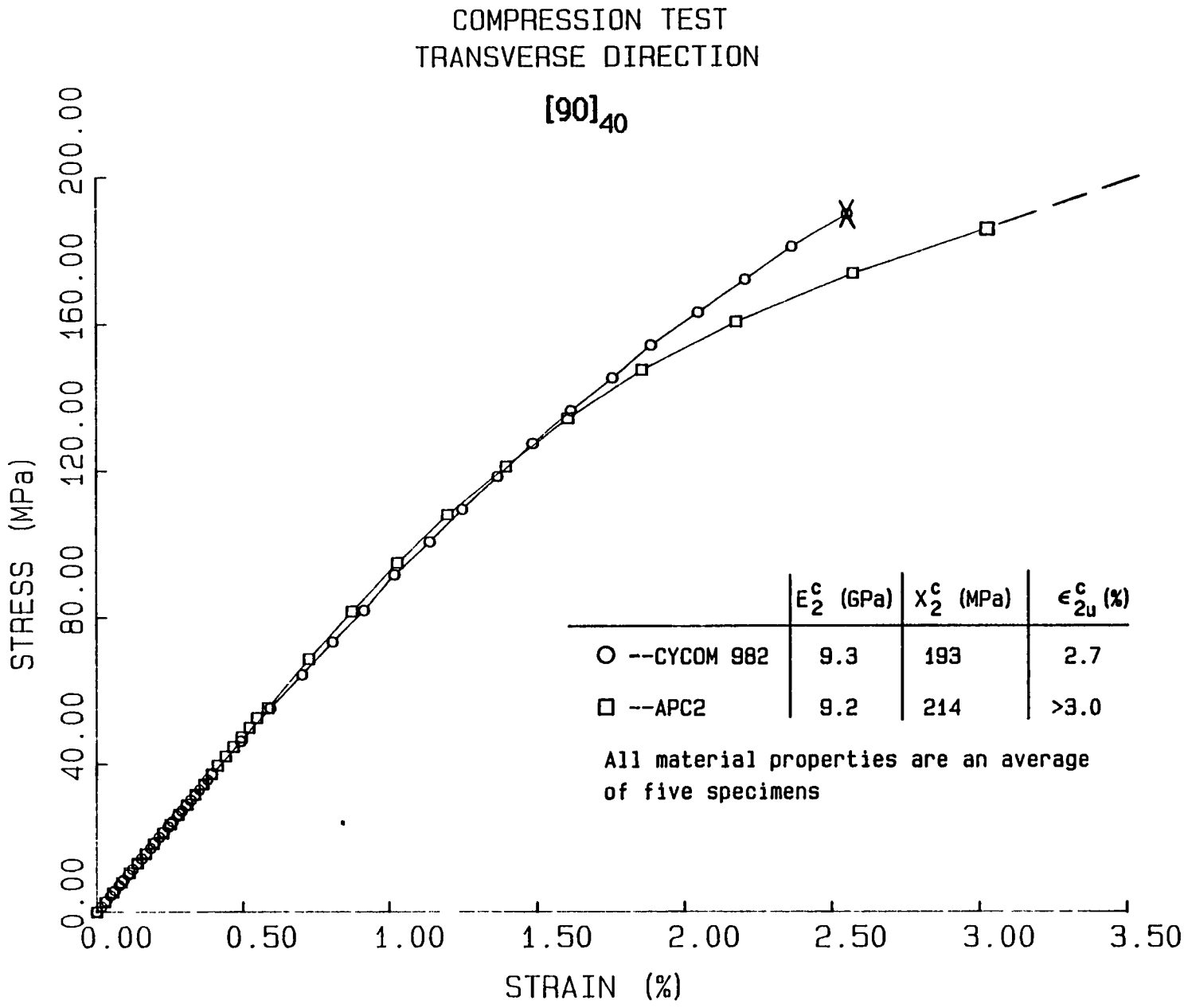
COMPRESSION TEST
TRANSVERSE DIRECTION
[90]40
STRESS (MPa)
0.00
40.00
80.00
120.00
160.00
200.00
0.00
0.50
1.00
1.50
2.00
2.50
3.00
3.50
STRAIN (%)
E2c (GPa)
X2c (MPa)
ε2uc (%)
O --CYCOM 982
9.3
193
2.7
□ --APC2
9.2
214
>3.0
All material properties are an average of five specimens

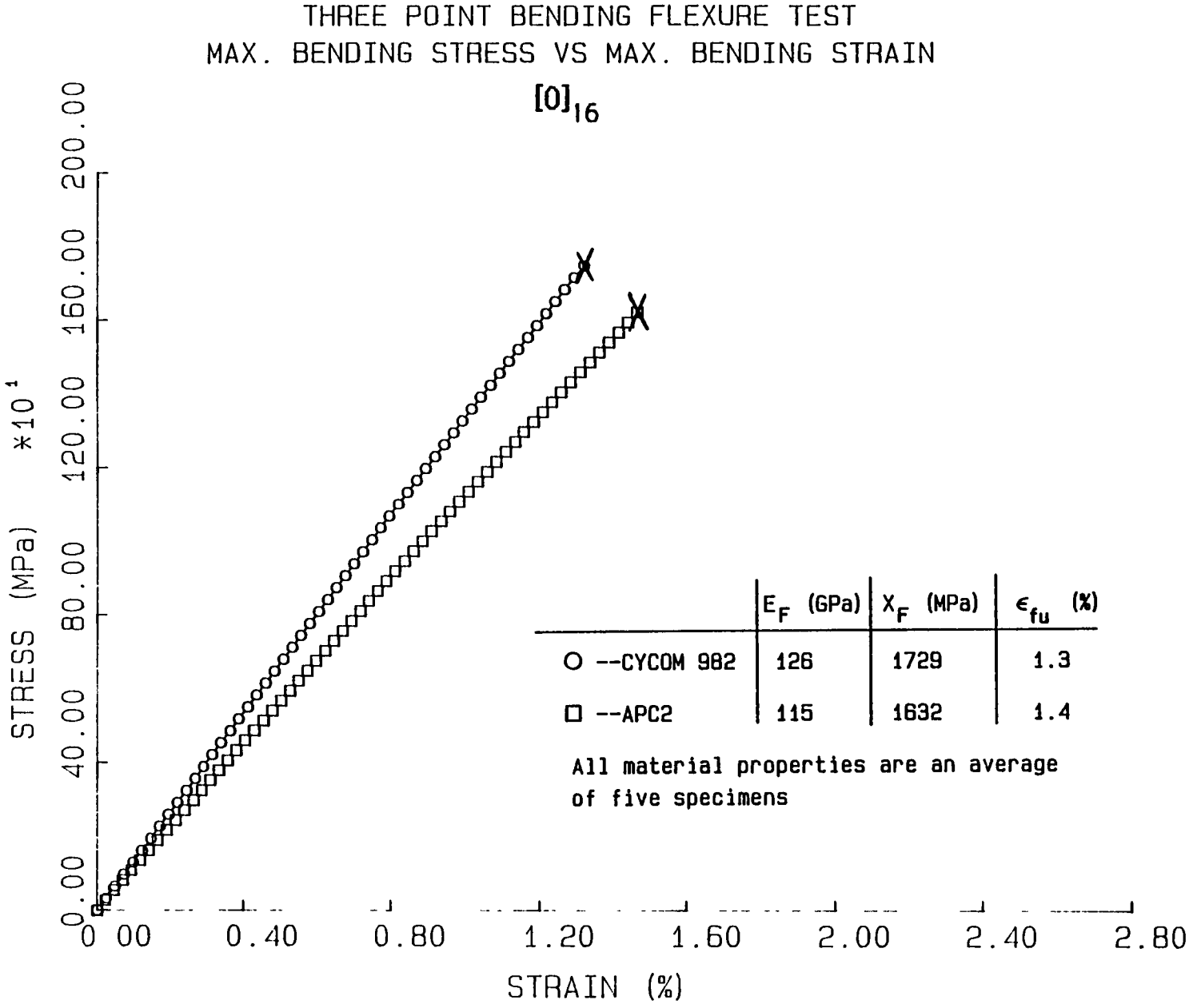
THREE POINT BENDING FLEXURE TEST
MAX. BENDING STRESS VS MAX. BENDING STRAIN
[0]16
STRESS (MPa) *10¹
0.00
40.00
80.00
120.00
160.00
200.00
0.00
0.40
0.80
1.20
1.60
2.00
2.40
2.80
STRAIN (%)
EF (GPa)
XF (MPa)
εfu (%)
O --CYCOM 982
126
1729
1.3
□ --APC2
115
1632
1.4
All material properties are an average of five specimens

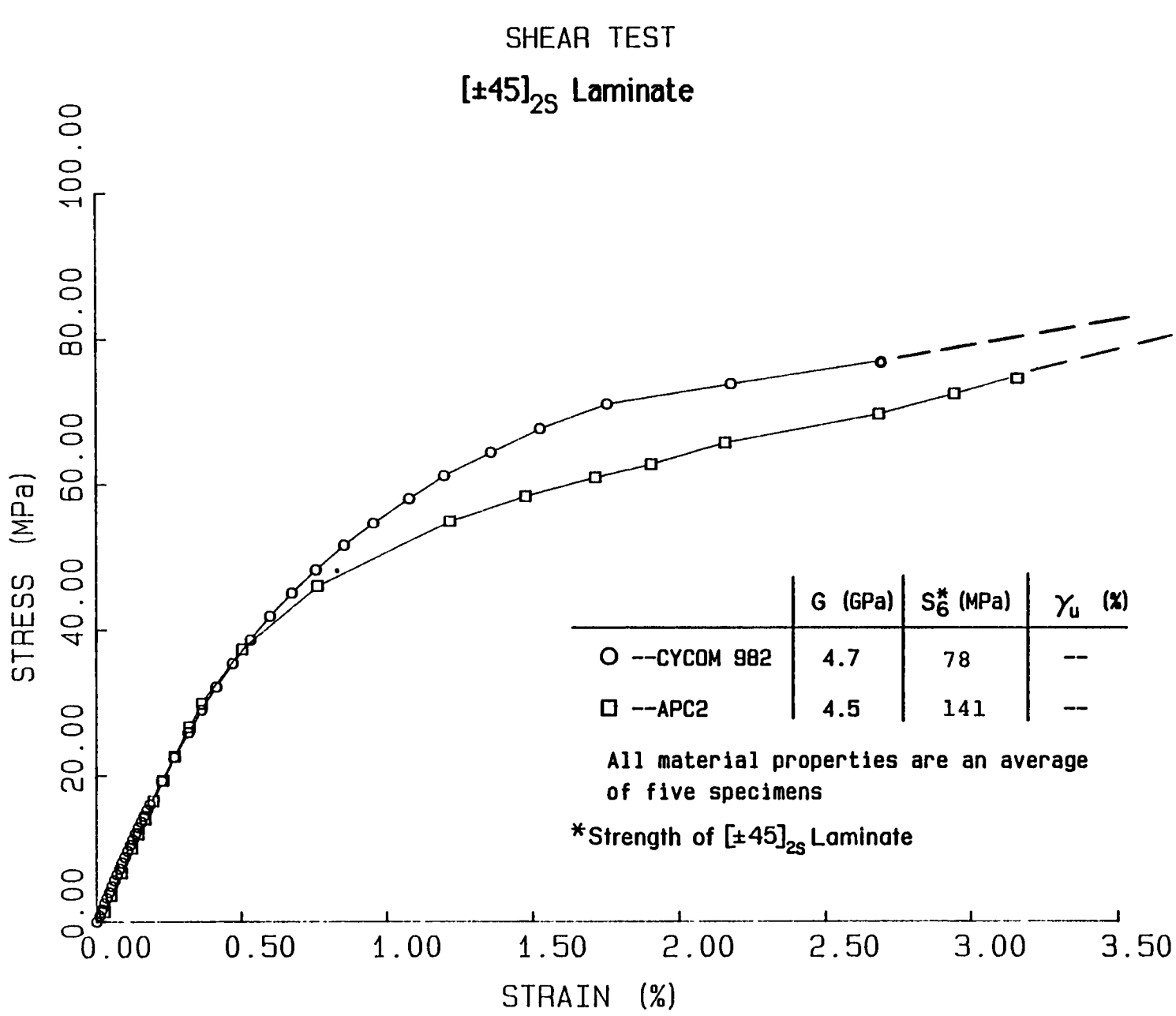
SHEAR TEST
[±45]2S Laminate
STRESS (MPa)
0.00
20.00
40.00
60.00
80.00
100.00
0.00
0.50
1.00
1.50
2.00
2.50
3.00
3.50
STRAIN (%)
G (GPa)
S*6 (MPa)
γu (%)
O --CYCOM 982
4.7
78
--
□ --APC2
4.5
141
--
All material properties are an average of five specimens
*Strength of [±45]2S Laminate

Appendix 7

Interlaminar Fracture Test Data

* Linear load-deflection response

** Non-linear load-deflection response

Mode I: Double Cantilever Beam

CYCOM 982*

$G_{IC}=3A_1A_2^2/2W$**

Nomenclature

$A1[Nm^2]^{-1}$: Coefficient(Compliance vs. Crack Length)
A2[Nm]: Coefficient(Critical load vs. Crack Length
C[m/N]: Initial Compliance
Pc[N]: Critical Load
w[m]: Width

Summary

Instron Cross Head Rate, $\dot{\delta}$ [in/min]	[10^{-6}m/s]	G_{IC} [kj/m^2]
0.05	21	0.26 0.27 0.25 0.23 0.22 0.26
Overall Average		0.25±0.02

* Linear elastic response and stable crack growth

** See Appendix 1

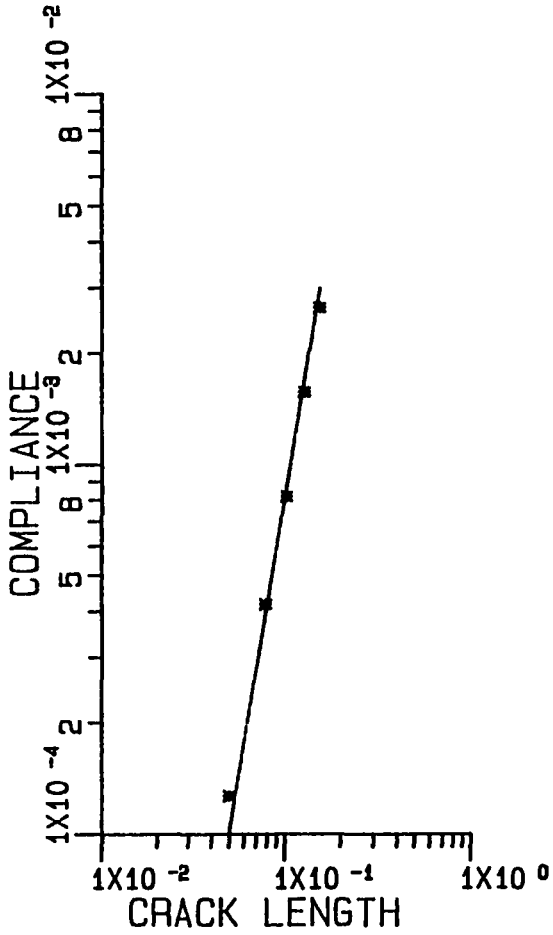

SPECIMEN: CYCOM 982-1

WIDTH= 0.019 (m)

C = 0.80874*A**3 (m/N)

Pc = 2.01212*A**-1 (N)

GIC = 0.26 (KJ/m**2)

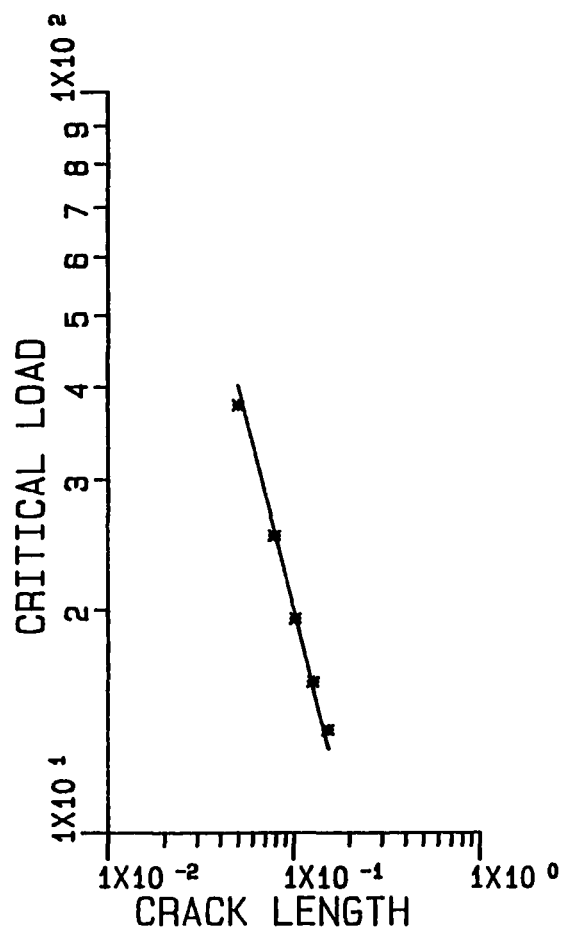

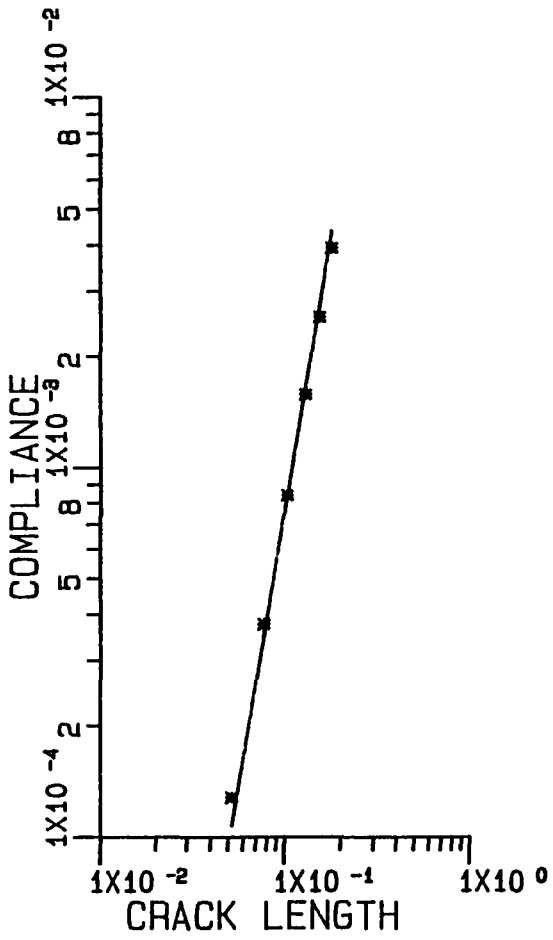

SPECIMEN: CYCOM 982-2

WIDTH= 0.019 (m)

C = 0.74788*A**3 (m/N)

Pc = 2.13270*A**-1 (N)

GIC = 0.27 (KJ/m**2)

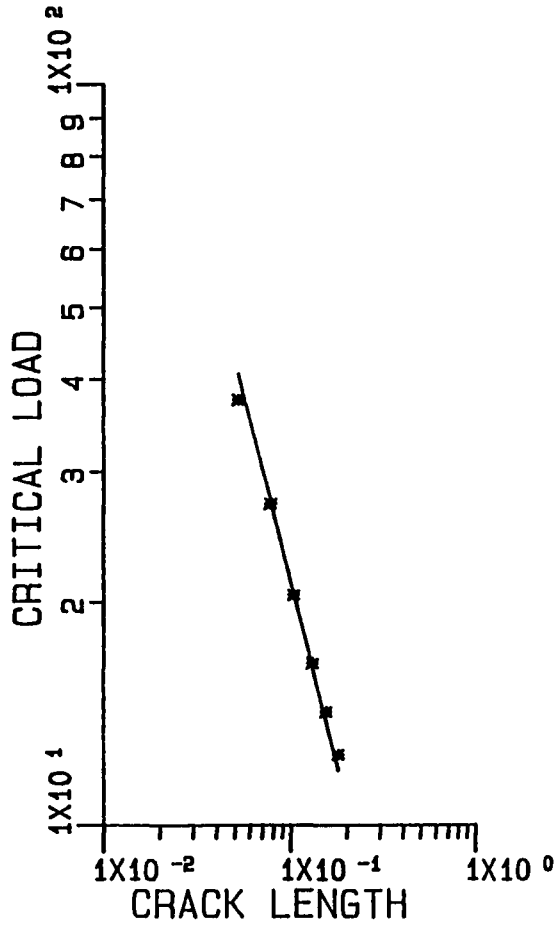

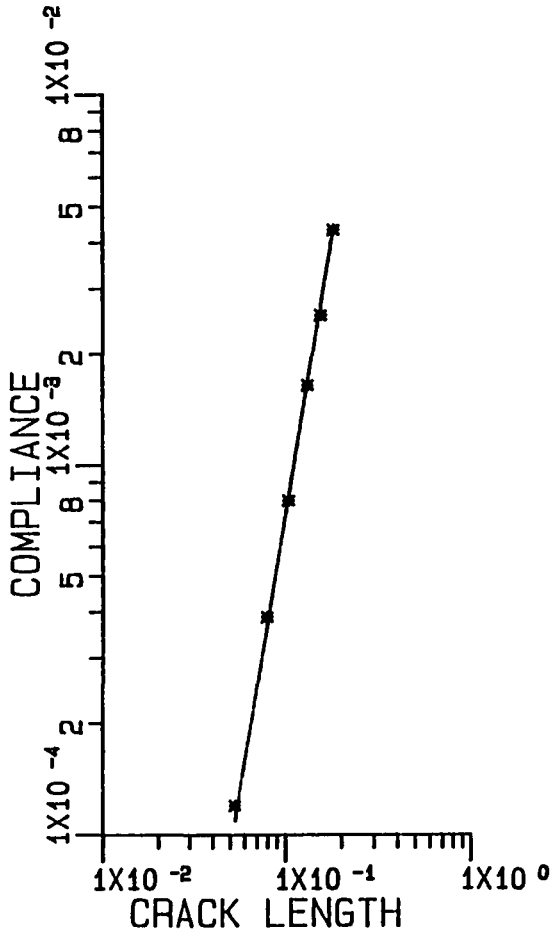

SPECIMEN: CYCOM 982-3

WIDTH= 0.019 (m)

C = 0.72684*A**3 (m/N)

Pc = 2.10707*A**-1 (N)

GIC = 0.25 (KJ/m**2)

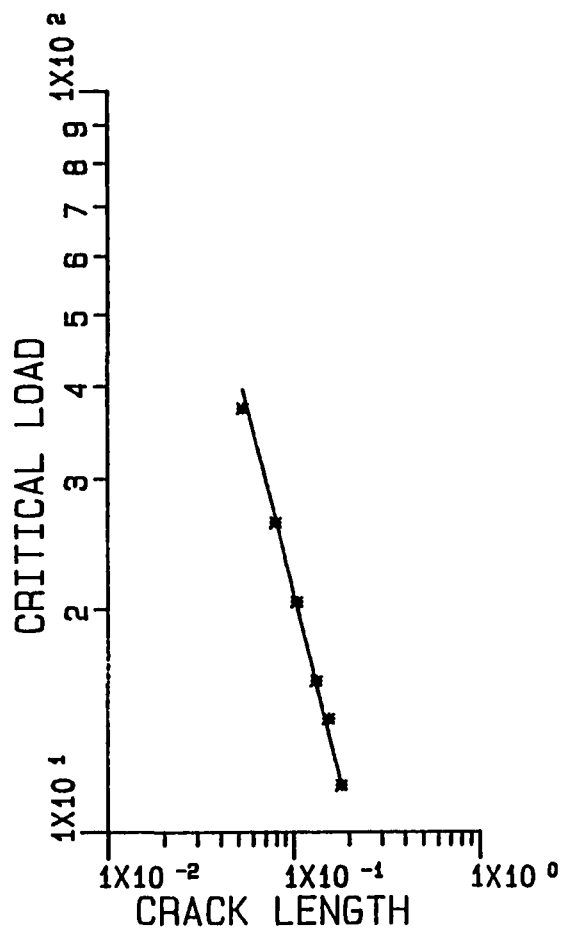

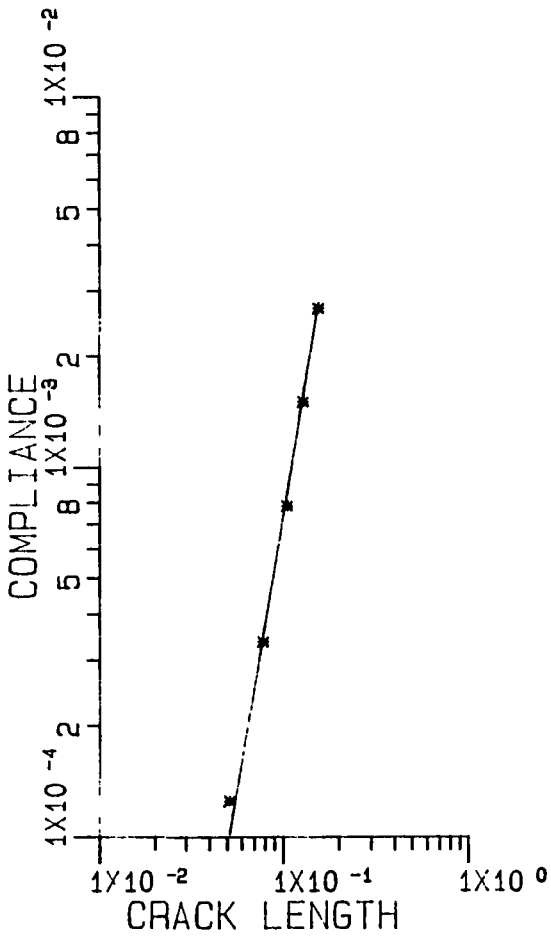

SPECIMEN: CYCOM 982-4

WIDTH= 0.019 (m)

C = 0.74367*A**3 (m/N)

Pc = 1.97113*A**-1 (N)

GIC = 0.23 (KJ/m**2)

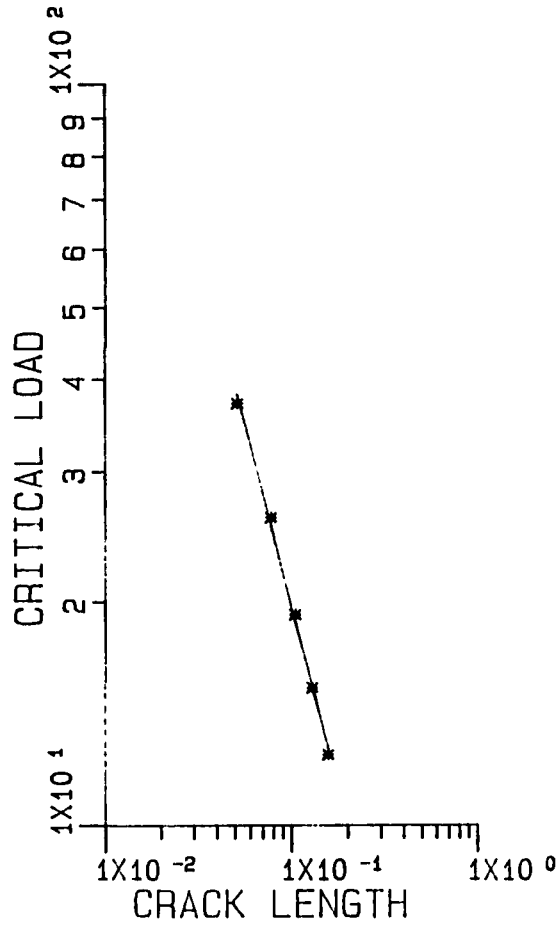

SPECIMEN: CYCOM 982-5

WIDTH= 0.019 (m)

C = 0.70209*A**3 (m/N)

Pc = 1.97580*A**-1 (N)

GIC = 0.22 (KJ/m**2)

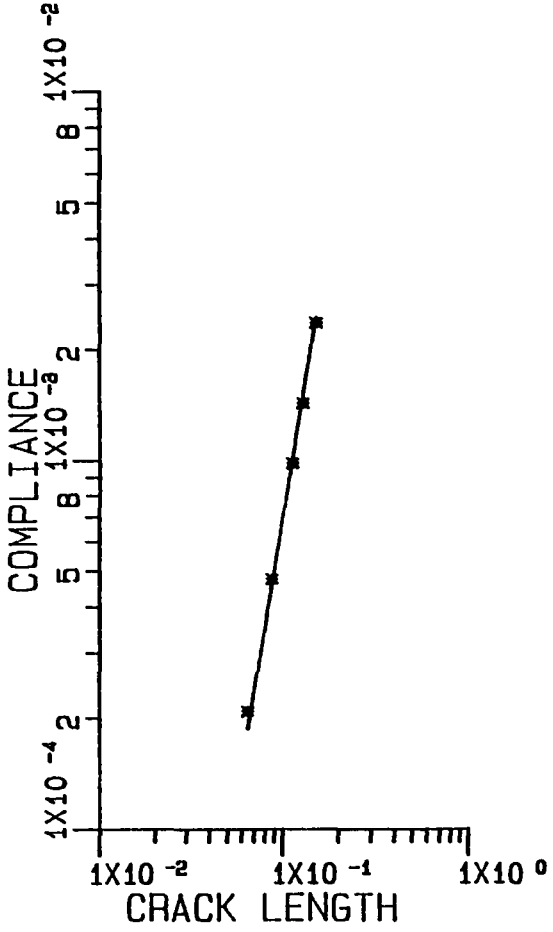

SPECIMEN: CYCOM 9822-6

WIDTH= 0.019 (m)

C = 0.69028*A**3 (m/N)

Pc = 2.17113*A**-1 (N)

GIC = 0.26 (KJ/m**2)

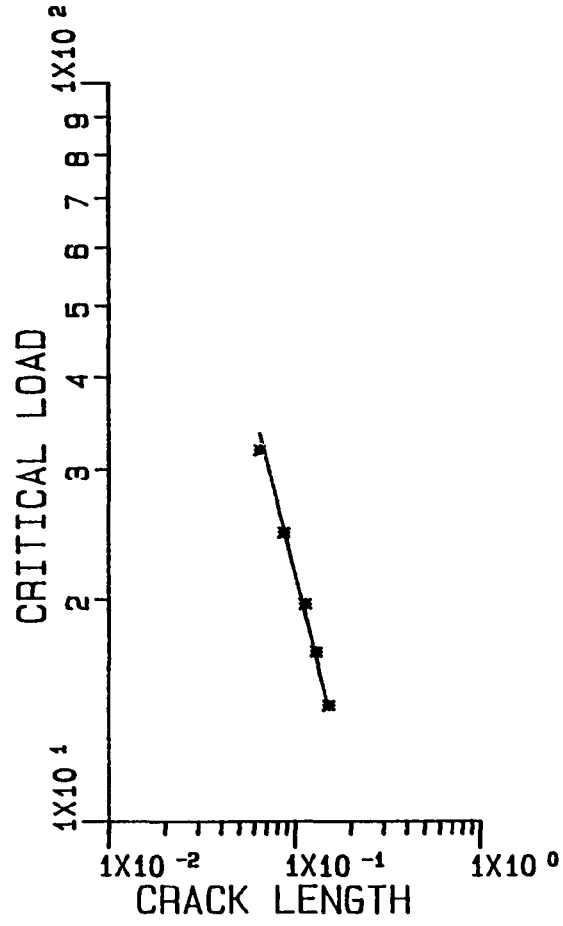

Mode I: Double Cantilever Beam

APC-2 Lower Bound: G_{ISC}

$$G_{ISC}=3A_1P_C^2A^2/2W$$

Nomenclature

A[m]: Crack length

C[m/N]: Initial Compliance

Pc[N]: Load at the onset of Nonlinear response

DR[mm/s]: Instron Crosshead Speed

$G_{IC}[kj/m^2]$: Lower Bound

$Al[Nm^2]^{-1}$: Coefficient

w[m]: Width

Summary: Averaged Results

Instron Cross Head Rate, $\dot{\delta}$ [in/min]	$[10^{-6}m/s]$	Crack Tip Opening* Rate, $\dot{\delta}_I^{CT}$ $[10^{-10}m/s]$	G_{ISC} $[kJ/m^2]$
0.01	4	0.02 - 1.6	1.56±0.05
0.10	42	1 - 10	1.60±0.26
1.00	423	8 - 118	1.41±0.21
10.00	4233	108 - 1102	1.37±0.15
		Overall Average	1.47

* $\dot{\delta}_I^{CT} \equiv \frac{3}{2}\dot{\delta}\left(\frac{t}{a}\right)^2$, t= 2 ply thicknesses

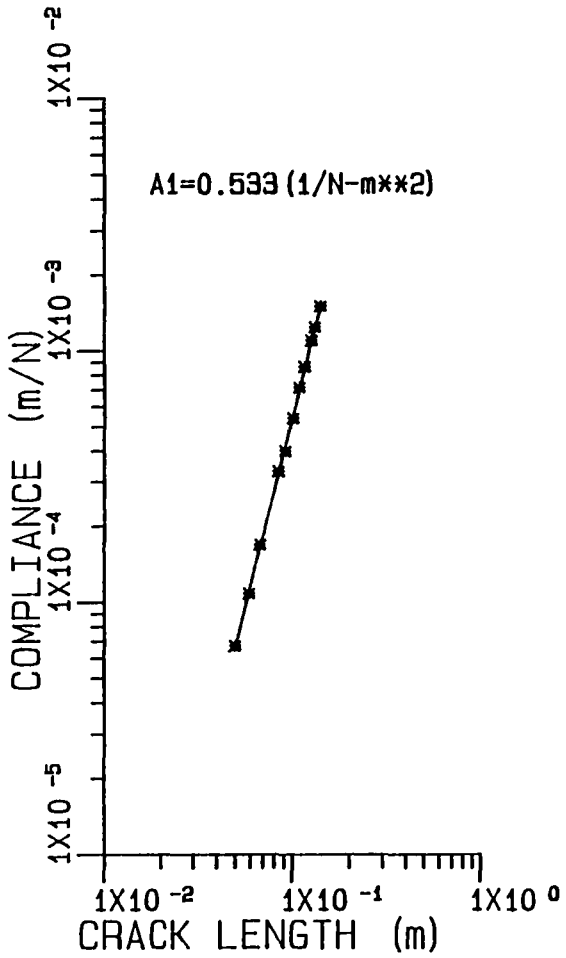

SPECIMEN: APC2-0.01-1

WIDTH= 0.019 (m)

A (m)	C (m/N)	Pc (N)	DR (mm/s)	GIC (KJ/m**2)
0.050	0.00007	122.3	0.004	1.57
0.059	0.00011	104.5	0.004	1.62
0.068	0.00017	87.6	0.004	1.48
0.085	0.00033	70.3	0.004	1.49
0.092	0.00040	65.8	0.004	1.55
0.101	0.00054	60.5	0.004	1.56
0.109	0.00071	56.0	0.004	1.57
0.117	0.00086	52.5	0.004	1.57
0.127	0.00110	48.0	0.004	1.56
0.133	0.00124	46.3	0.004	1.58
0.141	0.00150	44.5	0.004	1.65

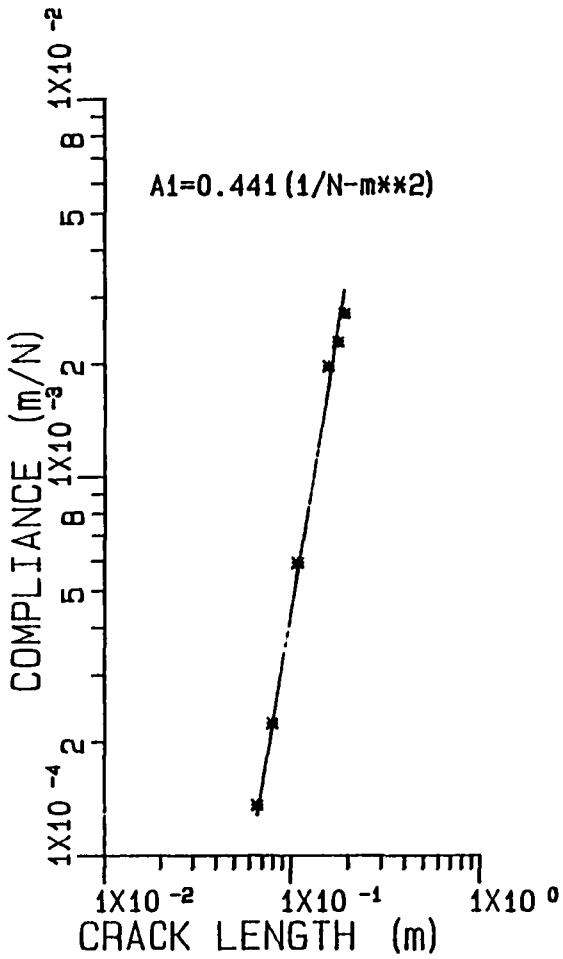

SPECIMEN: APC2-I0.1-1

WIDTH= 0.019 (m)

A (m)	C (m/N)	Pc (N)	DR (mm/s)	GIC (KJ/m**2)
0.066	0.00014	106.8	0.042	1.74
0.080	0.00022	89.0	0.042	1.74
0.109	0.00059	48.9	0.042	0.98
0.158	0.00197	34.7	0.042	1.05
0.179	0.00228	40.0	0.042	1.77
0.192	0.00272	36.5	0.042	1.70

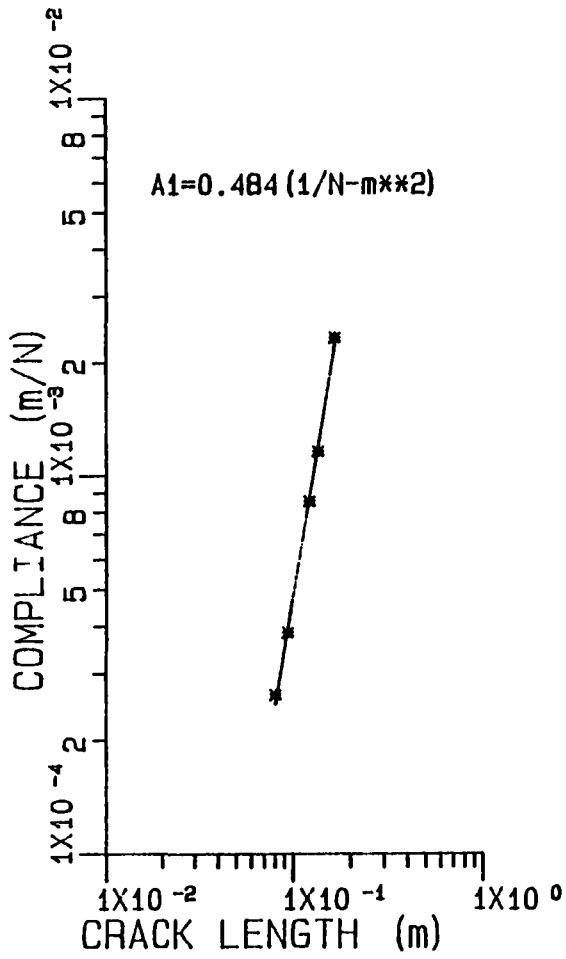

SPECIMEN: APC2-I0.1-2

WIDTH= 0.019 (m)

A (m)	C (m/N)	Pc (N)	DR (mm/s)	GIC (KJ/m**2)
0.080	0.00026	73.0	0.042	1.31
0.094	0.00039	71.2	0.042	1.70
0.122	0.00086	53.4	0.042	1.61
0.136	0.00116	47.2	0.042	1.56
0.167	0.00233	38.3	0.042	1.55

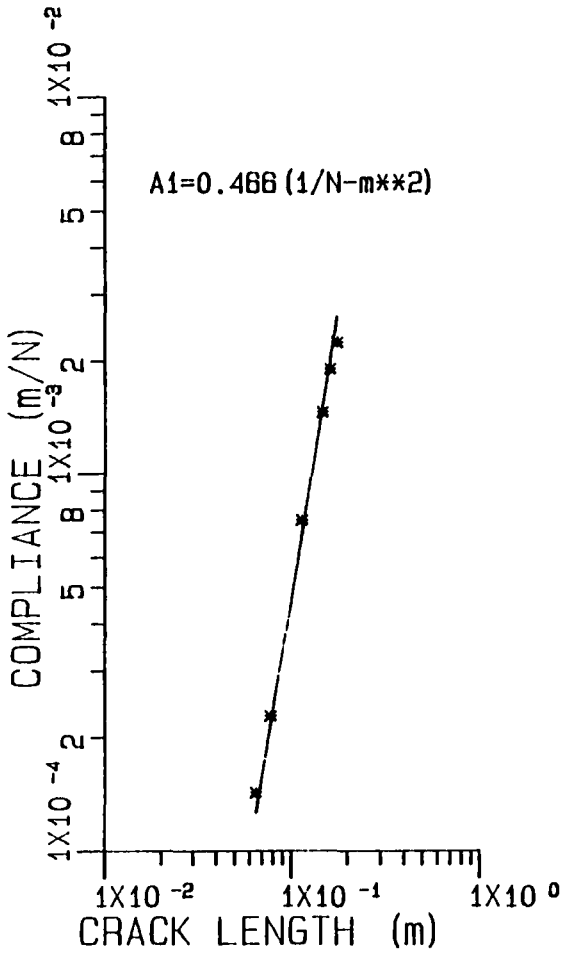

SPECIMEN: APC2-I0.1-3

WIDTH= 0.019 (m)

A (m)	C (m/N)	Pc (N)	DR (mm/s)	GIC (KJ/m**2)
0.065	0.00014	104.5	0.042	1.681
0.078	0.00023	89.0	0.042	1.753
0.114	0.00075	55.6	0.042	1.481
0.148	0.00146	46.7	0.042	1.754
0.163	0.00190	42.7	0.042	1.772
0.178	0.00224	41.4	0.042	1.983

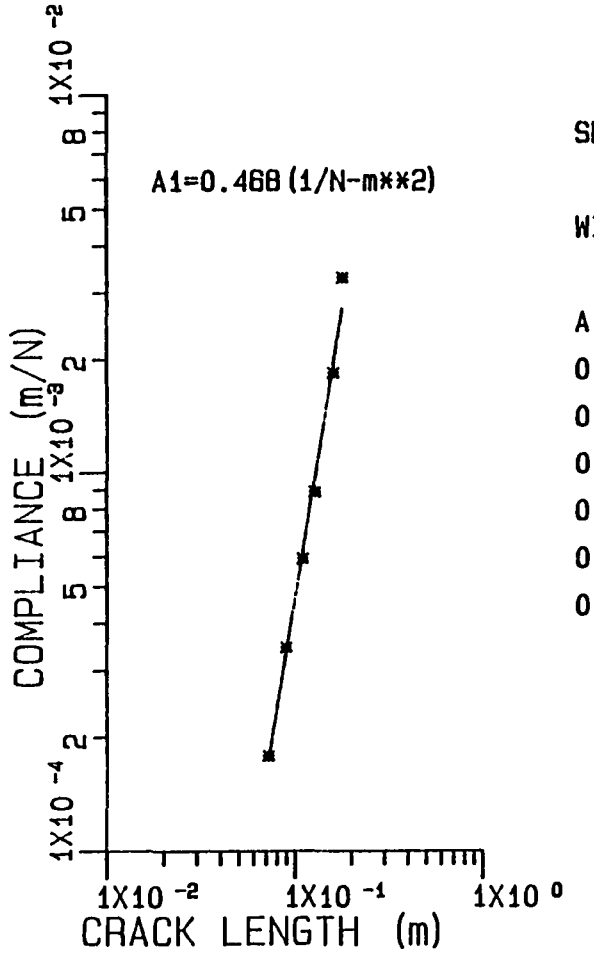

SPECIMEN: APC2-I1-1

WIDTH= 0.019 (m)

A (m)	C (m/N)	Pc (N)	DR (mm/s)	GIC (KJ/m**2)
0.072	0.00018	88.7	0.423	1.44
0.090	0.00035	72.5	0.423	1.57
0.110	0.00059	61.4	0.423	1.69
0.129	0.00089	48.9	0.423	1.46
0.161	0.00184	40.9	0.423	1.60
0.180	0.00329	31.6	0.423	1.19

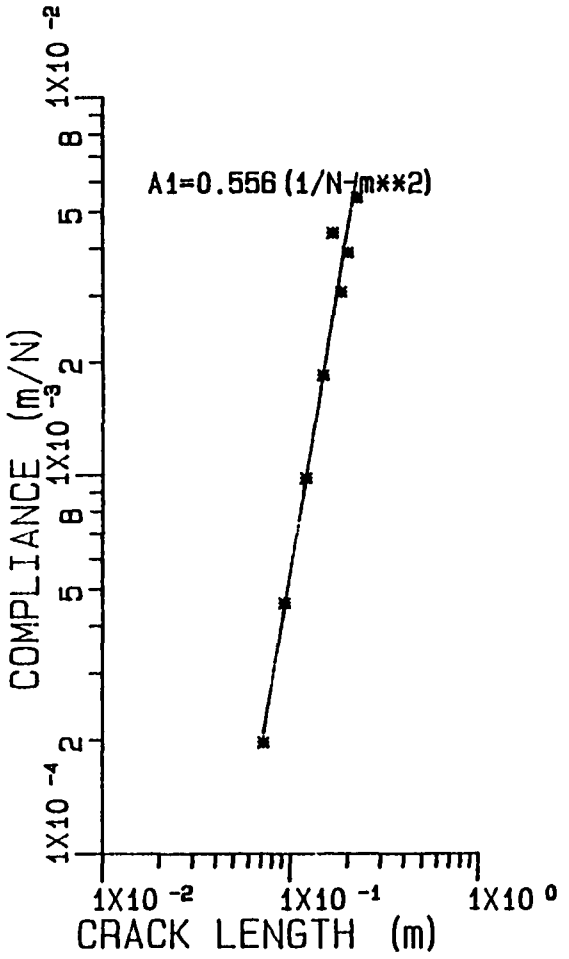

SPECIMEN: APC2-I1-2

WIDTH= 0.019 (m)

A (m)	C (m/N)	Pc (N)	DR (mm/s)	GIC (KJ/m**2)
0.072	0.00020	83.6	0.423	0.92
0.093	0.00046	54.3	0.423	1.12
0.121	0.00098	40.9	0.423	1.08
0.149	0.00184	34.7	0.423	1.18
0.168	0.00439	34.3	0.423	1.46
0.186	0.00306	33.4	0.423	1.68
0.202	0.00389	29.8	0.423	1.58
0.225	0.00544	25.4	0.423	1.42

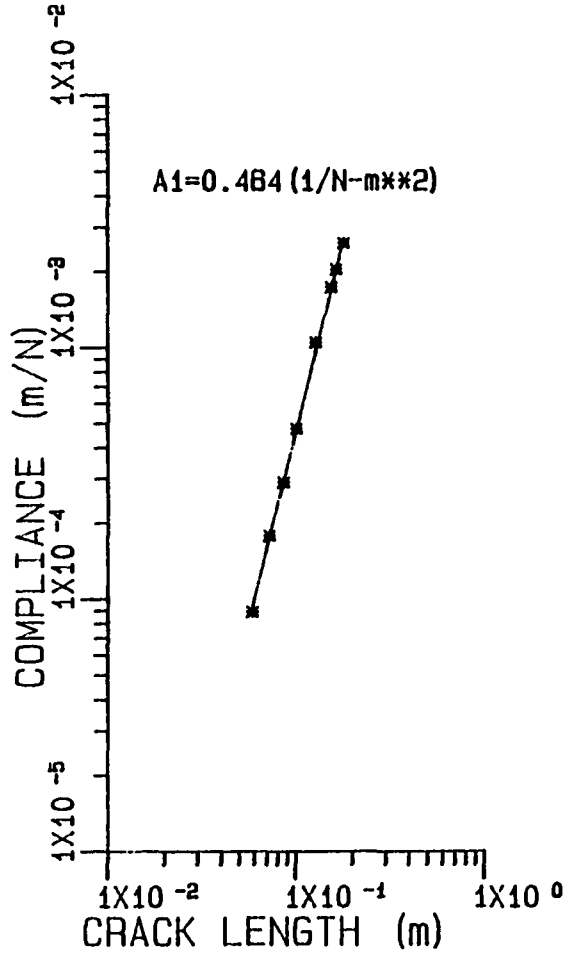

SPECIMEN: APC2-I1-3

WIDTH= 0.019 (m)

A (m)	C (m/N)	Pc (N)	DR (mm/s)	GIC (KJ/m**2)
0.059	0.00009	108.8	0.423	1.43
0.073	0.00018	81.4	0.423	1.28
0.088	0.00029	73.4	0.423	1.45
0.101	0.00048	60.5	0.423	1.37
0.128	0.00104	47.6	0.423	1.35
0.154	0.00173	41.8	0.423	1.51
0.164	0.00204	42.7	0.423	1.78
0.180	0.00259	36.0	0.423	1.53

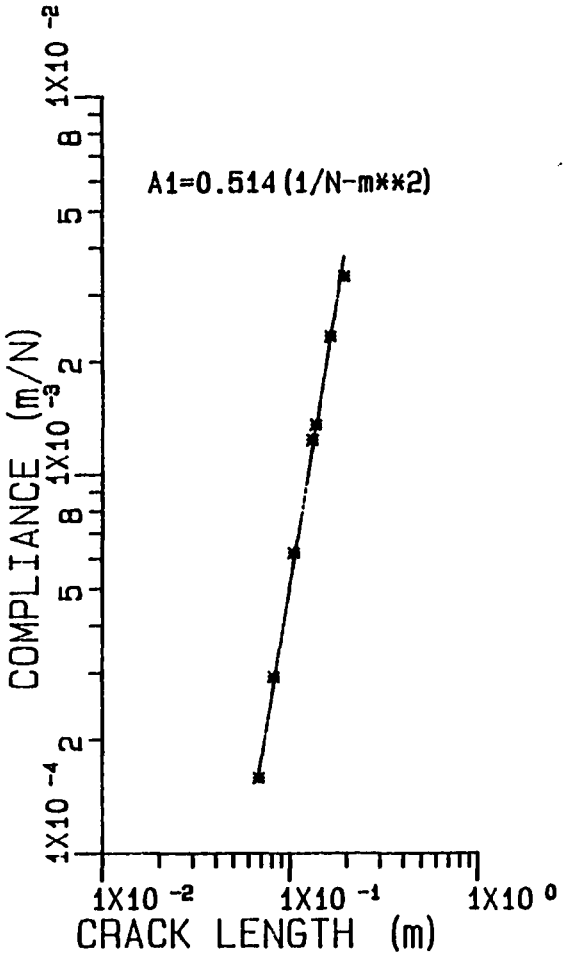

SPECIMEN: APC2-I10-1

WIDTH= 0.019 (m)

A (m)	C (m/N)	Pc (N)	DR (mm/s)	GIC (KJ/m**2)
0.068	0.00016	80.1	4.233	1.21
0.082	0.00029	66.7	4.233	1.21
0.105	0.00062	47.2	4.233	0.99
0.132	0.00124	41.8	4.233	1.23
0.137	0.00136	41.8	4.233	1.33
0.165	0.00233	35.6	4.233	1.40
0.195	0.00336	31.6	4.233	1.53

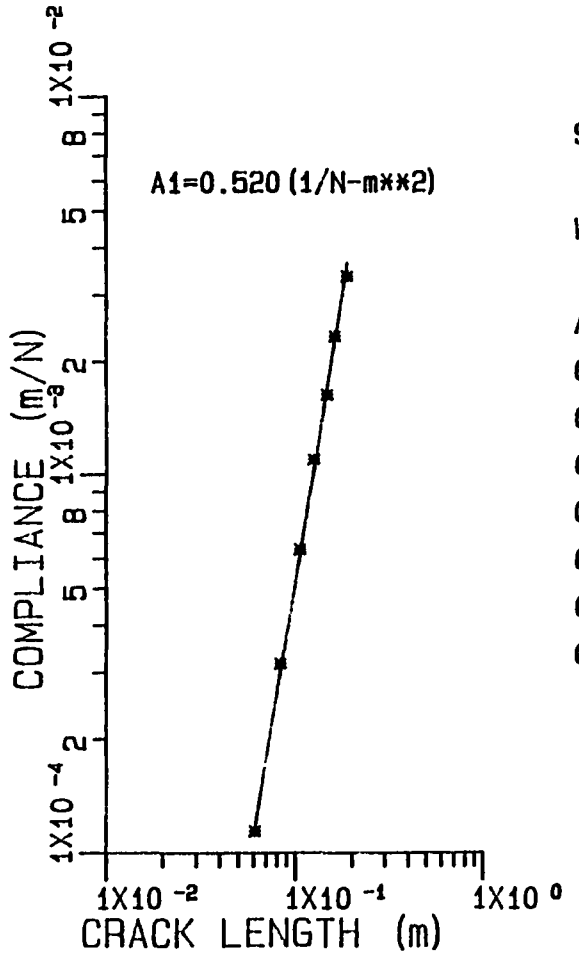

SPECIMEN: APC2-I10-2

WIDTH= 0.019 (m)

A (m)	C (m/N)	Pc (N)	DR (mm/s)	GIC (KJ/m**2)
0.081	0.00011	97.9	4.233	1.45
0.084	0.00032	68.1	4.233	1.33
0.106	0.00063	52.0	4.233	1.26
0.125	0.00110	48.9	4.233	1.54
0.148	0.00163	42.0	4.233	1.59
0.164	0.00233	34.7	4.233	1.32
0.191	0.00336	32.5	4.233	1.58

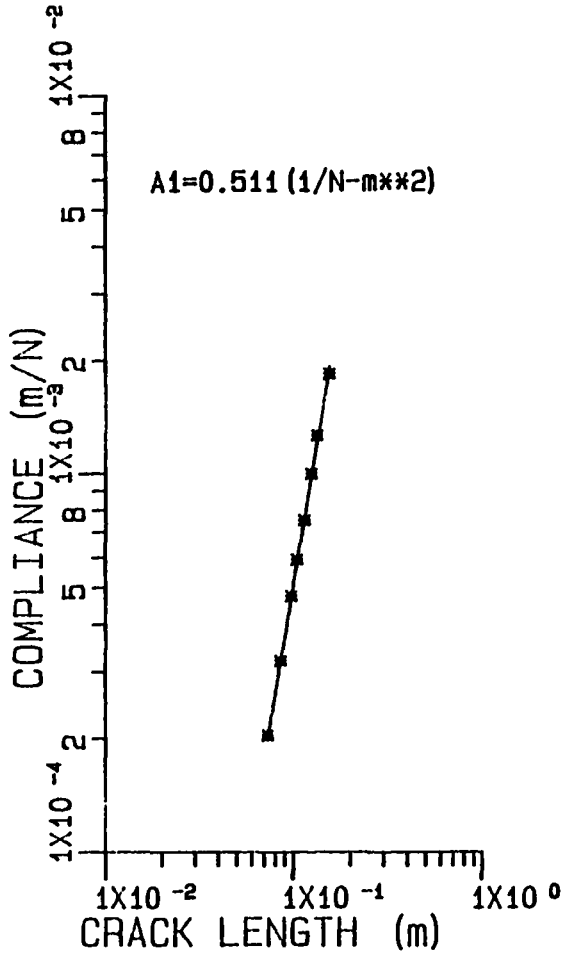

SPECIMEN: APC2-I10-3

WIDTH= 0.019 (m)

A (m)	C (m/N)	Pc (N)	DR (mm/s)	GIC (KJ/m**2)
0.073	0.00020	77.0	4.233	1.28
0.086	0.00032	65.4	4.233	1.27
0.098	0.00048	61.4	4.233	1.44
0.105	0.00059	56.5	4.233	1.41
0.114	0.00075	51.2	4.233	1.38
0.125	0.00100	48.0	4.233	1.44
0.134	0.00127	45.4	4.233	1.49
0.156	0.00184	40.0	4.233	1.56

Mode I: Double Cantilever Beam

APC-2 Intermediate Bound: G_{IC}

$$G_{IC}=3A_1 Pc^2 A^2/2W$$

Nomenclature

A[m]: Crack length

C[m/N]: Initial Compliance

Pc[N]: Maximum load

DR[mm/s]: Instron Cross Head Speed

G_{IC}[kj/m^2]: Intermediate Bound

A_1[Nm^2]$^{-1}$: Coefficient

W[m]: Width

Summary: Averaged Results

Instron Cross Head Rate, $\dot{\delta}$		Crack Tip Opening* Rate, $\dot{\delta}_I^{CT}$	G_{IC}
[in/min]	[10^{-6}m/s]	[10^{-10}m/s]	[kj/m^2]
0.01	4	0.02 - 1.6	1.56±0.05
0.10	42	1 - 10	1.75±0.13
1.00	423	8 - 118	1.98±0.13
10.00	4233	108 - 1102	1.71±0.16
		Overall Average	1.75

*$\dot{\delta}_I^{CT} \equiv \frac{3}{2}\dot{\delta}(\frac{t}{a})^2$, t= 2 ply thicknesses

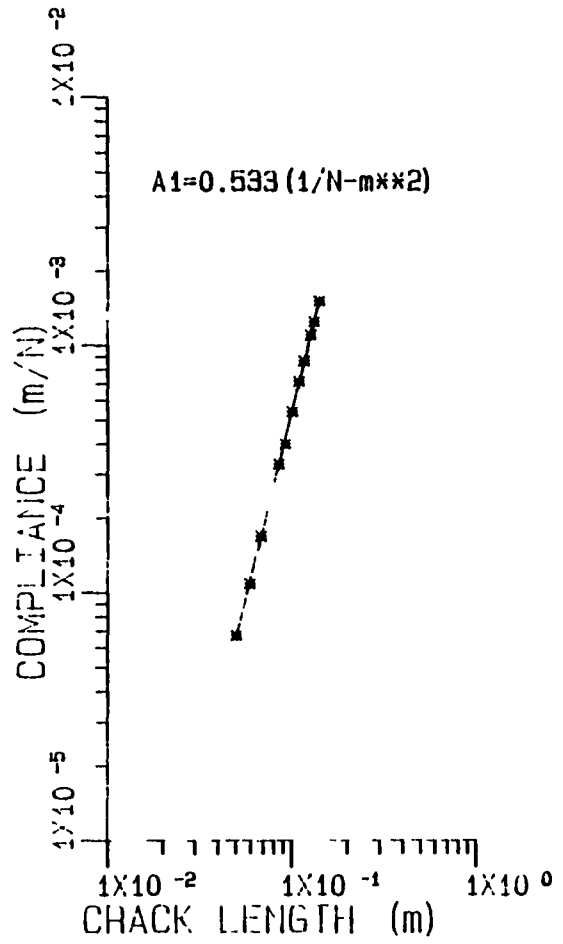

SPECIMEN: APC2-0.01-1

WIDTH= 0.019 (m)

A (m)	C (m/N)	Pc (N)	DR (mm/s)	GIC (KJ/m**2)
0.050	0.00007	122.3	0.004	1.57
0.059	0.00011	104.5	0.004	1.62
0.068	0.00017	87.6	0.004	1.48
0.085	0.00033	70.3	0.004	1.49
0.092	0.00040	65.8	0.004	1.55
0.101	0.00054	60.5	0.004	1.56
0.109	0.00071	56.0	0.004	1.57
0.117	0.00086	52.5	0.004	1.57
0.127	0.00110	48.0	0.004	1.56
0.133	0.00124	46.3	0.004	1.58
0.141	0.00150	44.5	0.004	1.65

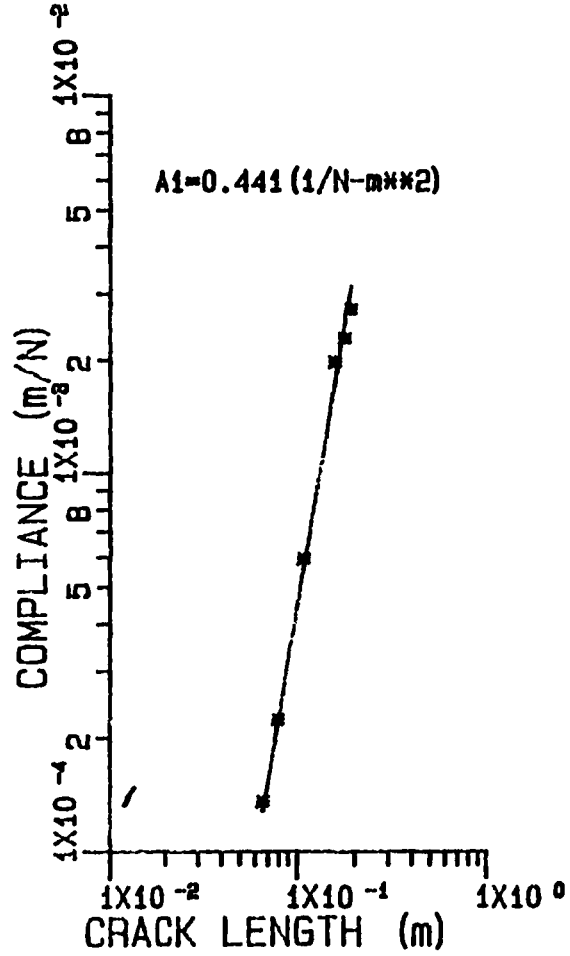

SPECIMEN: APC2-I0.1-1U

WIDTH= 0.018 (m)

A (m)	C (m/N)	Pc (N)	DR (mm/s)	GIC (KJ/m**2)
0.088	0.00014	108.8	0.042	1.739
0.080	0.00022	88.0	0.042	1.737
0.108	0.00058	61.8	0.000	1.568
0.158	0.00197	41.8	0.042	1.520
0.179	0.00228	40.5	0.042	1.814
0.192	0.00272	37.4	0.042	1.787

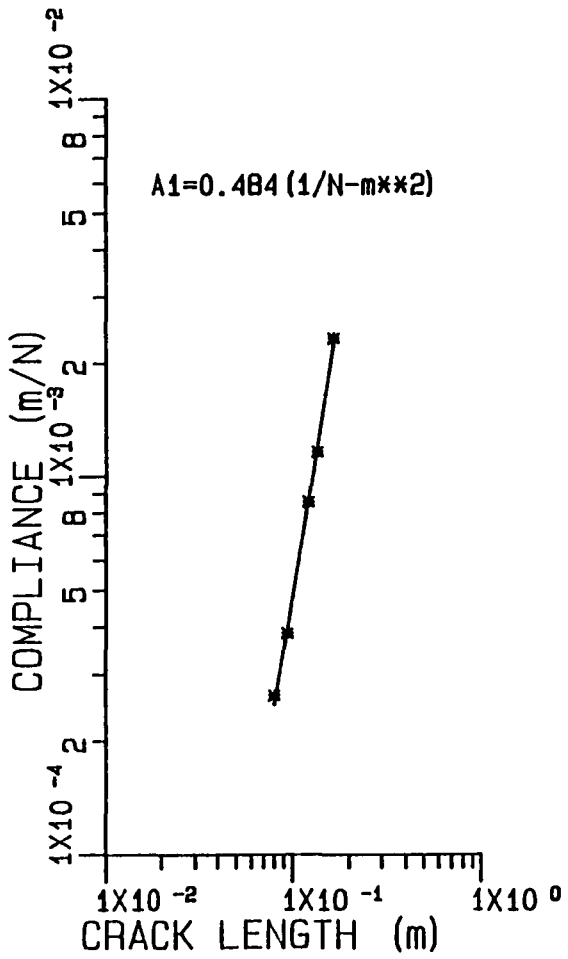

SPECIMEN: APC2-I0.1-2U

WIDTH= 0.019 (m)

A (m)	C (m/N)	Pc (N)	DR (mm/s)	GIC (KJ/m**2)
0.080	0.00026	83.6	0.042	1.718
0.094	0.00039	73.4	0.042	1.804
0.122	0.00086	54.3	0.042	1.669
0.136	0.00116	48.5	0.042	1.649
0.167	0.00233	40.9	0.042	1.773

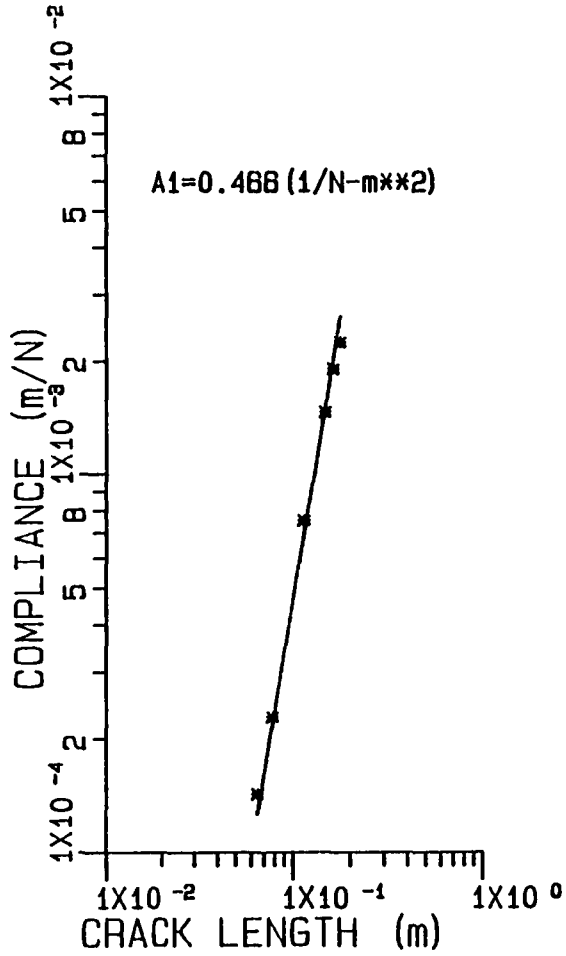

SPECIMEN: APC2-I0.1-3U

WIDTH= 0.019 (m)

A (m)	C (m/N)	Pc (N)	DR (mm/s)	GIC (KJ/m**2)
0.065	0.00014	104.5	0.042	1.681
0.078	0.00023	89.0	0.042	1.753
0.114	0.00075	59.6	0.042	1.702
0.148	0.00146	48.9	0.042	1.925
0.163	0.00190	43.1	0.042	1.809
0.178	0.00224	41.8	0.042	2.026

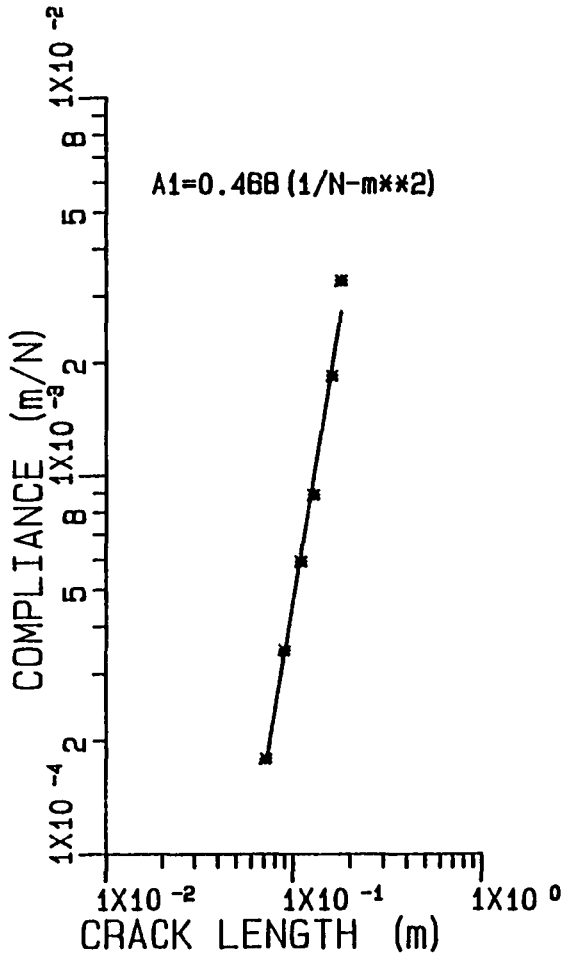

SPECIMEN: APC2-I1-1U

WIDTH= 0.019 (m)

A (m)	C (m/N)	Pc (N)	DR (mm/s)	GIC (KJ/m**2)
0.072	0.00018	105.4	0.423	2.130
0.090	0.00035	86.7	0.423	2.253
0.110	0.00059	71.6	0.423	2.295
0.129	0.00089	66.3	0.423	2.672
0.161	0.00184	53.8	0.423	2.766
0.180	0.00329	38.3	0.423	1.743

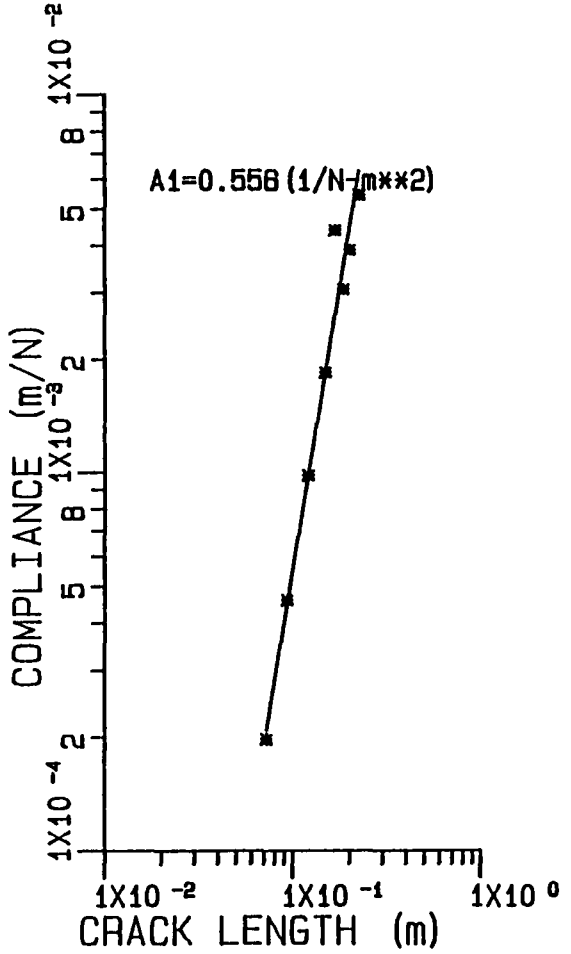

SPECIMEN: APC2-I1-2U

WIDTH= 0.019 (m)

A (m)	C (m/N)	Pc (N)	DR (mm/s)	GIC (KJ/m**2)
0.072	0.00020	81.0	0.423	1.493
0.093	0.00048	67.2	0.423	1.716
0.121	0.00098	51.2	0.423	1.682
0.149	0.00184	43.8	0.423	1.856
0.168	0.00439	41.4	0.423	2.125
0.186	0.00306	38.5	0.423	2.008
0.202	0.00389	33.4	0.423	1.982
0.225	0.00544	28.0	0.423	1.734

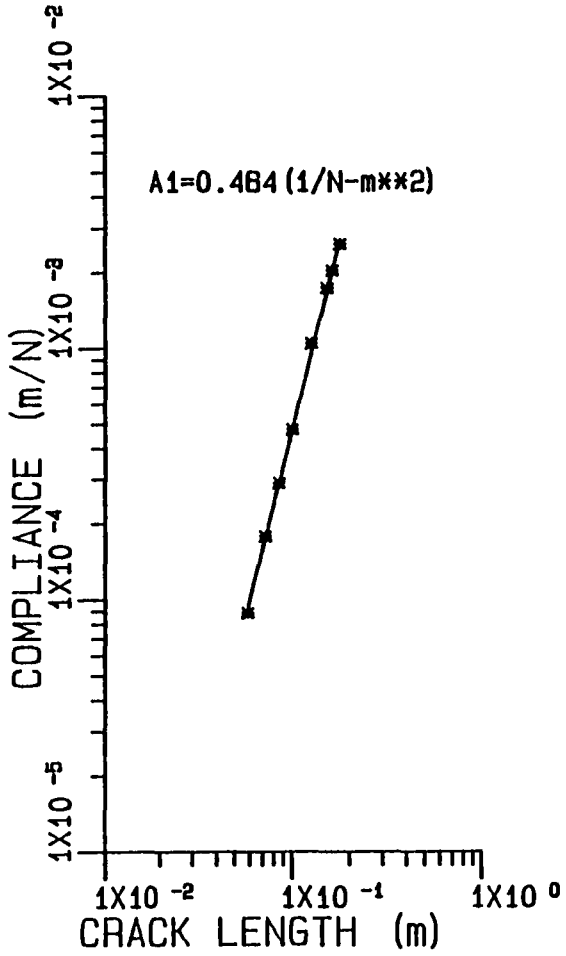

SPECIMEN: APC2-I1-3U

WIDTH= 0.019 (m)

A (m)	C (m/N)	Pc (N)	DR (mm/s)	GIC (KJ/m**2)
0.059	0.00009	120.5	0.423	1.827
0.073	0.00018	94.7	0.423	1.730
0.086	0.00029	81.8	0.423	1.803
0.101	0.00048	71.2	0.423	1.891
0.128	0.00104	60.1	0.423	2.150
0.154	0.00173	44.9	0.423	1.747
0.164	0.00204	43.1	0.423	1.819
0.180	0.00259	42.3	0.423	2.109

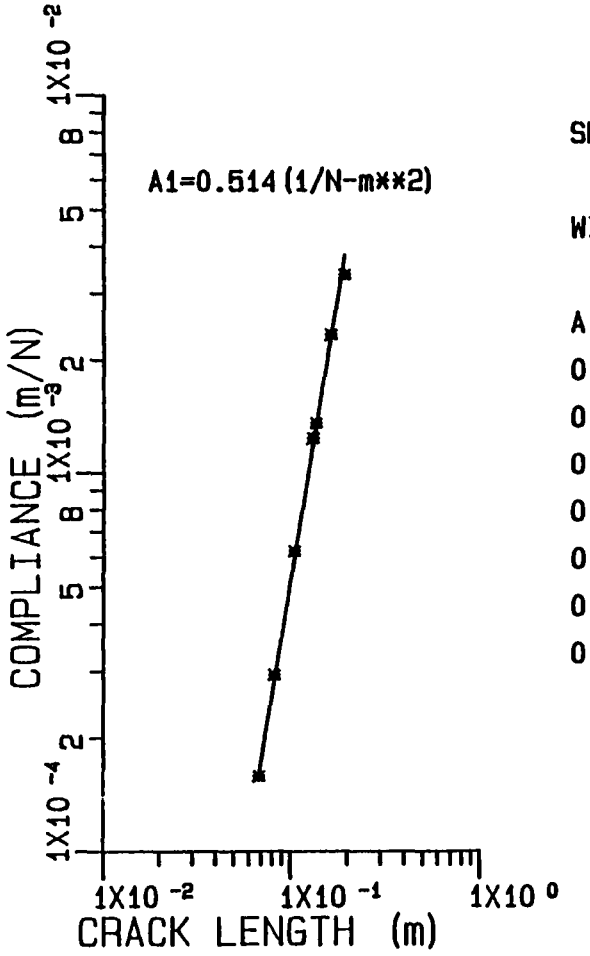

SPECIMEN: APC2-I10-1U

WIDTH= 0.019 (m)

A (m)	C (m/N)	Pc (N)	DR (mm/s)	GIC (KJ/m**2)
0.068	0.00016	89.0	4.233	1.494
0.082	0.00029	76.7	4.233	1.602
0.105	0.00062	62.3	4.233	1.734
0.132	0.00124	41.8	4.233	1.229
0.137	0.00136	45.4	4.233	1.572
0.165	0.00233	39.1	4.233	1.689
0.195	0.00338	31.8	4.233	1.527

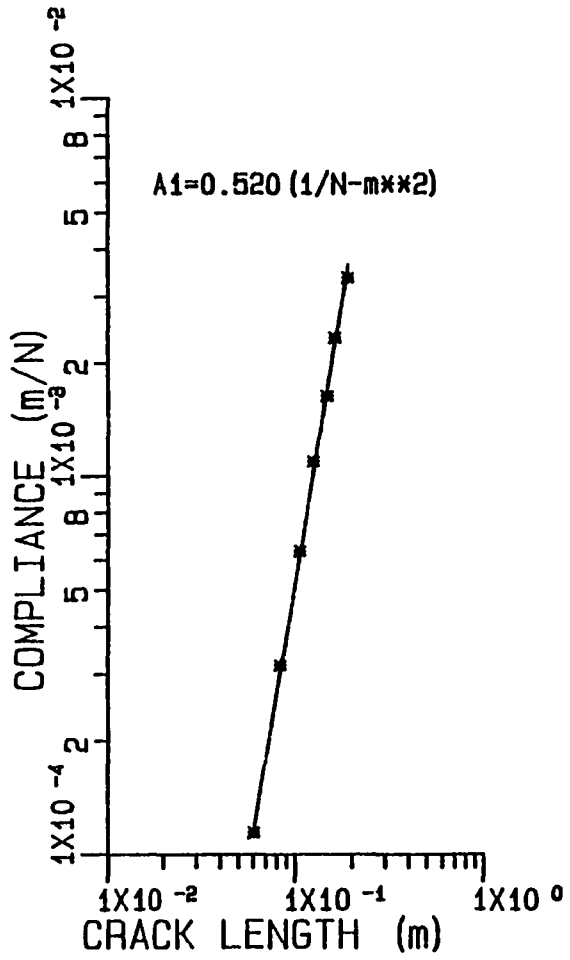

SPECIMEN: APC2-10-2U

WIDTH= 0.019 (m)

A (m)	C (m/N)	Pc (N)	DR (mm/s)	GIC (KJ/m**2)
0.081	0.00011	97.9	4.233	1.445
0.084	0.00032	77.8	4.233	1.743
0.108	0.00063	80.9	4.233	1.722
0.125	0.00110	52.5	4.233	1.776
0.148	0.00163	43.6	4.233	1.712
0.164	0.00233	41.8	4.233	1.916
0.191	0.00336	36.0	4.233	1.939

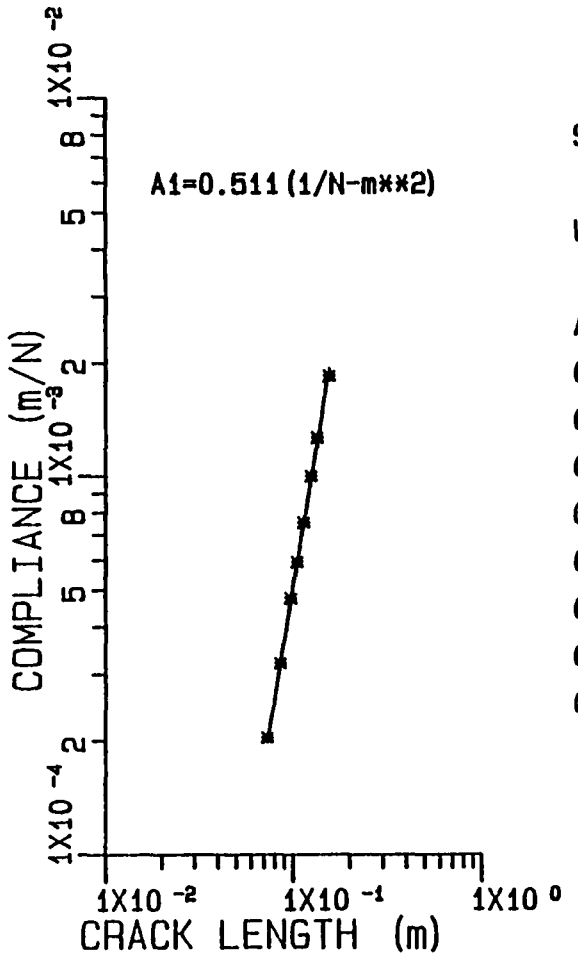

SPECIMEN: APC2-I10-2U

WIDTH= 0.019 (m)

A (m)	C (m/N)	Pc (N)	DR (mm/s)	GIC (KJ/m**2)
0.073	0.00020	89.0	4.233	1.704
0.088	0.00032	75.8	4.233	1.696
0.098	0.00048	61.4	4.233	1.443
0.105	0.00059	58.3	4.233	1.504
0.114	0.00075	56.5	4.233	1.678
0.125	0.00100	48.9	4.233	1.498
0.134	0.00127	51.2	4.233	1.894
0.156	0.00184	46.3	4.233	2.088

Mode II: End Notched Flexure

CYCOM 982*

$$G_{IIC}^{BT} = \frac{9a^2Pc^2C}{2w(2L^3+3a^3)}$$

Nomencluture

a[m]:	crack length	Pc[N]:	Maxıum Load
L[m]:	Half Span	C[m/N]:	Initial Compliance
W[m]:	width ($2.55\pm0.01\times10^{-2}$m)	t[m]:	Thickness ($3.51\pm0.03\times10^{-3}$m)

Summary **

Precrack	Half Span [m]	G_{II}^{BT} [kj/m^2]	G_{II}^{FE}*** [kj/m^2]
No Precrack	0.051	1.45±0.16	1.85+0.20
Mode I	0.051	0.68±0.02	0.87±0.03
Mode II	0.051	0.77±0.07	0.98±0.09
Mode II	0.038	0.68±0.11	0.94±0.15
No Precrack	0.038	1.40±0.18	1.93±0.25

* Linear load deflection response

** Instron Rate: 21×10^{-6}m/s [0.05 in/min]

*** See Tables 15 and 17 for Material 3 (E_1/G_{13}=25.7)

Mode II: End Notched Flexure

CYCOM 982

No Precrack

Sample	L [m]	$\frac{a}{L}$	C [10^{-6} m/N]	Pc [N]	G^{BT}_{IIC} [kj/m^2]
C4	0.051	0.52	2.53	1268	1.59
C6	0.051	0.51	2.46	1321	1.63
C7	0.051	0.51	2.41	1201	1.29
C9	0.051	0.50	2.36	1357	1.59
C11	0.051	0.51	2.42	1334	1.63
C18	0.051	0.51	2.01	1277	1.23
C20	0.051	0.50	2.51	1237	1.41
C28	0.051	0.51	2.45	1201	1.31
C1	0.038	0.37	0.93	2002	1.10
C2	0.038	0.37	0.96	2037	1.31
C17	0.038	0.36	0.96	2171	1.28
C5	0.038	0.57	1.18	1503	1.56
C23	0.038	0.54	1.16	1557	1.52
C3	0.038	0.69	1.41	1179	1.45
C8	0.038	0.68	1.41	1277	1.67
C26	0.038	0.68	1.37	1179	1.39

Mode II: End Notched Flexure

CYCOM 982

Mode I Precrack

Sample	L [m]	$\frac{a}{L}$	C [10^{-6}m/N]	Pc [N]	G_{IIC}^{BT} [kJ/m^2]
C-2-12	0.051	0.55	2.59	801	0.71
C-2-15	0.051	0.57	2.66	765	0.69
C-2-16	0.051	0.54	2.67	792	0.69
C-2-17	0.051	0.56	2.81	743	0.67

Mode II Precrack

C-2-2	0.051	0.64	2.85	725	0.75
C-2-18	0.051	0.60	2.66	796	0.79
C-2-32	0.051	0.58	2.66	783	0.75
C-2-31	0.051	0.58	2.57	801	0.74
C-2-21	0.051	0.51	2.48	863	0.69
C-2-13	0.051	0.59	2.45	863	0.86
C-2-11	0.051	0.78	3.19	667	0.88
C-2-10	0.051	0.79	3.62	609	0.84
C-2-14	0.051	0.87	3.79	560	0.78

Mode II: End Notched Flexure

CYCOM 982

Mode II Precrack

Sample	L [m]	$\frac{a}{L}$	C [10^{-6} m/N]	Pc [w]	G_{IIC}^{BT} [kj/m^2]
C-2-3	0.038	0.54	1.04	1076	0.65
C-2-5	0.038	0.44	0.97	1348	0.70
C-2-7	0.038	0.44	0.97	1414	0.78
C-2-29	0.038	0.42	1.01	1334	0.65
C-2-25	0.038	0.45	1.04	1099	0.51
C-2-26	0.038	0.54	1.12	1054	0.69
C-2-27	0.038	0.47	1.27	947	0.51
C-2-28	0.038	0.62	1.28	899	0.68
C-2-30	0.038	0.70	1.38	899	0.83
C-2-1	0.038	0.57	1.50	810	0.58
C-2-6	0.038	0.82	1.80	681	0.71
C-2-20	0.038	0.82	1.53	752	0.73
C-2-24	0.038	0.87	1.66	729	0.78

Mode II: End Notched Flexure

APC-2*

$$G_{IIC}^{BT} = \frac{9a^2Pc^2C}{2w(2L^3+3a^3)}$$

Nomencluture

a[m]:	Crack length	Pc[N]:	Maxium Load
L[m]:	Half Span	C[m/N]:	Initial Compliance
W[m]:	Width**	t[m]:	Thickness**

Summary ***

Precrack	Number of Plies	Half Span [m]	G_{IIC}^{BT} [kj/m^2]
No Precrack	26	0.051	2.73±0.33
Mode I	26	0.051	1.78±0.11
Mode I	40	0.051	1.87±0.11
Mode II	26	0.051	1.93±0.28
Mode I	26	0.038	1.89±0.16
Mode I	40	0.038	1.84±0.07

* Non-linear load deflection response

** Average width: $2.54\pm0.01\times10^{-2}$m
Average Thickness: $3.37\pm0.02\times10^{-3}$m (26 ply);
$5.26\pm0.05\times10^{-3}$m (40 ply)

*** Instron Rate: 21×10^{-6}m/s [0.05 in/min]

Mode II: End Notched Flexure

APC-2

No Precrack (26 plies)

Sample	L [m]	$\frac{a}{L}$	C [10^{-6}m/N]	Pc [N]	G_{IIC}^{BT} [kj/m^2]
A-2-24	0.051	0.49	3.21	1546	2.72
A-2-2	0.051	0.50	3.47	1368	2.39
A-2-8	0.051	0.49	2.91	1724	3.07

Mode I Precrack (26 plies)

A-2-4	0.051	0.53	3.89	1079	1.80
A-2-1	0.051	0.52	3.56	1112	1.70
A-2-20	0.051	0.52	2.81	1257	1.74
A-2-14	0.051	0.51	3.02	1212	1.66
A-2-13	0.051	0.50	2.78	1301	1.72
A-1-5	0.051	0.52	2.64	1303	1.76
A-1-17	0.051	0.53	3.02	1268	1.93
A-1-11	0.051	0.53	2.57	1535	2.01
A-1-3	0.051	0.51	2.57	1303	1.68
A-1-21	0.051	0.53	2.92	1201	1.67
A-1-15	0.051	0.51	2.62	1414	1.99

Mode II: End Notched Flexure

APC-2

Mode I Precrack (40 plies)

Sample	L [m]	$\frac{a}{L}$	C [10^{-6} m/N]	Pc [N]	G^{BT}_{IIC} [kj/m^2]
A-3-1	0.051	0.50	0.73	2630	1.86
A-3-2	0.051	0.52	0.67	2624	1.82
A-3-3	0.051	0.54	0.69	2489	1.84
A-3-4	0.051	0.53	0.71	2530	1.80
A-3-5	0.051	0.52	0.67	2677	1.86
A-3-6	0.051	0.53	0.77	2694	2.26
A-3-7	0.051	0.52	0.83	2483	2.01
A-3-8	0.051	0.50	0.74	2618	1.86
A-3-9	0.051	0.50	0.73	2778	2.08
A-3-10	0.051	0.50	0.76	2542	1.87
A-3-11	0.051	0.51	0.76	2483	1.77
Mode II Precrack (26 plies)					
A-2-5	0.051	0.51	4.78	1012	1.81
A-2-9	0.051	0.49	2.77	1546	2.35
A-2-18	0.051	0.52	3.07	1268	1.95

Mode II: End Notched Flexure

APC-2

Mode I Precrack (26 plies)

Sample	L	$\frac{a}{L}$	C $[10^{-6}m/N]$	Pc [N]	G_{IIC}^{BT} $[kj/m^2]$
A-1-6	0.038	0.68	1.36	1312	1.69
A-1-8	0.038	0.66	1.35	1410	1.88
A-1-7	0.038	0.68	1.30	1423	1.94
A-1-12	0.038	0.65	1.35	1414	1.86
A-1-24	0.038	0.53	1.09	1801	1.96
A-1-19	0.038	0.52	1.03	1890	1.88
A-1-20	0.038	0.51	1.16	1922	2.15
A-1-22	0.038	0.48	1.12	1926	1.90
A-1-23	0.038	0.52	1.26	1766	2.05
A-1-2	0.038	0.32	0.95	2847	1.83
A-1-9	0.038	0.34	1.00	3069	2.08
A-1-1	0.038	0.35	0.96	2433	1.56

Mode I Precrack (40 plies)

A-3-12	0.038	0.54	0.32	3203	1.79
A-3-13	0.038	0.51	0.32	3410	1.86
A-3-14	0.038	0.58	0.34	3114	1.98
A-3-15	0.038	0.51	0.31	3380	1.79
A-3-16	0.038	0.56	0.33	3084	1.77

Mode II: End Notched Flexure

APC-2 Rate Dependence*

$$G_{IISC}^{BT} = \frac{9a^2 P_{NL}^2 C}{2w(2L^3+a^3)} \qquad G_{II}^{BT} = \frac{9a^2 Pc^2 C}{2w(2L^3+3a^3)}$$

Nomenclature

a[m]:	Crack Length	Pc[N]:	Maximum Load
L[m]:	Half Span (0.051m)	P_{NL}[N]:	Load at the onset on nonlinear response
w[m]:	Width (2.54 ± 0.010^{-2})		
t[m]:	Thickness ($3.37\ 0.02\times10^{-3}$m)	C[m/N]:	Initial compliance

Averaged Results

Mode II Rate Dependence: APC2*

Averaged Results

Instron Cross Head Rate, $\dot{\delta}$ [in/min]	[10^{-6}m/s]	Crack Tip Shear Rate, $\dot{\delta}_{II}^{CT}$ [10^{-10}m/s]	G_{IISC}^{BT}	G_{IIC}^{BT} [kj/m^2]
0.01	4	26	0.95± 0.18	1.84± 0.27
0.05	21	130	1.02± 0.20	1.73± 0.20
0.10	42	260	1.01± 0.09	1.82± 0.20
1.00	423	2500	0.98± 0.16	1.87± 0.24
10.00	4233	25000	1.40± 0.13	1.40± 0.13
		Overall Average	1.31	1.73

* Mode I Precrack unless noted otherwise

** $\dot{\delta}_{II}^{CT} \equiv \frac{\dot{\delta}\ (h/L)^3}{1+\frac{3}{2}(\frac{a}{L})^3}\ (\frac{E_1}{G_{13}})$

Mode II Rate Dependence: APC-2

Sample	$\frac{a}{L}$	C $[10^{-6}m/N]$	PnL [N]	PC [N]	G_{IISC}^{BT} $[kj/m^2]$	G_{IIC}^{BT} $[kj/m^2]$
Instron Cross Head Rate: $4x10^{-6}$m/s [0.01 in/min]						
EP-.01-1	0.52	2.63	956	1303	0.91	1.72
EP-.01-2	0.56	2.72	801	1130	0.75	1.49
EP-.01-3	0.52	2.84	1001	1334	1.10	1.95
EP-.01-4	0.47	2.02	1045	1619	0.74	1.77
EP-.01-5	0.51	3.45	1001	1312	1.29	2.22
Instron Cross Head Rate: $42x10^{-6}$m/s [0.10 in/min]						
EP-.1-1	0.48	2.54	1134	1512	1.14	2.03
EP-.1-2	0.54	2.85	890	1210	0.93	1.72
EP-.1-3	0.51	2.43	1001	1326	0.92	1.61
EP-.1-4	0.53	2.86	956	1228	1.05	1.73
EP-.1-5	0.52	2.75	979	1370	1.02	2.00
A-2-11	0.49	2.87	1112	1312	1.27	1.79
A-2-21	0.50	3.15	956	1257	1.08	1.85
A-2-16	0.50	3.02	1023	1257	1.16	1.74
A-2-3	0.49	3.85	945	1101	1.23	1.66
Mode II Precrack						
A-2-6	0.51	3.64	1212	1323	1.77	2.14
A-2-7	0.49	3.07	1268	1401	1.79	2.25
A-2-10	0.51	2.88	1290	1446	1.79	2.25
A-2-19	0.54	2.97	1245	1368	1.91	2.30

Mode II Rate Dependence: APC-2

Instron Cross Head Rate: 423×10^{-6} m/s [1.00 in/min]

Sample	$\frac{a}{L}$	C $[10^{-6}$ m/N]	PnL [N]	Pc [N]	G_{IISC}^{BT} [kj/m^2]	G_{IIC}^{BT} [kj/m^2]
EP-1-1	0.53	2.92	1023	1379	1.24	2.25
EP-1-2	0.53	2.55	912	1379	0.85	1.94
EP-1-3	0.52	3.06	890	1157	0.96	1.62
EP-1-4	0.53	2.99	845	1214	0.86	1.77
EP-1-5	0.51	2.58	1001	1334	0.99	1.75

Instron Cross Head Rate: 4233×10^{-6} m/s [10.0 in/min]

EP-10-1	0.51	2.59	1210	1210	1.43	1.43
EP-10-2	0.52	3.11	1103	1103	1.46	1.46
EP-10-3	0.52	2.82	1192	1192	1.57	1.57
EP-10-4	0.53	3.42	939	939	1.21	1.21
EP-10-5	0.53	3.16	1023	1023	1.32	1.32

End of Document